

IDEA

**Innovations Deserving
Exploratory Analysis Programs**

NCHRP IDEA Program

Material Characteristics of Cu-Based Superelastic Alloys for Applications in Bridge Columns to Improve Seismic Performance

Final Report for
NCHRP IDEA Project 210

Prepared by:
Bora Gencturk
University of Southern California
M. Saiid Saiidi
Infrastructure Innovation, LLC

May 2022

NATIONAL Sciences
ACADEMIES Engineering
Medicine

 **TRANSPORTATION RESEARCH BOARD**

Innovations Deserving Exploratory Analysis (IDEA) Programs Managed by the Transportation Research Board

This IDEA project was funded by the NCHRP IDEA Program.

The TRB currently manages the following three IDEA programs:

- The NCHRP IDEA Program, which focuses on advances in the design, construction, and maintenance of highway systems, is funded by American Association of State Highway and Transportation Officials (AASHTO) as part of the National Cooperative Highway Research Program (NCHRP).
- The Safety IDEA Program currently focuses on innovative approaches for improving railroad safety or performance. The program is currently funded by the Federal Railroad Administration (FRA). The program was previously jointly funded by the Federal Motor Carrier Safety Administration (FMCSA) and the FRA.
- The Transit IDEA Program, which supports development and testing of innovative concepts and methods for advancing transit practice, is funded by the Federal Transit Administration (FTA) as part of the Transit Cooperative Research Program (TCRP).

Management of the three IDEA programs is coordinated to promote the development and testing of innovative concepts, methods, and technologies.

For information on the IDEA programs, check the IDEA website (www.trb.org/idea). For questions, contact the IDEA programs office by telephone at (202) 334-3310.

IDEA Programs
Transportation Research Board
500 Fifth Street, NW
Washington, DC 20001

The project that is the subject of this contractor-authored report was a part of the Innovations Deserving Exploratory Analysis (IDEA) Programs, which are managed by the Transportation Research Board (TRB) with the approval of the National Academies of Sciences, Engineering, and Medicine. The members of the oversight committee that monitored the project and reviewed the report were chosen for their special competencies and with regard for appropriate balance. The views expressed in this report are those of the contractor who conducted the investigation documented in this report and do not necessarily reflect those of the Transportation Research Board; the National Academies of Sciences, Engineering, and Medicine; or the sponsors of the IDEA Programs.

The Transportation Research Board; the National Academies of Sciences, Engineering, and Medicine; and the organizations that sponsor the IDEA Programs do not endorse products or manufacturers. Trade or manufacturers' names appear herein solely because they are considered essential to the object of the investigation.

**Material Characteristics of Cu-Based Superelastic
Alloys for Applications in Bridge Columns to Improve
Seismic Performance**

IDEA Program Final Report

IDEA Project NCHRP-210

Prepared for

The IDEA Program

Transportation Research Board

The National Academies of Sciences, Engineering, and Medicine

Bora Gencturk

University of Southern California

and

M. Saiid Saiidi

Infrastructure Innovation, LLC

May 4, 2022

ACKNOWLEDGMENTS

Over the duration of the project, several researchers have contributed to the work presented in this report: Mr. Huanpeng Hong, Dr. Amit Jain, Dr. Hadi Aryan, Dr. Farshid Hosseini, and Ms. Susan Alexis Brown, among others. The authors acknowledge the contribution of these researchers. The authors are grateful to Dr. Farhad Ansari, Project Advisor, for his continued support and feedback throughout the project. The NiTi and Cu-Al-Mn materials tested in this study were provided by the Furukawa Techno Material Co., LTD. The authors are grateful to Mr. Sumio Kise from FTM for not only providing the test specimens but also continuous feedback on the research results. Similarly, Dr. Yoshikazu Araki from Nagoya University, Japan, and Dr. Toshihiro Omori from Tohoku University have reviewed and provided input on the research findings. The authors acknowledge the support of Christian Dahl from the Headed Reinforcement Corp. for providing the coupling system used to test the steel rebar. The stainless and epoxy coated steels were donated by the Contractors Material Co. in Cincinnati, OH while the high chromium steel was donated by the MMFX Steel Corp. of America in Irvine, CA.

NCHRP IDEA PROGRAM

COMMITTEE CHAIR

CATHERINE MCGHEE
Virginia DOT

MEMBERS

FARHAD ANSARI
University of Illinois at Chicago

NICHOLAS BURMAS
California DOT

PAUL CARLSON
Road Infrastructure, Inc.

ERIC HARM
Consultant

PATRICIA LEAVENWORTH
Massachusetts DOT

A. EMILY PARKANY
Virginia Agency of Transportation

KEVIN PETE
Texas DOT

JOSEPH WARTMAN
University of Washington

AASHTO LIAISON

GLENN PAGE
AASHTO

FHWA LIAISON

MARY HUIE
Federal Highway Administration

USDOT/SBIR LIAISON

RACHEL SACK
USDOT Volpe Center

TRB LIAISON

RICHARD CUNARD
Transportation Research Board

IDEA PROGRAMS STAFF

CHRISTOPHER HEDGES
Director, Cooperative Research Programs

LORI SUNDSTROM
Deputy Director, Cooperative Research Programs

INAM JAWED
Senior Program Officer

DEMISHA WILLIAMS
Senior Program Assistant

EXPERT REVIEW PANEL

FARHAD ANSARI, *University of Illinois at Chicago*

TROY MARTIN, *HDR*

BIJAN KHALEGHI, *Washington State DOT*

YOSHIKAZU ARAKI, *Nagoya University*

TABLE OF CONTENTS

ACKNOWLEDGMENTS	I
TABLE OF CONTENTS	II
LIST OF FIGURES	IV
LIST OF TABLES	VII
LIST OF SYMBOLS AND ABBREVIATIONS	VIII
Symbols	VIII
Abbreviations.....	X
Executive Summary	1
1. IDEA Product.....	3
2. Concept and Innovation	4
2.1. Background	4
2.2. Research objectives and methodology	4
3. Investigation.....	5
3.1. Low-cycle Fatigue Behavior	5
3.1.1. Introduction	5
3.1.2. Materials and methods	5
3.1.3. Results	8
3.1.4. Summary	14
3.2. Corrosion Resistance of Cu-Al-Mn Alloys and Steel Reinforcing Bars	15
3.2.1. Introduction.....	15
3.2.2. Materials and methods	15
3.2.3. Results of long-term corrosion tests.....	19
3.2.4. Results of potentiodynamic polarization tests	22
3.2.5. Summary	25
3.3. Machinability of Cu-Al-Mn Alloys.....	25
3.3.1. Introduction.....	25
3.3.2. Materials and methods	25
3.3.3. Results for NiTi SEA	28
3.3.4. Results of CAM SEA and mild steel.....	30
3.3.5. Summary	33

3.4.	Coupling Performance of CAM Alloys.....	33
3.4.1.	Introduction.....	33
3.4.2.	Specimen preparation and test methods.....	34
3.4.3.	Results of threaded CAM SEA specimens.....	38
3.4.4.	Results of headed CAM SEA specimens.....	39
3.4.5.	Summary.....	42
3.5.	Cost Estimation of CAM SEAs in Typical Bridge Columns.....	42
3.5.1.	Introduction.....	42
3.5.2.	Design of bridge columns.....	43
3.5.3.	Analysis of bridge columns.....	44
3.5.4.	Cost estimation of typical columns.....	47
3.5.5.	Discussion.....	49
3.5.6.	Summary.....	51
4.	Plans for Implementation.....	51
5.	Conclusions.....	51
6.	Investigator’s Profile.....	52
7.	References.....	53
8.	Appendix Research Results.....	55
8.1.	WHAT WAS THE NEED?.....	55
8.2.	WHAT WAS OUR GOAL?.....	55
8.3.	WHAT DID WE DO?.....	55
8.4.	WHAT WAS THE OUTCOME?.....	55
8.5.	WHAT IS THE BENEFIT?.....	55

LIST OF FIGURES

Figure 1-1 Concept of using SEAs as plastic hinge reinforcement in columns to improve seismic performance.	3
Figure 3-1 Dimensions of (a) SCB, NTB, and (b) PCP specimens.	6
Figure 3-2 Setup for low cycle fatigue test. (a) Setup for SCB and NTB at room temperature, (b) zoom-in view of customized grip fixture for SCB and NTB, (c) zoom-in view of grip fixture for PCP, (d) inside view of environmental chamber and setup for PCP, and (d) outside view of environmental chamber connected with liquid nitrogen tank.	6
Figure 3-3 Schematic diagram of the grip fixture used for SCB, NTB: (a) picture of setup, (b) front view, (c) section A-A, and (d) section B-B.	7
Figure 3-4 Schematic diagram of the grip fixture used for PCP: (a) picture of setup, (b) front view, and (c) section A-A.	7
Figure 3-5 Definition of critical mechanical properties considered in low-cycle fatigue test.	8
Figure 3-6 Stress-strain curves of SCB-25C-1 at room temperature, 25°C.	9
Figure 3-7 Variation in mechanical properties of SCB-25C-1 at room temperature, 25°C.	10
Figure 3-8 Stress-strain curves of SCB-m40C-1 at -40°C.	11
Figure 3-9 Stress-strain curves of SCB at 50°C, (a) SCB-5-C-1 and (b) SCB-50C-2.	11
Figure 3-10 Stress-strain curves of PCP-25C-1 at room temperature, 25°C.	12
Figure 3-11 Grain distribution and fracture locations of (a) PCP-25C-1, (b) PCP-25C-3, (c) PCP-25C-4 and (d) PCP-25C-5. The blue bracket shows the location of the extensometer. The red arrow shows the fracture location.	12
Figure 3-12 Stress-strain curves of NTB-25C-1 at room temperature, 25°C.	13
Figure 3-13 Stress-strain curves at typical cycles of NTB-m40.	13
Figure 3-14 Stress-strain curves at typical cycles of NTB-m10-1 at -10°C.	14
Figure 3-15 Stress-strain curves of NTB-50C-1 at 50°C.	14
Figure 3-16 Preparation of test specimens for long-term corrosion testing: (a) dimensions of SCB and PCP, (b) machined SCB, (c) surface grain boundaries of as received polycrystal CAM SEA, and (d) preparation of PCP.	16
Figure 3-17 Arrangement of test specimens in the corrosion chamber for accelerated corrosion.	17
Figure 3-18 Timeline of long-term corrosion and mechanical tests.	18
Figure 3-19 Surface conditions of four types of steel rebar after 296 days of corrosion and cleaning (numbers inside parenthesis indicate the mass loss): (a) MS, (b) XS, (c) ES, and (d) SS.	19
Figure 3-20 Surface conditions of CAM SEA specimens prior to cleaning: (a) SCB after 20 days of exposure, (b) PCP after 20 days of exposure, (c) SCB after 75 days of exposure, and (d) PCP after 75 days of exposure.	20
Figure 3-21 Corrosion surface of two CAM SEA specimens at different ages after cleaning (numbers inside parenthesis indicate the mass loss): (a) SCB-2 and (b) PCP-2.	20
Figure 3-22 Two CAM specimens that broke naturally at 1051 days, (a) SCB-1 and (b) PCP-3.	21
Figure 3-23 Mass loss in long-term corrosion tests: (a) MS, (b) XS, (c) ES, (d) SS, (e) PCP, and (f) SCB.	22
Figure 3-24 Ranked normalized mass loss of PCP, SCB, MS, XS, ES and SS after 296 days of exposure.	22

Figure 3-25 Potentiodynamic polarization curves of MS, XS, ES, SS, CAM and NiTi, where E_{corr} denotes the open corrosion potential, and i_{corr} denotes the corrosion current density.	23
Figure 3-26 Open corrosion potential of MS, XS, ES, SS, CAM and NiTi.....	23
Figure 3-27 Corrosion current density of MS, XS, ES, SS, CAM and NiTi.	24
Figure 3-28 Corrosion rate of MS, XS, ES, SS, CAM and NiTi.	24
Figure 3-29 Samples used for machinability tests: (a) mild steel, (b) CAM and (c) NiTi.....	26
Figure 3-30 Setup for machinability tests.....	26
Figure 3-31 Protocol used in machinability tests.....	27
Figure 3-32 Picture of chips obtained from NiTi machineability experiments: (a) $V_c = 60.96$ m/min, (b) $V_c = 30.48$ m/min, (c) $V_c = 15.24$ m/min and (d) $V_c = 10.67$ m/min.	28
Figure 3-33 Condition of I-NT-1 after machining NT-1 at $V_c = 60.96$ m/min, (a) front view, (b) top view, (c) left view and (d) right view.	29
Figure 3-34 Chips produced during machining CAM SEA, (a) CAM-1, (b) CAM-10, (c) CAM-20 and (d) CAM-30.....	30
Figure 3-35 Chips produced during machining mild steel, (a) MS-1, (b) MS-10, (d) MS-20, and (d) MS-30.....	30
Figure 3-36 Condition of I-CM-30 at $V_c = 60.96$ m/min after machining 30 continuous workpieces. .	31
Figure 3-37 Condition of I-MS-30 at $V_c = 60.96$ m/min, after machining 30 continuous workpieces..	31
Figure 3-38 Change in diameter of 30 mild steel specimens after machining.....	32
Figure 3-39 Change in diameter of 30 Cu-Al-Mn specimens after machining.....	32
Figure 3-40 Mean value of diameter difference of Cu-Al-Mn and mild steel.	33
Figure 3-41 Dimensions of headed end CAM SEA bars for coupling tests: (a) 20 mm diameter headed bar, (b) 30 mm diameter headed bar, and (c) 20 mm diameter threaded bar.	35
Figure 3-42 Pictures from heading process: (a) heating specimens by blowtorch, (b) heading specimens using a mechanical extruder.....	35
Figure 3-43 Setup for single coupling tests on threaded CAM SEA bar.	36
Figure 3-44 Loading protocols used for training CAM SEA bars in coupling tests.....	36
Figure 3-45 Mechanical coupler used to connect headed specimens.	37
Figure 3-46 Setup for single coupling tests on headed CAM SEA bars.	37
Figure 3-47 Constant amplitude cyclic tensile loading protocol for coupling tests.....	38
Figure 3-48 Test setup for double coupling tests on headed CAM SEA bars.....	38
Figure 3-49 Training results of HC20-1: stress strain curves of (a) middle CAM bar, and (b) image of the specimen after fracture.	39
Figure 3-50 Second training results of HC20-2: (a) CAM SEA bar, (b) top steel rebar, and (c) image of the specimen after fracture.....	40
Figure 3-51 Results of HC30-1: (a) first training, (b) second stage loading, and (c) specimen after fracture.	41
Figure 3-52 Double coupling test results of HC20-3 and HC20-4. Up Ex and Dw Ex denote the results respectively collected from the upper extensometer installed on HC20-3 and lower extensometer installed on HC20-4. Pot denotes the results collected by the linear potentiometer.	41
Figure 3-53 After fracture image of double coupling test specimens HC20-3 and HC20-4.....	42
Figure 3-54 Sectional configuration of designed columns: (a) CAM SEA RC, (b) NiTi SEA RC, and (c) steel RC.....	43

Figure 3-55 Axial force-bending moment interaction diagram of designed columns: (a) CAM SEA RC, (b) NiTi SEA RC, and (c) steel RC.....	44
Figure 3-56 Constitutive models used in sectional analysis: (a) CAM SEA, (b) NiTi SEA, (c) confined concrete, (d) unconfined concrete, and (e) steel rebar.....	45
Figure 3-57 Moment-curvature diagrams of three types of columns: (a) CAM SEA RC, (b) NiTi SEA RC, and (c) steel RC.....	46
Figure 3-58 Arrangement of longitudinal reinforcement for three types of columns, (a) CAM SEA RC, (b) NiTi SEA RC, and (c) steel RC.....	47
Figure 3-59 Cost comparison of steel RC, CAM SEA RC, and NiTi SEA RC.	50

LIST OF TABLES

Table 3-1 Summary of low-cycle fatigue test results.....	8
Table 3-2 Chemical composition of steel rebar.....	17
Table 3-3 Geometric properties of inserts.....	27
Table 3-4 Parameters of machinability tests.....	27
Table 3-5 Results of cost estimation.....	49

LIST OF SYMBOLS AND ABBREVIATIONS

SYMBOLS

A_f	Austenitic transformation finish temperature
A_g	Gross area of the cross-section
A_l	Area of longitudinal reinforcement
c	Concrete cover
$C_{cutting}$	Cost of cutting
C_{insert}	Cost of inserts
C_{setup}	Cost of setup
$C_{turning}$	Cost of turning
D	Column diameter
D	Displacement at the top end of the column
D/R	Axial demand to axial capacity ratio
d_c	Depth of cut
d_R	Damping ratio
d_{steel}	Diameter of steel rebar
d_{tr}	Diameter of transvers reinforcement
$E_{,norm}$	Normalized elastic modulus of steel rebar
E_{CAM}	Cost of each reinforcement in CAM RC
$E_{CAM-heading}$	Cost of each CAM bar when using heading
$E_{CAM-machine}$	Cost of each CAM bar when using machining
E_{corr}	Corrosion potential
$E_{coupler}$	Cost of mechanical coupler
$E_{load, norm}$	Normalized elastic modulus of loading
E_{load}	Elastic modulus of loading
E_{load2}	Elastic modulus after yielding
$E_{load3, norm}$	Normalized elastic modulus of lower yield plateau
$E_{machining}$	Cost of machining
$E_{material}$	Cost of SEA material
e_{max}	Maximum strain
E_{NiTi}	Cost of each reinforcement in NiTi RC
$e_r, norm$	Normalized rupture strain
$e_{resi, norm}$	Normalized residual strain

$E_{remainsteel}$	Cost of the remaining steel rebar
e_{resi}	Residual strain
E_{steel}	Cost of each reinforcement in steel RC
$E_{unload, norm}$	Normalized elastic modulus of unloading
$E_{load2, norm}$	Normalized elastic modulus of upper yield plateau
f_{cc}	Compressive strength of confined concrete
$f_{m, norm}$	Normalized maximum stress
$f_{y, norm}$	Normalized yield stress
f_{yCAM}	Yield strength of longitudinal CAM SEA reinforcement
f_{yl}	Yield strength of longitudinal reinforcement
f_{yNiTi}	Yield strength of longitudinal NiTi SEA reinforcement
f_{ytr}	Yield strength of transverse reinforcement
f_z	Chip load
i_{corr}	Corrosion current density
φ_u	Idealized ultimate curvature
φ_y	Idealized yield curvature
L	Column height
L_{CAM}	Length of CAM SEA in plastic region
L_{NiTi}	Length of NiTi SEA in plastic region
L_p	Plastic hinge length
N_{CAM}	Number of CAM reinforcements
n_{CAM}	Number of CAM pieces in each reinforcement
N_{NiTi}	Number of NiTi reinforcements
n_{NiTi}	Number of NiTi pieces in each reinforcement
N_{steel}	Number of steel reinforcement
P_{CAM}	Price of CAM SEA
P_{NiTi}	Price of NiTi SEA
P_{steel}	Price of steel rebar
r_{CAM}	Density of CAM SEA
r_{NiTi}	Density of NiTi SEA
r_{steel}	Density of steel rebar
$S_{Af, norm}$	Normalized austenitic transformation finish stress
$S_{hy, norm}$	Normalized stress hysteresis
S_{max}	Maximum stress

$S_{Ms, norm}$	Normalized martensitic transformation start stress
S_y	Yield stress
$T_{CAM-heading}$	Total cost of all CAM reinforcement when using heading
$T_{CAM-machine}$	Total cost of all CAM reinforcement when using machining
$T_{NiTi-heading}$	Total cost of all NiTi reinforcement when using heading
$T_{NiTi-machine}$	Total cost of all NiTi reinforcement when using machining
T_{steel}	Total cost of all steel rebar reinforcement
V_c	Cutting speed
W_{steel}	Weight of each steel rebar
z_l	Upper limit strength modifier

ABBREVIATIONS

AGG	Abnormal Grain Growth
CAM	Cu-Al-Mn
DAQ	Data Acquisition Systems
DSC	Differential scanning calorimetry
ES	Epoxy coated steel
MS	Mild steel
NiTi	Nickel-titanium
NTB	Polycrystal NiTi bars
OCP	Open circuit corrosion potential
PCP	Polycrystal CAM plates
RC	Reinforced concrete
SCB	Single crystal CAM bars
SE	Superelastic effect
SMA	Shape memory alloys
SME	Shape memory effect
SS	Stainless steel
XS	High chromium steel

EXECUTIVE SUMMARY

The superior mechanical properties of shape memory alloys (SMAs) have made them one of the most desirable smart materials applied in bridges. Due to the internal reversible martensitic transformation, SMAs can recover large (up to 10-12%) inelastic strains upon stress removal (referred to as the superelastic effect, SE) or with external heat stimuli (referred to as the shape memory effect, SME). The SE are particularly advantageous for dissipating seismic energy and protecting bridges in earthquake prone regions by substantially reducing permanent drift of bridges subjected to near-fault earthquakes. In this report, only the superelastic effect (SE) of SMA is involved, therefore, the notation of shape memory alloys (SMA) with superelastic effect (SE) is referred to SEAs for brevity.

Previous research on SEAs mainly focused on the nickel-titanium (NiTi) based alloy which showed stable behavior at or near room temperature. NiTi SEAs have been shown to have the necessary characteristics (strength, ductility, and energy dissipation capacity, among others) to be used as plastic hinge reinforcement in bridge columns. The first successful implementation of the NiTi SEAs in the SR99 Alaskan Viaduct Bridge in Seattle has been completed in 2017. However, certain properties of the NiTi based SEAs such as the difficulty in machining, potential loss of superelasticity at low temperature, and the high cost still drive the search for alternate materials.

As an alternative material to NiTi, this research investigates the use of Cu-Al-Mn (CAM) SEAs, which are known to be cheaper and easier to machine. Considering both the manufacturing and machining, the total cost of CAM SEAs is expected to be one-half to one-quarter of that of NiTi based ones. More importantly, the CAM SEAs show comparable or even better superelasticity, ductility, low-cycle fatigue and corrosion resistance, and wider temperature application range than NiTi ones. At the same time, it is known that CAM SEAs have a lower strength and lower energy dissipation capacity compared to NiTi SEAs, which need to be considered in design. Additionally, there are currently manufacturing challenges in producing bars longer than 300 mm and larger than 30 mm in diameter.

This report describes the research conducted under NCHRP IDEA PROJECT 210, "Material Characteristics of Cu-Based Superelastic Alloys for Applications in Bridge Columns to Improve Seismic Performance". The material properties of CAM SEAs are characterized by a series of experiments, including: low-cycle fatigue tests at various temperatures, long-term corrosion and electrochemical tests, machinability and coupling tests, as well as cost estimation of CAM SEAs in typical bridge columns. All the experiments and analysis on CAM SEAs are benchmarked with other conventional materials, such as commonly used engineering steel bars and NiTi SEAs. Both intuitive understanding and quantitative characterization are formed to fill the knowledge gap in their use in bridge columns. The key findings of this report are described as follows.

In the low-cycle fatigue tests, it was found that the single crystal CAM SEA shows excellent superelasticity and fatigue resistance at all tests temperatures: -40°C, room temperature, 25°C, and 50°C. The fatigue life of single crystal CAM SEAs can be up to 50,000 cycles under 5% strain cyclic loading, and almost no deterioration was observed in the superelastic properties of single crystal CAM SEAs in the initial 100 cycles. The superelasticity of polycrystal CAM SEAs show comparable fatigue resistance to the single crystal CAM, but the fatigue life was affected by the grain distribution and orientation. In contrast, the NiTi SEAs tested in this study show poor superelasticity and fatigue resistance compared to CAM SEAs. The NiTi SEAs lose the strain recovery completely at -40°C. At room temperature and 50°C, the energy dissipation capacity of NiTi SEAs deteriorates rapidly within less than 100 cycles.

However, some of these shortcomings of NiTi SEAs could be addressed by changing the NiTi alloy composition by adding a third alloying element such as Nb or Co.

In the long-term corrosion and electrochemical tests, it was found that the corrosion on CAM SEAs is local: it starts with local speckles and then grows into some deep pits. The mass loss and corrosion rate of CAM SEAs is around 1/3 of mild steel. After around three years of natural corrosion, the CAM SEAs still showed excellent superelasticity: its strain recovery and energy dissipation capacity showed negligible degradation.

It was found that the CAM SEAs are more machinable than NiTi SEAs. When machining NiTi at high cutting speed using standard machining tools, the tip of the insert broke completely after machining only one specimen. While at the same cutting speed, the wear on the insert tip was around 200 μm after machining 30 specimens of CAM SEAs, this degree of wear was comparable to machining conventional mild steel. Besides, all CAM specimens machined at high cutting speed showed a smooth and shiny surface condition. The change in the diameter of CAM SEAs after machining 30 specimens was only 10 μm more than that of mild steel.

In the coupling performance test, it was found that the heading process has almost no influence on the strain recovery of CAM SEAs. In five CAM SEAs tests, two 20 mm diameter headed specimens showed a ductile behavior under both cyclic and monotonic loading. The ultimate stress and strain of two headed CAM SEA specimens coupled in series reached 450 MPa and 10%, respectively. The heading process generally increased the elastic modulus of CAM SEAs and a post-heat treatment at 130°C with a duration of 45 min helped soften the material.

In the cost estimation study, it was found that columns reinforced with CAM SEAs show economic advantage over the NiTi SEA reinforced column particularly if the machining method is used to connect the SEA bars with the steel rebar. The additional cost of CAM SEA reinforced column is only about 1/4 of the cost increase of NiTi SEA reinforced column, indicating the cost effectiveness of CAM SEA resulting from its excellent machinability. Incorporating CAM SEA in the column plastic hinges of earthquake-prone bridges increased the overall initial cost of the bridge by only a few percent, a cost that is more than offset by not needing to conduct major bridge repair or replacement after strong earthquakes. The only major impediment for real life implementation of CAM SEA composition is the mechanical splicing, which is recommended for future research.

1. IDEA PRODUCT

The concept of using superelastic alloys (SEA), a type of shape memory of alloy (SMA) to improve seismic performance of bridge columns is illustrated in Figure 1-1. This project investigated the feasibility of using a new composition of shape memory alloy (SMA), specifically, Cu-Al-Mn (CAM), in bridge columns as plastic hinge reinforcement to improve seismic performance. Reinforcement in concrete structures subject to earthquakes have certain requirements. These include sufficient low-cycle fatigue life, corrosion resistance, and the ability to splice with conventional reinforcement. The latter requirement implies sufficient machineability for certain mechanical splices. Additionally, cost is always a primary consideration in implementation of new technologies. This project specifically investigated these characteristics of CAM SEAs.

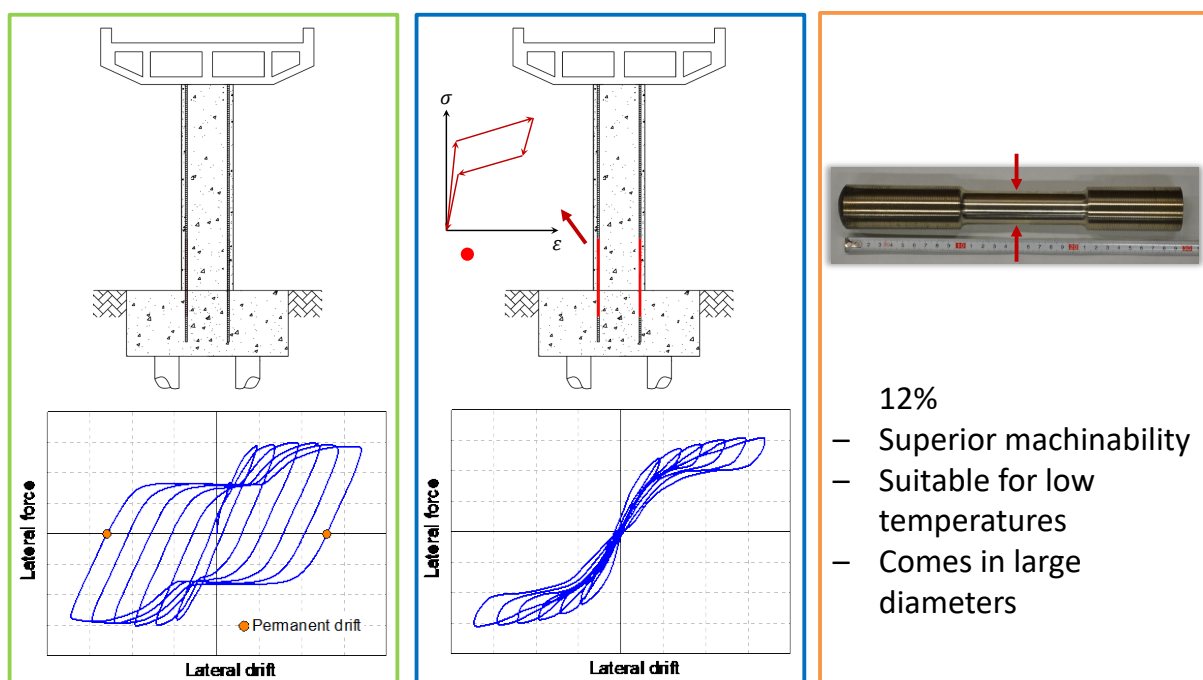


Figure 1-1 Concept of using SEAs as plastic hinge reinforcement in columns to improve seismic performance.

Prior research indicates drastic improvements to a column's seismic performance when the plastic hinge reinforcement is replaced with SEAs. The improvement is specifically in terms of repair needed after the earthquake. Up to certain strain levels, SEAs do not exhibit damage under repeated loading cycles while still dissipating energy. No damage implies no or little permanent deformations after an earthquake. This allows for continued use of bridges with or little repair after an earthquake, reducing downtime, cost and facilitating post-earthquake recovery efforts. If CAM SEAs are shown to be a feasible alternative plastic hinge reinforcement, there is a great potential to improve the seismic performance of bridges constructed in the future. This is the direct benefit of this project to DOTs, AASHTO, FHWA, Transit and Rail Transportation agencies, as well as other transportation stakeholders.

As described earlier, SEAs have already been implemented in a real project; namely, in the SR99 Alaskan Viaduct Bridge in Seattle, which was completed in 2017. However, using a different SEA composition: NiTi. It was shown that NiTi SEAs can successfully be applied in bridge columns through

research and this Alaskan Viaduct Bridge project. The motivation for this project is to determine the feasibility of the CAM alternative which offers two main advantages over the NiTi composition: cost and machineability. Additionally, as opposed to NiTi SEA, CAM SEA have a much wider temperature range and less dependency on the strain rate. These characteristics are important, deserving further research, and they could influence the adoption of this technology by the stakeholders.

2. CONCEPT AND INNOVATION

2.1. BACKGROUND

Shape memory alloys have been studied in recent years for application in bridges in moderate and high seismic areas. There are two typical properties of SMA, one is called the shape memory effect (SME) and the other one is called the superelastic effect (SE). In this report, only the SE of SMAs is studied, therefore, SMAs with SE are referred to as SEAs. Due to the internal reversible martensitic transformation, SEAs can recover large (up to 10-12%) inelastic strains upon stress removal, which is particularly advantageous for dissipating seismic energy and protecting bridges in earthquake prone regions while resulting in near zero permanent deformation and damage. To date, SEAs have been widely studied as reinforcement in bridge columns, energy dissipation devices, bracing systems and isolators.

Existing research on SEAs mainly focused on the nickel-titanium (NiTi) alloy composition, which shows stable superelasticity, corrosion resistance and biocompatibility. Nevertheless, the NiTi based SEAs are prohibitively expensive when used in large quantities in civil engineering applications, difficult to process, and their relatively high austenitic transformation finish temperature, A_f , leads to a total loss of superelasticity at low temperatures ($<0^\circ\text{C}$). The relative high cost, poor machinability and narrow operating temperature prevent the wide application of NiTi based SEAs in civil engineering.

Cu-Al-Mn SEAs, which show excellent low-cycle fatigue stability, a wider temperature range, and higher cost efficiency have shown great potential for application in bridges and recently attracted research attention. The CAM SEAs have comparable superelastic strain recovery to conventional NiTi SEAs with a price that is only a fraction of NiTi ones. It is shown in this report that when machining and coupling with conventional steel rebar are taken into consideration, the added cost of replacing plastic hinge reinforcement of columns with CAM SEAs is only about 1/4 of that of NiTi SEAs. In addition to the excellent superelasticity and low-cost, the CAM SEA also show less dependency on loading rate and temperature. All these advantages warrant an in-depth investigation of CAM SEA focused on applications in bridge columns in seismic regions.

2.2. RESEARCH OBJECTIVES AND METHODOLOGY

Research to date showed promising mechanical performance of CAM SEAs as an alternative to NiTi SEAs, particularly in bridges [1–7]. However, a comprehensive study on various characteristic that are essential in application in bridges: corrosion resistance, low-cycle fatigue performance, machinability and coupling, and a cost study has been lacking. This project aims to fill this important research gap by investigating the basic material properties of CAM SEAs mentioned above. A series of experiments and analyses were conducted to characterize the properties of CAM SEAs, namely, the low-cycle fatigue performance at various temperatures, the long-term and electrochemical corrosion characteristics, the machinability and coupling with steel rebar, as well as the cost of using CAM SEAs in typical bridges columns. For comparison purposes, all the experiments and analysis on CAM SEAs

are benchmarked against conventional materials, such as commonly used engineering steel reinforcing bars and NiTi SEAs. To achieve the objectives of the project, the following tasks were conducted:

- A state-of-the art review of publicly available literature on the fatigue performance, corrosion resistance, machining and coupling of both CAM SEAs and NiTi SEAs.
- Conducted low-cycle fatigue tests at -40°C, 25°C and 50°C, up to 50,000 cycles. Three types of materials were tested and compared: single crystal CAM SEA bars, polycrystal CAM SEA plates, and polycrystal NiTi bars.
- Conducted long-term (three years of exposure) corrosion tests. Single crystal CAM SEA bars, polycrystal CAM SEA plates, and four types of commonly used engineering steels: mild steel, high chromium steel, epoxy coated steel, and stainless steel were tested under the same conditions and compared. The mass loss, corrosion surfaces, stress-strain curves of these materials were characterized and analyzed. Electrochemical tests on the abovementioned materials and NiTi were also conducted.
- Conducted machinability tests on NiTi SEA, CAM SEA, and mild steel. By machining these materials under similar conditions, the wear on the machine insert and the diameter variation of the machined products were measured and compared.
- Conducted mechanical tests on headed large diameter CAM SEAs. The feasibility of connecting large diameter CAM SEAs with steel rebar by headed coupling was investigated through cyclic and monotonic loading tests. Large diameter threaded coupling specimens were also prepared and tested to make a comparison with headed CAM SEA bars.
- Conducted an analytical study on the cost estimation of using CAM SEA and NiTi SEA in bridge columns. The total cost of constructing three types of bridge columns (steel reinforced concrete (RC) column, CAM RC column and NiTi RC column) was evaluated and compared under the same scenario.

3. INVESTIGATION

3.1. LOW-CYCLE FATIGUE BEHAVIOR

3.1.1. Introduction

In this section, the low-cycle fatigue behavior of CAM SEAs in comparison to NiTi SEAs is determined at -40°C, 25°C and 50°C. Strain cycles up to 50,000 have been applied at a tensile strain of 5%. These parameters cover most civil engineering conditions. Variations in superelastic mechanical properties were observed and analyzed, including the stress-strain curves, elastic modulus, transformation stresses, damping ratio and recovery strain.

3.1.2. Materials and methods

3.1.2.a. Materials

The materials considered in the low-cycle fatigue tests are single crystal and polycrystal CAM and polycrystal NiTi SEAs. The composition of CAM and NiTi SEAs are Cu-8.38Al-11.32Mn (wt. %), and 55.93NiTi (wt. %), respectively. Both materials were obtained from Furukawa Techno Material Co., Ltd. The transformation temperatures of CAM and NiTi SEAs used in this study were measured by differential scanning calorimetry (DSC). The A_f of CAM and NiTi SEAs were obtained as -67.3 °C and -15.5 °C, respectively.

Two forms of CAM SEA specimens and one form of NiTi SEA specimen were studied; namely, single crystal CAM SEA bars (SCB), polycrystal CAM SEA plates (PCP, obtained from polycrystal

CAM SEA bars), and polycrystal NiTi SEA bars (NTB). The as received CAM and NiTi SEA bars all had a 20 mm diameter. The SCB and NTB were machined from as received rods to 140 mm long and 16 mm diameter coupons with a diameter of 12.7 mm in the gauge length. To obtain PCP, the as received polycrystal CAM rods were sliced along the length into four pieces, the middle two larger pieces were used for testing. The dimensions of SCB, NTB and PCP used in this study are shown in Figure 3-1.

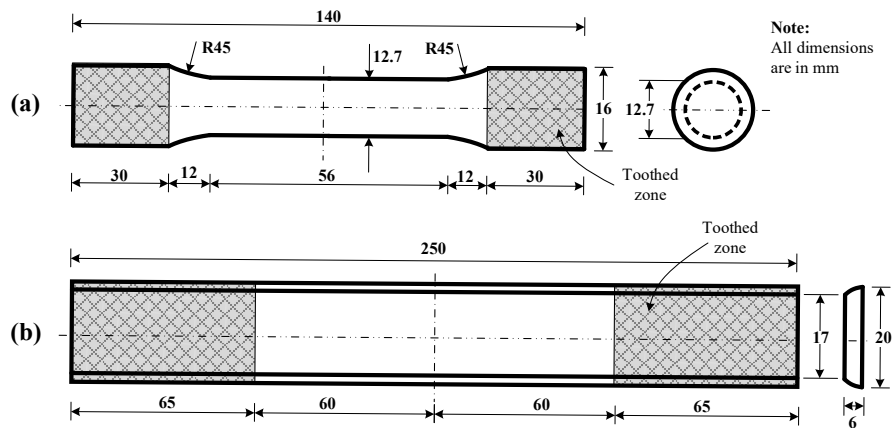


Figure 3-1 Dimensions of (a) SCB, NTB, and (b) PCP specimens.

3.1.2.b. Methods

Figure 3-2 shows the setup of the low-cycle fatigue tests. An MTS 370.5 dynamic servo-hydraulic frame with 500 kN force capacity, 15.24 cm displacement and 30 gpm flow capacity was used to apply the cyclic loading. For high, 50°C, and low, -40°C, temperature tests, an MTS 651.06E-04 environmental chamber was equipped to the MTS frame. The environmental chamber has internal dimensions of 35.56×43.18×81.28 cm (W×D×H) and a temperature range from -128.9°C to 215.6°C. An Epsilon Model No. 3542-0200-050-ST with 50.8 mm gauge length extensometer, ASTM E83 B-1 [8], was used to measure the strain in the specimens. A Mars Labs BMS16HR-53 Data Acquisition System (DAQ) was used to collect the data.

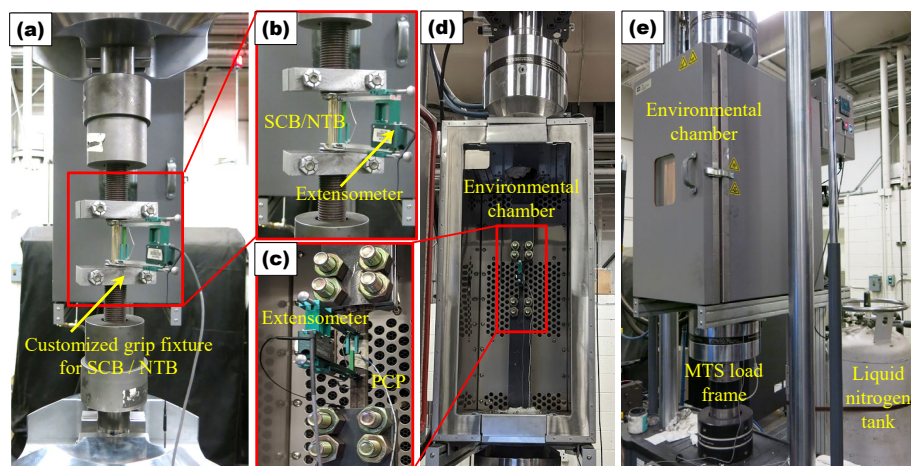


Figure 3-2 Setup for low cycle fatigue test. (a) Setup for SCB and NTB at room temperature, (b) zoom-in view of customized grip fixture for SCB and NTB, (c) zoom-in view of grip fixture for PCP, (d) inside view of environmental chamber and setup for PCP, and (e) outside view of environmental chamber connected with liquid nitrogen tank.

To reduce the stress concentrations at the grips, custom fixtures were designed and fabricated. For SCB and NTB, the round bars were mounted in a conical grip, which had a smooth contact with the

specimens, as shown in Figure 3-3. This mechanical contact-based grip effectively reduced the stress concentrations and eliminated premature failures. The PCP was gripped by two steel plates at the ends, where two steel plates were tightened by four high strength steel bolts, as shown in Figure 3-4.

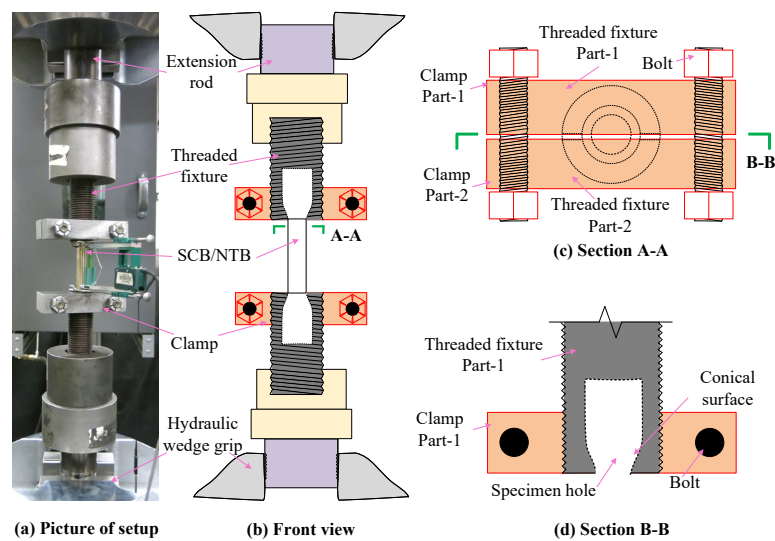


Figure 3-3 Schematic diagram of the grip fixture used for SCB, NTB: (a) picture of setup, (b) front view, (c) section A-A, and (d) section B-B.

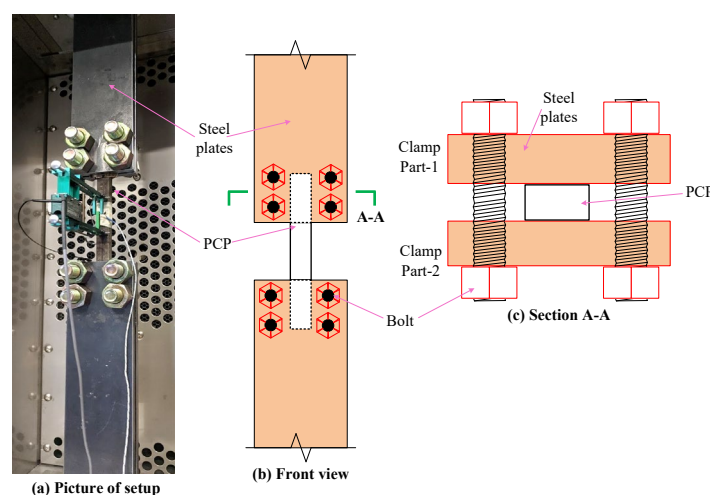


Figure 3-4 Schematic diagram of the grip fixture used for PCP: (a) picture of setup, (b) front view, and (c) section A-A.

Prior to low-cycle fatigue tests, all specimens were trained at room temperature to stabilize the martensitic transformation. The training consisted of five tensile cycles with increasing amplitude of 1% to 5% at 1% increments. During the low cycle fatigue tests, specimens were stretched to 5% target strain at a speed of 0.4% strain/sec, then unloaded to near-zero force within around 10 seconds. The target force in unloading was set close to zero but not exactly zero to avoid any slack or compressive loading in the specimens. This process was cyclically repeated until fracture occurred. The loading was strain controlled while the unloading was force controlled. For low temperature tests, the test condition was produced using a liquid nitrogen tank. With the existing setup, it was not feasible to replace the liquid nitrogen tank without disrupting the test environment. Therefore, the cold temperature tests had to be completed before the tank ran out (within approximately 24 hours).

To quantify the effect of fatigue and temperature on the superelasticity of CAM and NiTi SEAs, seven critical properties were extracted from the stress-strain curves; namely, the elastic modulus, E_{load} , the elastic modulus after yielding, E_{load2} , the maximum stress, σ_{max} , the yield stress, σ_y , the damping ratio, δ_R , the maximum strain, ϵ_{max} , and the residual strain, ϵ_{resi} . The definition of these properties is shown in Figure 3-5. The damping ratio is calculated using the equation shown in Figure 3-5 by dividing the area enclosed by the hysteresis loop by the product of the maximum strain and maximum stress applied in that cycle.

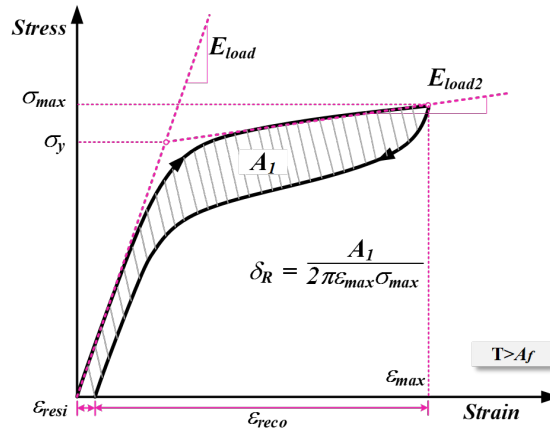


Figure 3-5 Definition of critical mechanical properties considered in low-cycle fatigue test.

3.1.3. Results

Since a large number of specimens were tested in the study, for each testing scenario, only two typical specimens are presented here. A summary of the low-cycle fatigue test results is provided in Table 3-1. The purpose of these experiments is to investigate how the mechanical properties of CAM SEAs deteriorate, and benchmark this against NiTi SEAs. Hence, obtaining the fatigue life is not the main research goal and the testing was stopped when either of the following conditions was achieved: (1) the specimen fractures, (2) the residual strain becomes stable, or (3) the liquid nitrogen tank runs out. Nevertheless, it was possible to obtain the fatigue life of certain specimens when the specimen was fractured before the test was terminated.

Table 3-1 Summary of low-cycle fatigue test results.

Material	Temperature	Label	Total loading cycles	Reason for test termination
SCB	Room temperature (25°C)	SCB-25C-1	50,000	Condition 2
		SCB-25C-2	10,000	Condition 2
		SCB-25C-3	4,285	Condition 1
		SCB-25C-4	5,326	Condition 1
		SCB-25C-5	7,000	Condition 2
		SCB-25C-6	10,000	Condition 2
	Cold temperature (-40°C)	SCB-m40C-1	5,500	Condition 1
		SCB-m40C-2	2,600	Condition 3
		SCB-m40C-3	7,200	Condition 1
	Hot temperature (50°C)	SCB-50C-2	9,100	Condition 2
SCB-50C-3		2,100	Condition 2	
SCB-50C-1		2,100	Condition 2	
PCP	Room temperature (25°C)	PCP-25C-1	15,006	Condition 1

	PCP-25C-2	1,280	Condition 1
	PCP-25C-3	357	Condition 1
	PCP-25C-4	110	Condition 1
	PCP-25C-5	104	Condition 1
	NTB-25C-1	89	Condition 1
Room temperature (25°C)	NTB-25C-2	30	Condition 1
	NTB-25C-3	53	Condition 1
	NTB-m40C	6	Condition 1
Cold temperature (-10°C)	NTB-m10C-1	1,981	Condition 3
	NTB-m10C-2	450	Condition 1
	NTB-m10C-3	1,132	Condition 1
Hot temperature (50°C)	NTB-50C-1	88	Condition 1
	NTB-50C-2	15	Condition 1
	NTB-50C-3	29	Condition 1

It should be noted that the SCB-25C-3 and SCB-25C-4 were tested by directly gripping the specimens with the hydraulic wedge grips, prior to fabrication of the custom grip fixture. Therefore, stress concentration at the grip points led to a premature fracture of these two specimens. The rest of SCB and NTB were tested with the customized fixture.

3.1.3.a. Single crystal CAM SEA bar (SCB)

SCB at room temperature, 25°C

Figure 3-6 shows the room temperature, 25°C, stress-strain curves of SCB-25C-1. It is seen that both single crystal CAM SEA bars show excellent superelasticity until about 200 cycles. In the first 100 cycles, the stress strain curves remain ideal flag-shaped and almost no degradation of strain recovery is observed. From 100 to 1,000 cycles, the stress-strain curves shrink, and the residual strain increases. Moreover, the damping ratio shows an obvious increase from 100 to 1,000 cycles. The reason for this increase is the reduction of the transformation stress and increase in the area of the stress-strain curves. A similar behavior was observed for the other specimens.

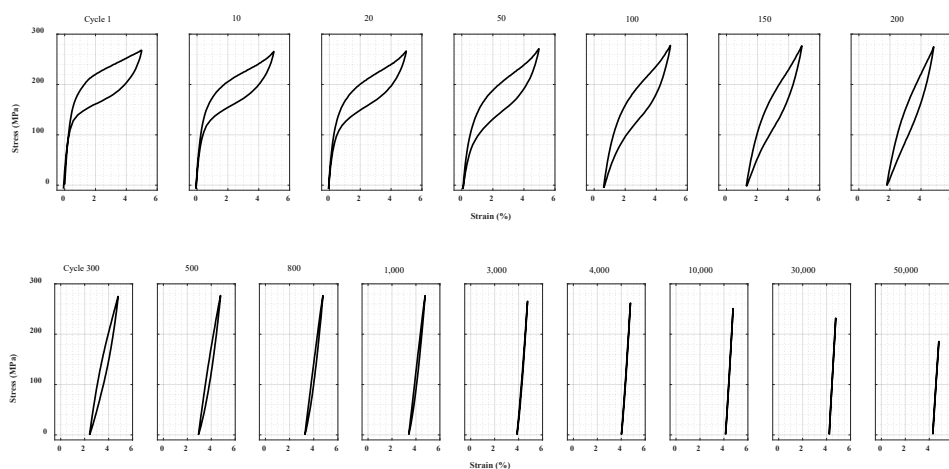


Figure 3-6 Stress-strain curves of SCB-25C-1 at room temperature, 25°C.

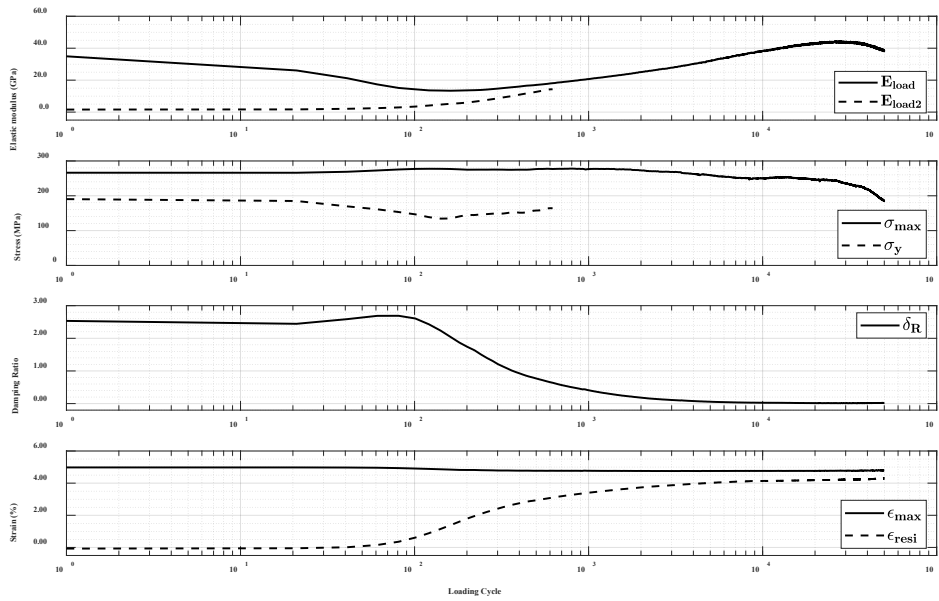


Figure 3-7 Variation in mechanical properties of SCB-25C-1 at room temperature, 25°C.

Figure 3-7 show the variation in the extracted parameters with increasing loading cycles. In Figure 3-6, it is seen that the yield stress first decreases and then almost disappears at around 1,000 cycles; however, because the yield stress is obtained as the intersection point of E_{load} and E_{load2} , this disappearance did not show in the extracted results in Figure 3-7. Furthermore, when the ratio of E_{load2} to E_{load} is over 0.85, the E_{load2} and σ_y are largely influenced from numerical error; therefore, the results for these parameters were truncated when the ratio of E_{load2} to E_{load} reached 0.85. As seen in Figure 3-7, the residual strain and damping ratio of SCB-25C-1 starts to saturate at around 1,000 cycles, and after that, they remain stable until 50,000 cycles. It is an important finding that even after 50,000 cycles of 5% strain loading, the CAM SEA bar can still sustain loading with no visible crack or fracture. This demonstrates excellent low-cycle fatigue resistance of CAM SEAs.

SCB at -40°C

Figure 3-8 shows the stress-strain curves of SCB-m40C-1 at -40°C. It is seen that at -40°C, the SCB shows an ideal flag-shaped stress strain curve and excellent damping capacity until 200 cycles. Furthermore, the specimen SCB-m40C-1 showed no rupture after 5,500 cycles of fatigue loading. The test was stopped because the liquid nitrogen tank ran out and the environmental chamber could not sustain a stable low temperature condition. The envelope curve from training at room temperature is presented with a grey dashed line at Cycle 1. As seen in Figure 3-8, the transformation stress at -40°C is lower than that at room temperature. However, area inside the stress strain cycles at -40°C is larger than that at room temperature (refer to Figure 3-6), which indicates higher energy dissipation capacity of CAM SEAs at low temperature. The variation in the mechanical properties at -40°C is similar to that at room temperature. But what is worth noting is that the energy dissipation capacity and strain recovery at -40°C are superior to those at room temperature, demonstrating the promise of CAM SEAs for use at cold temperatures.

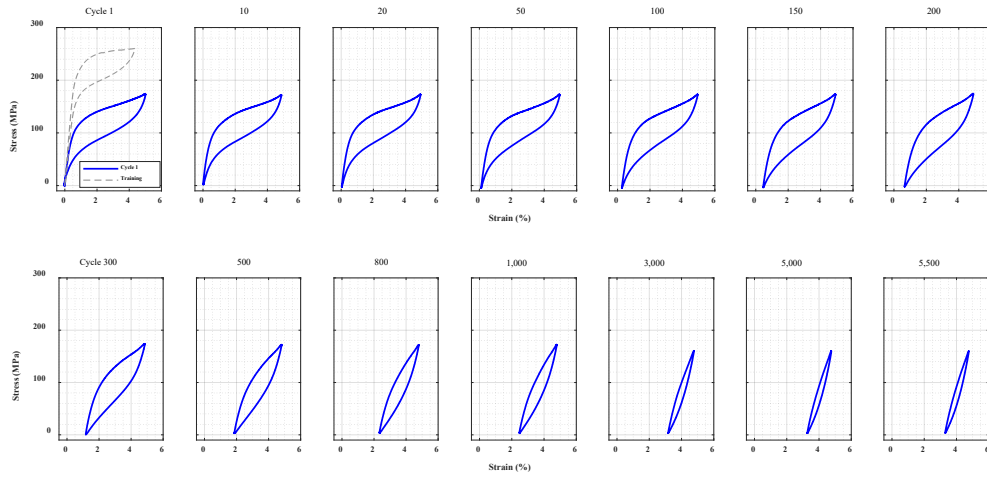


Figure 3-8 Stress-strain curves of SCB-m40C-1 at -40°C .

SCB at 50°C

The stress-strain curves of SCB-50C-1 at 50°C are shown in Figure 3-9. The envelope curve from training at room temperature is presented with a grey dashed line. SCB-50C-1 showed no fracture after 9,100 cycles of loading. Compared with the stress strain curves at room temperature (shown in Figure 3-6), and -40°C (shown in Figure 3-8), the transformation stress of CAM SEAs at 50°C is higher and the stress-strain curves become narrower. The general variation in the mechanical properties at 50°C is similar to those at room temperature and -40°C . An important observation is that the damping ratio at 50°C shows an increase after 100 cycles. The reason is that in the first several cycles, the stress-strain curves are very narrow, and the damping only is a result of the flag-shaped zone while as the residual strain increases and the transformation stress decreases, the stress-strain curve becomes larger and leads to an increase in the damping ratio. After around 1,000 cycles, the response of the CAM SEAs becomes almost linear.

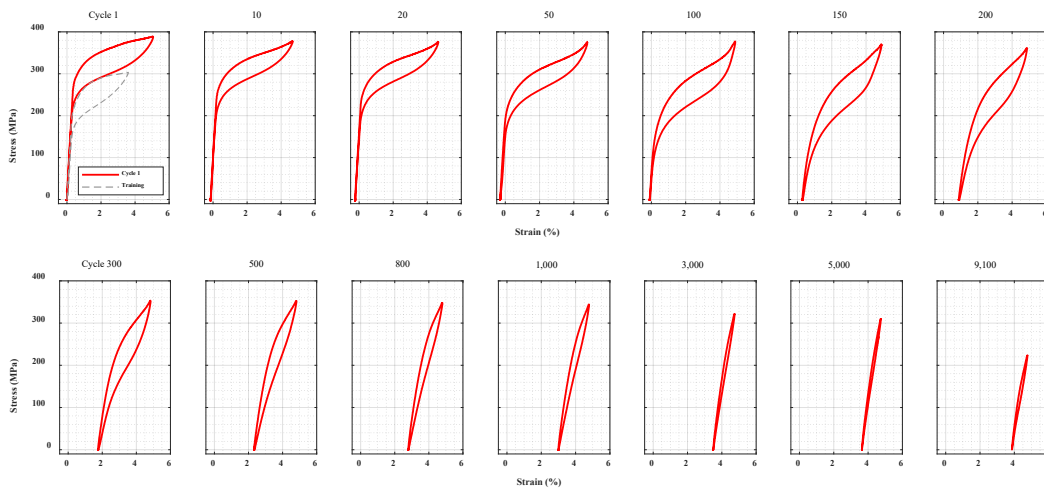


Figure 3-9 Stress-strain curves of SCB at 50°C , (a) SCB-5-C-1 and (b) SCB-50C-2.

3.1.3.b. Polycrystal CAM SEA plate (PCP)

Figure 3-10 shows the stress-strain curves of PCP-25C-1 at selected cycles at 25°C . The specimen ruptured after 15,000 cycles of fatigue loading. It is seen that the fatigue resistance of PCP-25C-1 is similar to that of single crystal CAM SEA bar. In the initial 100 cycles, the superelasticity shows almost no degradation, and flag-shaped stress-strain curves and energy dissipation are observed. From 100 to

1,000 cycles, the stress-strain curves become narrower, and the residual strain accumulates rapidly. After 1,000 cycles, the specimen behaves almost linearly until fracture.

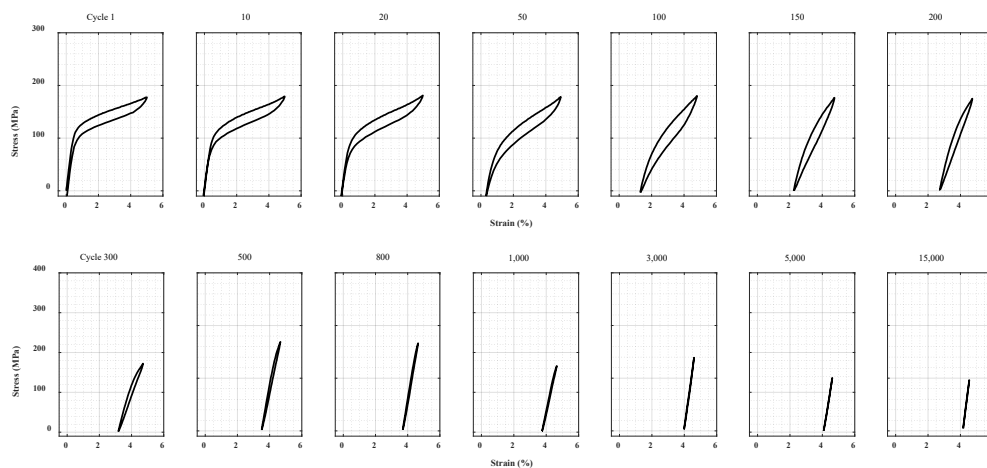


Figure 3-10 Stress-strain curves of PCP-25C-1 at room temperature, 25°C.

Even though a long fatigue life (i.e., 15,000 cycles) exhibited by PCP-25C-1, the fatigue life of the rest of PCP showed a large scatter. The rest of four PCP, respectively, fractured at 1,280, 357, 110 and 104 cycles. Figure 3-11 shows the grain distribution and fracture location of the PCP specimens. The black solid lines indicate the grain boundaries on the specimen surface, obtained by visual observation; the blue dash line and the bracket indicate the gauge length where the extensometer was placed during the test. Compared with the SCB, the reason why the PCP show a large scatter in fatigue life is that each polycrystal plate is composed of several small and randomly distributed grains with different sizes and orientations, as shown in Figure 3-11. In fatigue loading, the boundaries of neighboring grains, particularly when the neighboring grains have different orientations, may cause stress concentrations and result in crack formation and propagation [2,9,10]. The fracture location of each of the PCP is marked with a red arrow in Figure 3-11, which supports this explanation. Because of the large dependence of the fatigue behavior on the grain size, distribution and orientation, no further tests on PCP were conducted at low or high temperatures.

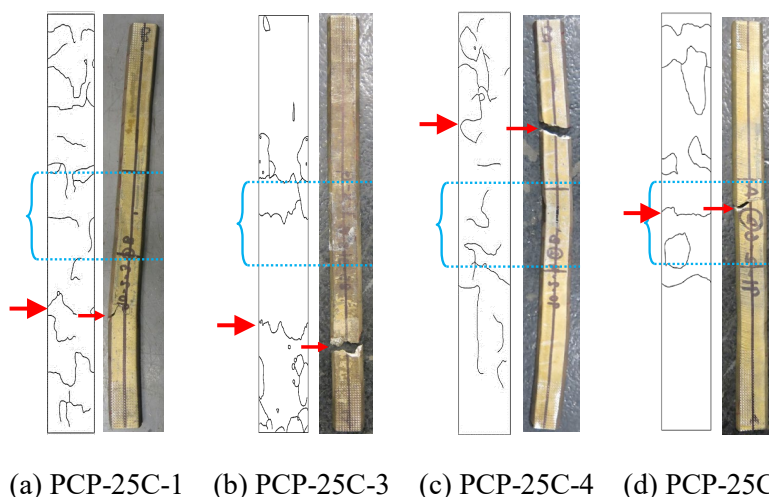


Figure 3-11 Grain distribution and fracture locations of (a) PCP-25C-1, (b) PCP-25C-3, (c) PCP-25C-4 and (d) PCP-25C-5. The blue bracket shows the location of the extensometer. The red arrow shows the fracture location.

3.1.3.c. NiTi bar (NTB)

NTB at room temperature, 25°C

Figure 3-12 shows the stress-strain curves of NTB-25C-1 at 25°C. The three tested NiTi SEA bars at 25°C all fractured rapidly with fatigue lives of 89, 31 and 54 cycles. It is seen that the stress-strain curve of NTB in the 1st cycle is not an ideal flag-shape. The transformation stress and residual strain of NTB reach 400 MPa and 1%, both of which are higher than those of CAM SEAs in the 1st cycle. More importantly, the stress-strain curve of the NTB narrows even in the first few cycles, leading to a sharp decrease in the energy dissipation. The residual strain also increases slightly in the first few cycles and then stabilizes until fracture. This ratcheting phenomenon of NiTi SEAs is consistent with the results presented by Maletta et al. [11].

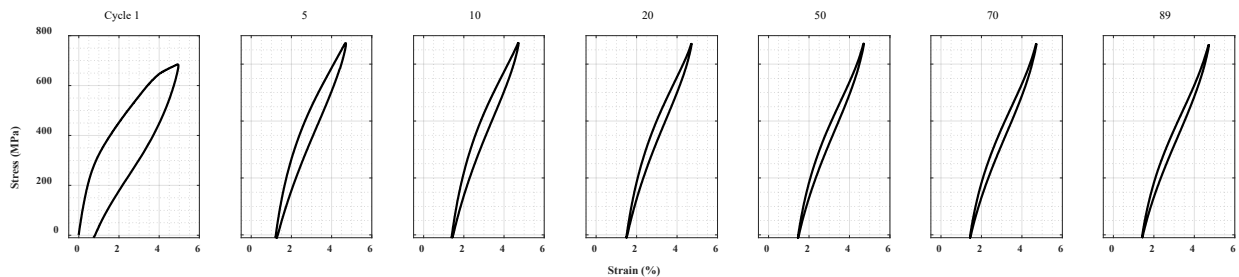


Figure 3-12 Stress-strain curves of NTB-25C-1 at room temperature, 25°C.

NTB at -40°C and -10°C

The low temperature fatigue tests on NiTi bars were conducted at -40°C and -10°C. Stress-strain curves at select cycles of NTB-m40 are shown in Figure 3-13 in addition to the envelope curve of training at room temperature in grey. From Figure 3-13, it is seen that the NiTi SEA is in pure martensitic phase at -40°C. No superelasticity is seen because no austenite-martensite phase transformation is involved. The specimen NTB-m40C fractured after 6 cycles of fatigue loading.

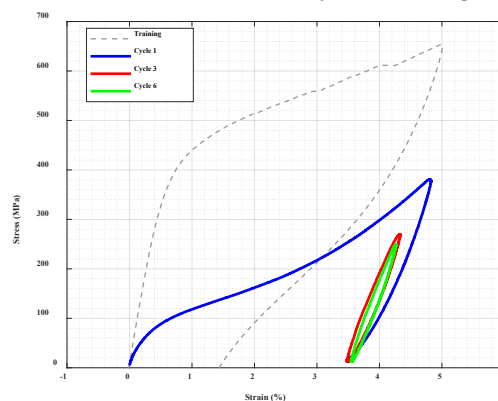


Figure 3-13 Stress-strain curves at typical cycles of NTB-m40.

Because no superelasticity was observed at -40°C, additional testing was performed at -10°C to investigate the fatigue resistance of NiTi SEAs. Figure 3-14 shows the stress-strain curves of NTB-m10C-1 at -10°C. Compared with NiTi SEAs at 25°C, the specimen at -10°C shows a higher fatigue life, this trend is consistent with Iasnii et al. [12] and Mahtabi et al. [13]. The energy dissipation and strain recovery at -10°C starts to degrade rapidly at around 10 cycles and stabilize at around 100 cycles.

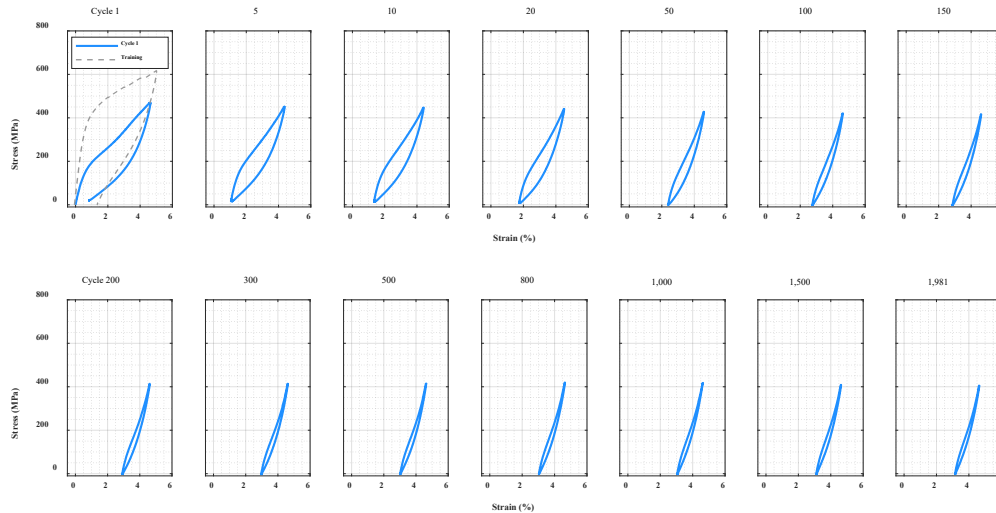


Figure 3-14 Stress-strain curves at typical cycles of NTB-m10-1 at -10°C.

NTB at 50°C

The stress-strain curves of NTB-50C-1 at 50°C are shown in Figure 3-15. The transformation stress of NTB at 50°C reaches 500 MPa, which is higher than the training results. All NiTi bars at 50°C fractured after a few cycles of loading. The first one ruptured after 87 cycles of fatigue loading while the second and the third ones fractured after 15 and 29 cycles, respectively. Furthermore, the stress-strain curves became narrow very rapidly and then kept constant until fracture. It is observed that the elastic modulus and transformation stress shows negligible degradation. The damping ratio and the residual stress degrade rapidly and then stabilize. Even in the first cycle, significant residual strain is observed, indicating the poor superelasticity of NTB at 50°C.

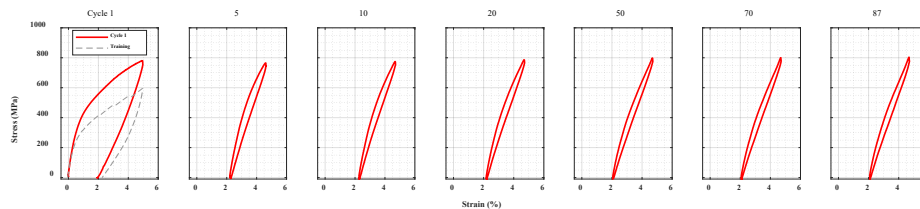


Figure 3-15 Stress-strain curves of NTB-50C-1 at 50°C.

3.1.4. Summary

The SCB showed excellent superelasticity and fatigue resistance at all tests temperatures: -40°C, room temperature, 25°C, and 50°C. Specifically, in the initial 100 cycles, no deterioration was observed in the superelastic properties. Between 100 to 1,000 cycles, the transformation stress started to decrease, the residual strain started to accumulate, and a slight decrease in the elastic modulus was observed. The stress-strain response became almost linear after around 8,000, 2,000, and 2,000 cycles at -40°C, 25°C and 50°C, respectively. The superelasticity and fatigue resistance of polycrystal CAM SEAs were found to largely depend on the grain characteristics, such as the grain size, orientation and boundaries. The five PCP specimens all showed comparable superelasticity to single crystal ones at the early stages of fatigue loading (1 to 100 cycles), but the fatigue life showed a large scatter (difference of more than two orders of magnitude). The best two PCP tested in this study showed a fatigue life of over 15,000 cycles (PCP-25C-1) and excellent superelasticity with zero residual strain accumulation up to 200

cycles (PCP-25C-2). NiTi SEAs tested in this study showed poor superelasticity and fatigue resistance compared to CAM SEAs. Specifically, at room temperature, 25°C and at 50°C, the stress-strain curves of NiTi SEAs reduced in size even in the first few cycles, leading to a significant decrease in the energy dissipation capacity. Additionally, at -40°C, the NiTi SEAs completely lost superelasticity because they were in martensitic phase and no austenite-martensite phase transformation was involved. The one NiTi SEA bar tested at -40°C fractured after 6 cycles of fatigue loading. To sum up, the large number of fatigue cycles and the temperature range considered here strongly suggests the feasibility of using single crystal CAM SEAs in earthquake-prone regions.

3.2. CORROSION RESISTANCE OF CU-AL-MN ALLOYS AND STEEL REINFORCING BARS

3.2.1. Introduction

In this study, corrosion resistance of CAM SEAs, four types of commonly used reinforcing steels, and NiTi SEAs was investigated through long-term natural corrosion tests and potentiodynamic polarization tests. Long-term natural corrosion testing of single and polycrystal CAM SEAs, and four types of commonly used reinforcing steels (mild steel, high chromium steel, epoxy coated steel, and stainless steel) was conducted up to 1015 days. For each type of steel, three different diameters of bars were evaluated: 9.53 mm (U.S. #3), 15.88 mm (U.S. #5) and 32.26 mm (U.S. #10). Critical mechanical properties of CAM SEAs and steel rebar were extracted and analyzed when specimens reached predetermined corrosion levels. Potentiodynamic polarization tests were performed on single crystal CAM SEAs, four types of commonly used reinforcing steels, and polycrystal NiTi SEAs. Tafel curves were used to determine the corrosion rates of CAM and NiTi SEAs and reinforcing steels. The experimental data and control groups in this research provides detailed evaluation of the corrosion resistance of CAM SEAs and guides their application in harsh environmental conditions.

3.2.2. Materials and methods

3.2.2.1. Materials

The materials considered in the long-term corrosion tests included two types of CAM SEAs, namely, single crystal CAM bars (SCB), polycrystal CAM plates (PCP); and four types of steel rebar, namely, mild steel (MS), epoxy coated steel (ES), and stainless steel (SS), high chromium steel (XS). The materials considered in the potentiodynamic polarization tests included single crystal CAM SEAs, polycrystal NiTi SEAs, and the same four types of steel rebar used in the long-term corrosion tests (MS, ES, SS and XS). The composition and manufacturer of CAM and NiTi SEAs used are the same as those presented earlier.

The as received CAM material (both single crystal and polycrystal) was in the form of 20 mm diameter smooth rods. The dimensions of SCB and PCP used in the long-term corrosion tests are shown in Figure 3-16(a) and (b). To obtain PCP, the surface grain boundaries of the as received polycrystal CAM SEA rods was marked based on a visual inspection before slicing, as shown in Figure 3-16(c). After that, the polycrystal CAM rods were sliced along the length into four parts as shown in Figure 3-16(d), the middle two larger parts, denoted as PCP-i and PCP-iC (i ranges from 1 to 5), were used for long-term corrosion testing. The PCP-i was mechanically tested after designed corrosion levels and its counterpart PCP-iC was mechanically tested without corrosion. Since PCP-i and PCP-iC came from the same as received rod and had almost the same grain distribution, their behavior was compared to determine the effect of corrosion on fracture behavior of polycrystal CAM SEAs.

The MS, ES, SS and XS used in the this study respectively conform to: ASTM A516 Grade 60 [14], ASTM A615 Grade 60 [15], ASTM A955 S32304 [16], and ASTM A1035 CS Grade 100 [17]. The chemical composition of these rebar is presented in Table 3-2. For each type of steel bar used in the long-term corrosion test, three diameters were considered, namely, U.S. #3 (diameter = 9.53 mm), U.S. #5 (diameter = 15.88 mm) and U.S. #10 (diameter = 32.26 mm). These sizes represent the most commonly used sizes and provides an opportunity to determine the rate of corrosion as a function of rebar diameter. Three samples of each size and material were tested to ensure repeatability of the results. As mentioned in the next section, the samples were tested at four different levels of corrosion. Therefore, in total, 4 (steel types) \times 3 (sizes) \times 4 (corrosion degrees) \times 3 (repetitions) = 144 steel rebar were tested in this study. The label of steel specimens presented in this report is composed of four parts, first, the steel type (i.e., MS, XS, ES, SS); second, the diameter number (i.e., #3, #5, #10); third, the corrosion degree, which is the exposure duration of the specimen in days (i.e., D0, D20, D75, D296); finally, the repetition of the specimens of each type (i.e., 1, 2, 3). For example, ‘MS#3D0-1’, indicates mild steel with a diameter of 9.53 mm (U.S. #3), at corrosion exposure of zero days (start of the corrosion testing) and 1st specimen of this type; similarly, ES#5D75-3 indicates: epoxy coated steel, with a diameter of 15.9 mm (U.S. #5), at corrosion exposure of 75 days, and 3rd specimen of this type.

For specimens used in the potentiodynamic polarization tests, all six materials (single crystal CAM, polycrystal NiTi, MS, ES, SS, XS) were firstly machined into 1 cm³ cubes and then embedded into an epoxy resin mount to leave one exposed surface with 1 cm² area. The exposed surface was polished before submerging into the solution. Three specimens were prepared for each material, and they were labeled in order. For example, CAM-1 indicates the first specimen of CAM material, SS-3 indicates the third specimen of SS material.

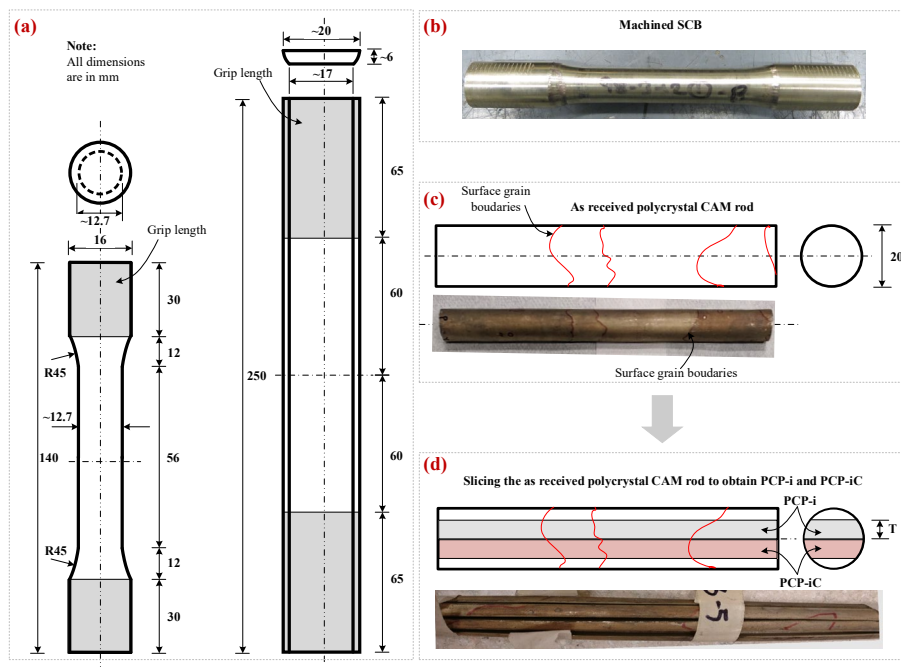


Figure 3-16 Preparation of test specimens for long-term corrosion testing: (a) dimensions of SCB and PCP, (b) machined SCB, (c) surface grain boundaries of as received polycrystal CAM SEA, and (d) preparation of PCP.

Table 3-2 Chemical composition of steel rebar.

Steel type	Size	Chemical composition, %				
		C	Mn	P	S	Si
MS	#3	0.21	0.77	0.03	0.03	0.29
	#5	0.23	1.05	0.03	0.03	0.29
	#10	0.23	1.05	0.03	0.03	0.29
ES	#3	0.44	0.33	0.15	0.28	0.23
	#5	0.43	0.81	0.23	0.23	0.11
	#10	0.35	0.79	0.21	0.23	0.11
SS	#3	22.77	3.69	0.3	1.68	0.18
	#5	22.56	4.18	0.35	1.77	0.19
	#10	22.65	4.02	0.31	1.65	0.2
XS	#3	9.54	0.68	0.46	0.17	0.09
	#5	9.86	0.57	0.43	0.19	0.1
	#10	9.51	0.53	0.44	0.14	0.08

3.2.2.a. Methods

Long-term corrosion of CAM SEAs was performed in two phases. First, the specimens were subjected to a continuous salt spray in a corrosion chamber for 296 days. Next, the salt spray was stopped, and the specimens were removed (without cleaning) to normal laboratory environment until 1051 days. The steel rebar (MS, XS, ES and SS) were subjected to salt spray in a corrosion chamber for 296 days. A fine mist of 5% by weight NaCl solution was sprayed constantly at 40°C in the chamber. The NaCl was purchased from Fisher Scientific with purity $\geq 99.0\%$. The average rate of salt spray was 1.34 mL/hour. The corrosion chamber used in this study is WEICE WTC/A160. The selected exposure conditions is based on ASTM G85 [18] with slight deviation in the temperature.

Figure 3-17 shows all the test samples in the corrosion chamber prior to testing. As shown in Figure 3-17, all specimens were placed vertically in the chamber to allow for air circulation around the specimens and prevent ponding on the surfaces. The specimens were taken out regularly for subsequent tests at predetermined corrosion times. A red corrosion resistant coating was used to prevent corrosion of the gripped ends.

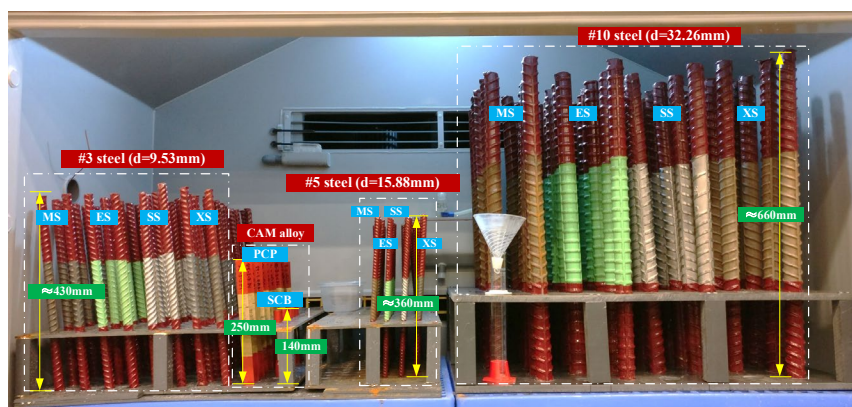


Figure 3-17 Arrangement of test specimens in the corrosion chamber for accelerated corrosion.

In this study, the percent mass loss was used as one of the indicators of degree of corrosion for different materials. The percent mass loss is obtained as the ratio of mass loss at a given age of exposure and original mass at day zero. At each predetermined corrosion days, specimens were cleaned according to the following steps. Specimens were first rinsed in deionized water; second, scrubbed with plastic bristle brush to loosen the corrosion products; they were next cleaned in an ultrasonic bath for 15 minutes; then, placed in solution that was made by 500 ml of 37% by weight HCl (purchased from Grainger) and 500 ml reagent water for 5 min; HCl was removed by rinsing the sample using DI water and then acetone; finally, dried before the mass loss measurement. Steps 1 to 3 were repeated until the mass loss value becomes constant. A Branson CPX8800H ultrasonic bath was used to clean SCB, PCP, #3 and #5 steel rebar. For #10 steel rebar, no ultrasonic bath was used in the third step of cleaning and this step was skipped because the specimens were too large to fit into the bath.

After thorough cleaning, gravimetric measurements were conducted to determine the mass loss and mass loss percentage. For SCB, PCP and #3 steel rebar, a Mettler Toledo ME303E scale with 320 g capacity and 1 mg sensitivity was used. For #5 and #10 steel rebar, a Cole-Parmer SK-10000-53 scale with 15 kg capacity and 0.5 g sensitivity was used.

The timeline of the long-term corrosion tests and mechanical tests is shown in Figure 3-18. It is noted that the PCP and SCB specimens were taken out of the corrosion chamber at predetermined days, cleaned, mechanically tested without failure, and then put back into the chamber for subsequent corrosion and mechanical testing. On the other hand, the steel rebar specimens that had reached the predetermined days were taken out, cleaned, and monotonically tested until failure. Relevant measurements were collected from those specimens before disposal. The mechanical test results are omitted in this report for brevity and they will be presented in future publications.

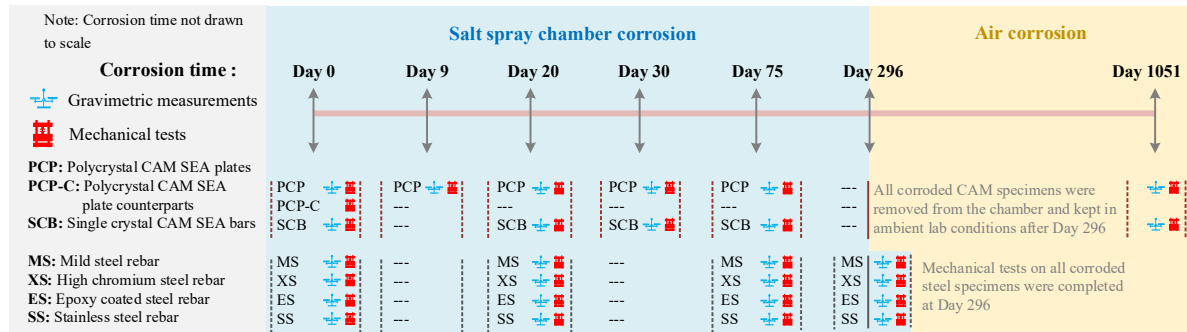


Figure 3-18 Timeline of long-term corrosion and mechanical tests.

The electrochemical measurements were conducted at 30°C in a MultiPort Gamry Corrosion Cell containing 800 ml of 3.5% by weight NaCl solution. The voltage/current was applied and the data was collected using an INTERFACE1000E Gamry Potentiostat. The temperature of the corrosion cell was controlled in a WBE10 PolyScience water bath. A classic three-electrode cell was used for potentiodynamic polarization tests, where platinum was used as the counter electrode, standard silver-silver electrode was used as the reference electrode and the specimen as the working electrode.

Prior to the electrochemical tests, specimens were submerged in 1100 ml of 1M NaCl solution, inside a 30°C water bath for 1 hour and the open circuit corrosion potential (OCP) was determined. Then a polarization of ±200 mV from OCP was applied to the specimens with a constant scan rate of 0.33 mV/s. For each material, the polarization test was performed on three different samples to ensure the reproducibility of results.

3.2.3. Results of long-term corrosion tests

3.2.3.a. Visual observation

Figure 3-19 shows the typical corrosion surface of four types of steel rebar after 296 days of exposure and cleaning. In the figure under each rebar image, the percentage in the bracket indicates the corresponding mass loss percentage. For brevity, only one typical specimen is selected from each diameter of rebar to show the surface conditions. It is seen in Figure 3-19 that after 296 days of exposure, the MS and XS corroded more severely than ES and SS, furthermore, rebar with smaller diameter showed a higher amount of corrosion than rebar with larger diameter. The corrosion on MS was found to be relatively uniform; however, the corrosion on XS was highly inhomogeneous. Apart from the significant cross-sectional area reduction along the whole specimen, some very deep pits were observed. The interconnected deep pits led to a porous-like corrosion surface on XS. The similar porous surface was also observed for XS by Nachiappan et al. [20]. The ES and SS were both in good surface condition after corrosion, almost no damage could be observed on their surface after cleaning. The epoxy coat on ES was intact and the surface condition of SS had no visible change.

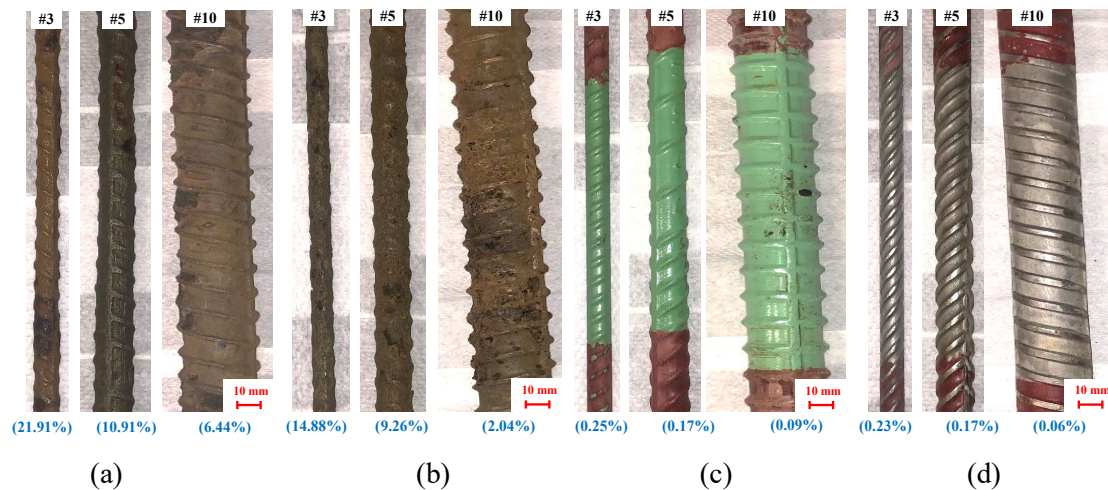


Figure 3-19 Surface conditions of four types of steel rebar after 296 days of corrosion and cleaning (numbers inside parenthesis indicate the mass loss): (a) MS, (b) XS, (c) ES, and (d) SS.

Figure 3-20 shows the surface conditions of corroded SCB and PCP before cleaning. The corrosion of both SCB and PCP started with some tiny speckles, some visible dull red speckles were observed after nine days of exposure when the mass loss was approximately 0.15%. Then, the speckled corrosion areas gradually merged into some bigger spots. As shown in Figure 3-20(a) and (b), after 20 days of exposure, at a mass loss of approximately 0.2%, some obvious local corrosion spots were observed, but the spots on PCP were smaller and more uniform than those on SCB. As corrosion progressed, the local spots turned into some deep-black and soft corrosion products. After 75 days of exposure, with at a mass loss of approximately 1%, the surface of both PCP and SCB were covered with cotton-like corrosion products, as shown in Figure 3-20(c) and (d).



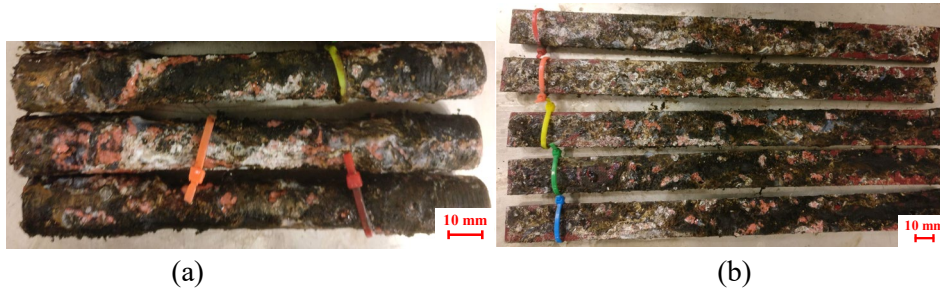


Figure 3-20 Surface conditions of CAM SEA specimens prior to cleaning: (a) SCB after 20 days of exposure, (b) PCP after 20 days of exposure, (c) SCB after 75 days of exposure, and (d) PCP after 75 days of exposure.

Figure 3-21 shows the surface conditions of SCB and PCP after cleaning. Two typical specimens, SCB-2 and PCP-2 are selected for this presentation while the rest of the CAM specimens showed similar surface patterns. The number in the bracket indicates the mass loss percentage after different exposure durations. From the clean surfaces shown in Figure 3-21, it is confirmed that the corrosion on both PCP and SCB did not occur uniformly. The corrosion initiates in some local pits and grows bigger and deeper, which is consistent with Figure 3-20. Some large corrosion spots were observed after 296 days of exposure when the mass loss of SCB-2 and PCP-2 reached 4.24% and 6.82%, respectively. The local corrosion pits on SCB were more obvious than those on PCP nonetheless not being as deep as those on XS. At the final corrosion stage after 1051 days at a mass loss of 5.80% and 12.10%, respectively, for SCB-2 and PCP-2, both SCB and PCP corroded seriously, the local corrosion pits merged together along the length, and the cross-sectional area decreased accordingly.

It is worth noting that two of the specimens broke without an application of external force before (PCP-3) or during (SCB-1) the cleaning at Day 1051 as shown in Figure 3-22. These two specimens were different in that they became very brittle with corrosion and broke without any external force while the rest of the specimens were able to withstand the subsequent cyclic mechanical tests. This problem may be attributed to the local corrosion concentrated on the surface defects or grain boundaries, which grew into intergranular corrosion cracks penetrating through the specimen.

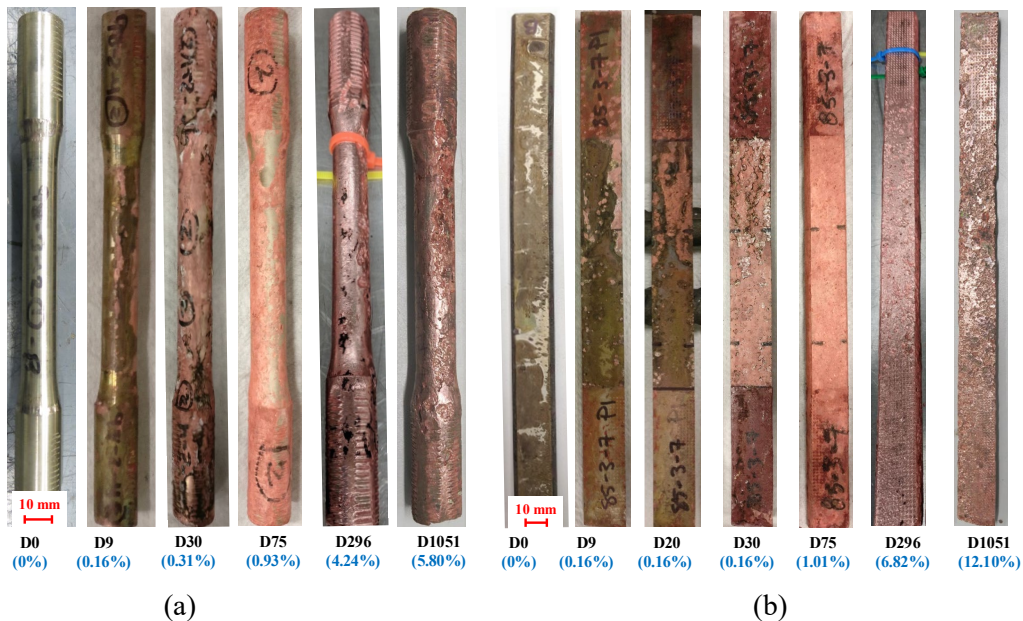


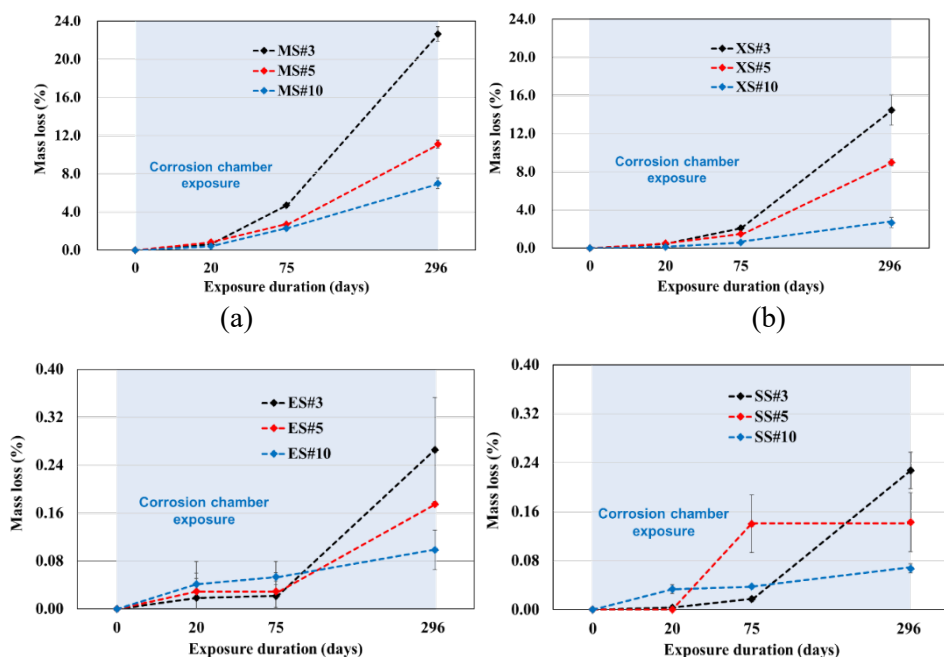
Figure 3-21 Corrosion surface of two CAM SEA specimens at different ages after cleaning (numbers inside parenthesis indicate the mass loss): (a) SCB-2 and (b) PCP-2.



Figure 3-22 Two CAM specimens that broke naturally at 1051 days, (a) SCB-1 and (b) PCP-3.

3.2.3.b. Mass loss analysis

Figure 3-23 shows the mass loss of CAM SEAs and steel rebar over the testing duration. The exposure duration is not drawn to scale. It should be noted that some specimens (PCP in early corrosion, ES and SS) had negligible mass loss. For these cases, the mass loss is taken zero. It is seen that during the salt spray exposure up to 296 days, the MS shows the highest mass loss, but its mass loss shows large dependence on the rebar diameter. The mass loss of #3 MS is around three times that of #10 MS. The mass loss of XS is smaller than MS but it shows similar diameter dependency. The mass loss of #3 XS is around 60% of #3 MS. The ES and SS showed negligible mass loss (around 1/100 of MS and XS) throughout the testing program, which agrees with the visual observation in Figure 3-20. The large scatter in the test data is due to measurement error associated with small changes in the mass of the rebar. An apparent increase in the mass loss of #3 ES after 75 days should be interpreted with caution due to large error associated with the measurements and very low mass loss in ES and SS specimens over the entire period of testing. The mass loss of PCP is close to the #3 XS and is around twice that of the SCB. During corrosion in the ambient laboratory conditions from 296 days to 1051 days, the mass loss of PCP is almost doubled (increased by 82%) while the SCB increased by 40%. The average mass loss of six types of specimens at 296 days of exposure is normalized by the mean value of #3 MS and compared in Figure 3-24. It is seen that the mass loss of PCP is about the same as that of #10 MS and it is around 1/3 of the #3 MS. The mass loss percent of SCB has been observed to be around 1/5 of #3 MS.



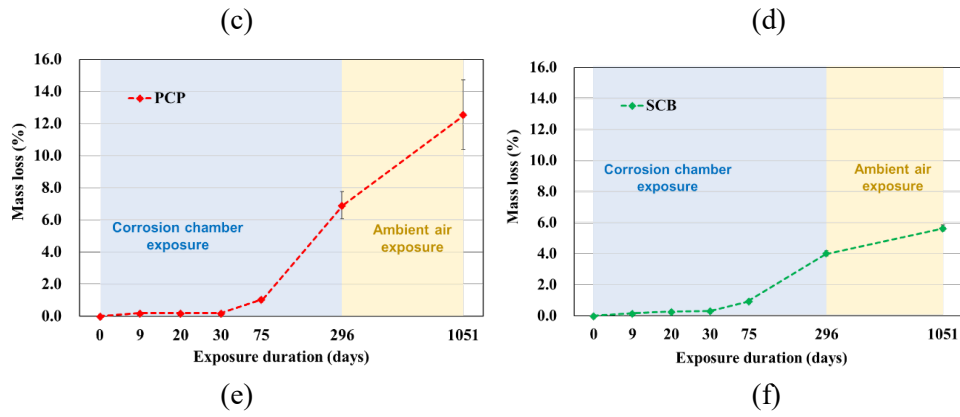


Figure 3-23 Mass loss in long-term corrosion tests: (a) MS, (b) XS, (c) ES, (d) SS, (e) PCP, and (f) SCB.

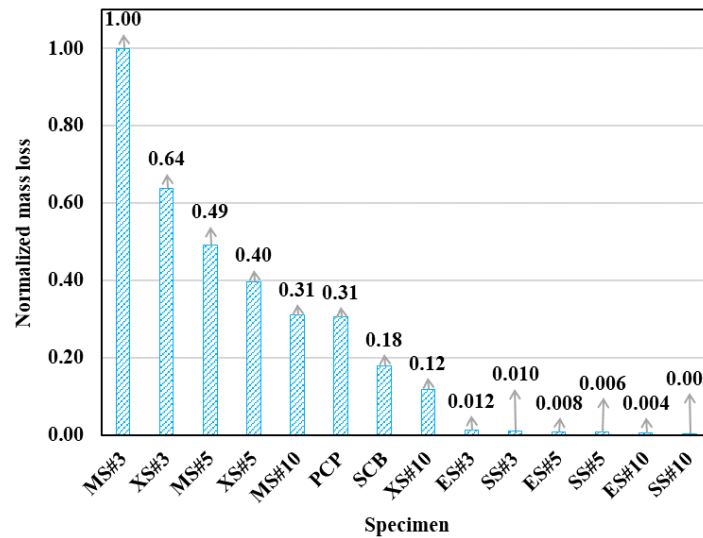


Figure 3-24 Ranked normalized mass loss of PCP, SCB, MS, XS, ES and SS after 296 days of exposure.

3.2.4. Results of potentiodynamic polarization tests

3.2.4.a. Potentiodynamic polarization curves

Figure 3-25 shows the potentiodynamic polarization curves of six materials: MS, XS, ES, SS, CAM and NiTi. From these curves, it is seen that: in terms of corrosion potential, the rank of six materials from largest to smallest is: MS, ES, NiTi, CAM, XS and SS; while in terms of corrosion current density, the rank of six materials from largest to smallest is: NiTi, SS, XS, CAM, MS and ES. The CAM shows close corrosion potential to NiTi, but its corrosion current density is much higher than that of NiTi.

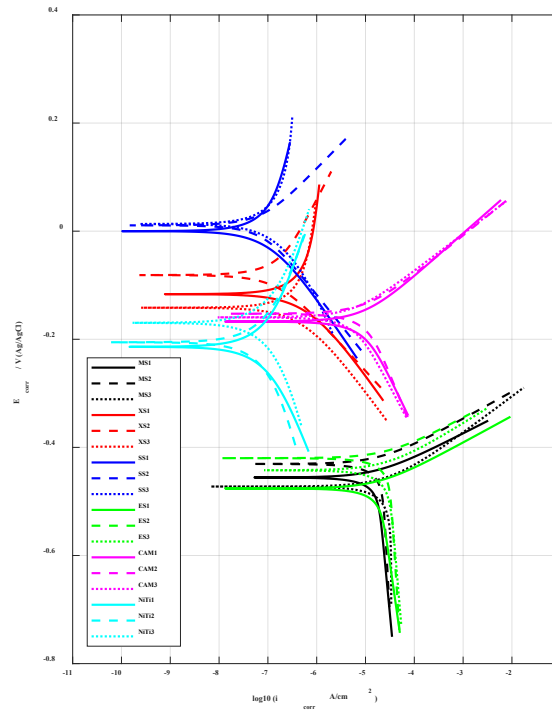


Figure 3-25 Potentiodynamic polarization curves of MS, XS, ES, SS, CAM and NiTi, where E_{corr} denotes the open corrosion potential, and i_{corr} denotes the corrosion current density.

3.2.4.b. Corrosion potential and density

Based on the potentiodynamic polarization curves, the open corrosion potential, E_{corr} , and corrosion current density, i_{corr} , of six materials were extracted, as shown in Figure 3-26 and Figure 3-27, respectively. An average was taken from the three samples. The average open corrosion potential, E_{corr} , of MS, XS, ES, SS, CAM and NiTi were obtained as -453 mV, -113 mV, -446 mV, 8 mV, -160 mV, and -196 mV, respectively. The average corrosion current density, i_{corr} , of MS, XS, ES, SS, CAM and NiTi were obtained as 16.26 $\mu\text{A}/\text{cm}^2$, 0.31 $\mu\text{A}/\text{cm}^2$, 14.37 $\mu\text{A}/\text{cm}^2$, 0.08 $\mu\text{A}/\text{cm}^2$, 4.75 $\mu\text{A}/\text{cm}^2$, and 0.07 $\mu\text{A}/\text{cm}^2$, respectively.

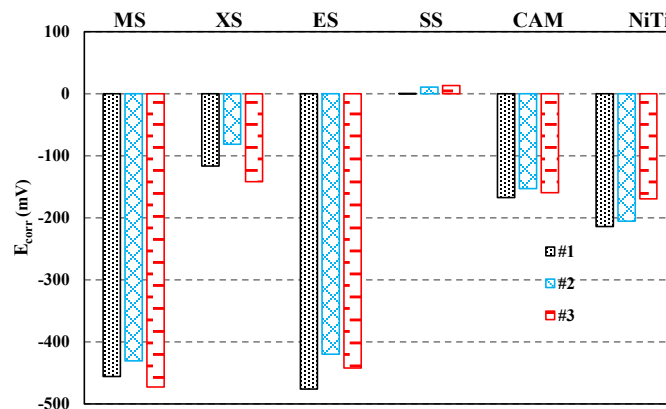
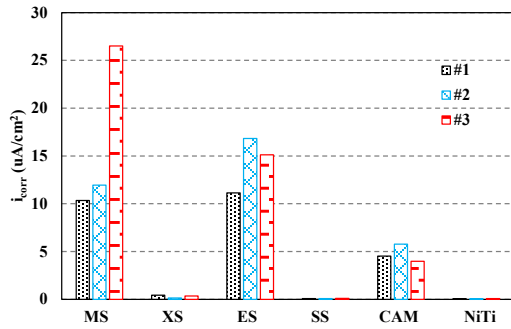
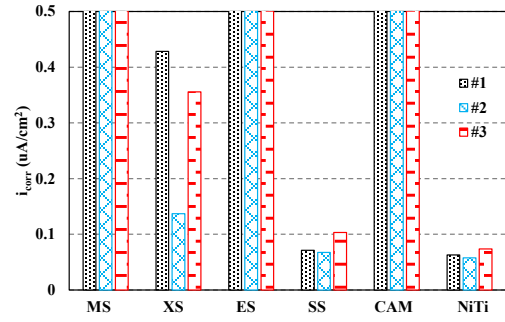


Figure 3-26 Open corrosion potential of MS, XS, ES, SS, CAM and NiTi.



(a) Corrosion current density, i_{corr}



(b) Corrosion current density, i_{corr} within the range from 0-0.5 $\mu\text{A}/\text{cm}^2$

Figure 3-27 Corrosion current density of MS, XS, ES, SS, CAM and NiTi.

3.2.4.c. Corrosion rate

Based on Faraday's law and the average corrosion current density, i_{corr} , the corrosion rate of six materials is computed and ranked in the order from largest to smallest, see Figure 3-28. The corrosion rate of CAM is 0.0565 mm/year, close to the value 0.032 mm/year measured in [21]. From Figure 3-28, it is seen that the corrosion rate of CAM is higher than SS and NiTi, but is only 1/3 of that of MS.

It is worth noting that under salt spray chamber corrosion testing, the ES showed comparable mass loss to SS (see Figure 3-23). However, in the electrochemical tests, the corrosion rate of ES (0.1687 mm/year) was close to that of MS (0.1910 mm/year). The reason is that the corrosion resistance of ES relies on the exterior epoxy coating to prevent chloride attack. While in the electrochemical tests, the epoxy coating was removed, and the inner base material was exposed to solution. Without the exterior physical barrier against chloride ions, the ES behaves like normal MS.

Besides, the XS in the salt spray chamber tests showed serious surface corrosion (deep corrosion pits and porous surface condition as shown in Figure 3-19) and mass loss (see Figure 3-23). However, in the electrochemical tests, the corrosion rate of XS (0.0035 mm/year) was close to that of SS (0.0008 mm/year) and both of them were much lower than that of MS (0.1910 mm/year). This may attribute to the sensitivity of XS to sodium chloride concentration. According to Nachiappan et al [20], at 0.1% NaCl concentration, the corrosion rate of XS is 1/12 of that of MS, but when the concentration of NaCl is increased to 3%, the corrosion rate of XS increases to 1/2 of that of MS. In this study, the NaCl concentration in the electrochemical tests was 3.5%, lower than the 5% used in salt spray tests. Moreover, the long-term fine mist salt spray creates more contact between the chloride ion and the porous surface of XS, thereby leading to more corrosion on the XS.

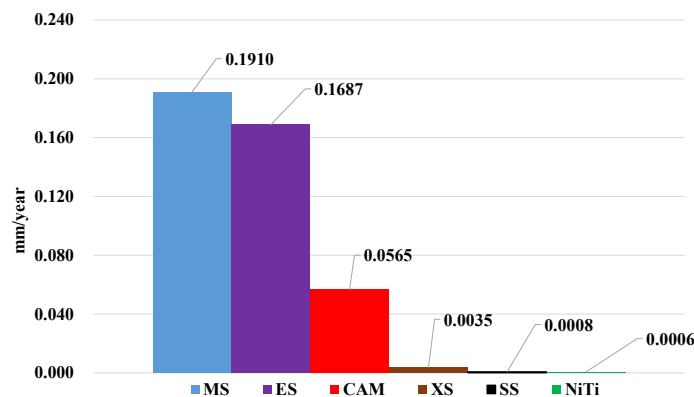


Figure 3-28 Corrosion rate of MS, XS, ES, SS, CAM and NiTi.

3.2.5. Summary

During the long-term corrosion tests, corrosion on both PCP and SCB were local, initiating with local speckles and then growing to some deep pits. The local corrosion pits merged together along the length and the cross-sectional area of the CAM SEAs decreased accordingly. In general, the mass loss of PCP was higher than that of SCB, but both were lower than those of MS and XS, and higher than those of ES and SS. Specifically, after around three years of salt spray and ambient air exposure, the mass loss of MS was the highest; the XS was around 60% of MS; the PCP and SCB was around 1/3 of MS; the ES and SS was only around 1/100 of MS. The mass loss of MS and XS showed large dependency on the diameter: the corrosion degree increased in order from #3 diameter to #5 diameter and #10 diameter. The ES and SS showed negligible mass loss and their mass loss dependency on the rebar diameter was negligible.

The mechanical properties degradation of CAM SEA varied from specimen to specimen. After three years of corrosion, the yield stress of SCB decreased about 20% at a mass loss of around 6%; the PCP showed more than 40% degradation percent because its mass loss reached 15%. Besides, because of the different grain distributions and orientations, the mechanical properties of PCP showed a large scatter among specimens. It should be noted that after three years of corrosion, both PCP and SCB still showed superelastic behavior. Specifically, the superelastic strain recovery of all CAM SEAs showed no degradation for all the tested specimens; the fracture strain of one corroded SCB was over 32%. From electrochemical test, it was seen that the corrosion potential of CAM is comparable to NiTi and less than SS and XS, but its corrosion current density is close to those of MS and ES. Based on the Faraday's law, the corrosion rate of CAM is 0.0565 mm/year, which is only around 1/3 of that of MS. It is noted that the bimetallic corrosion of different steels with CAM and NiTi SEAs is expected to be different than the single metal corrosion results reported here. Since there will be electrical connectivity between the plastic hinge reinforcement (e.g., CAM or NiTi SEAs) and the steel rebar, the relative corrosion of the two metals will depend on the standard electrode potentials. In the cases of steel-CAM or steel-NiTi coupling, the steel is likely to be the anode and CAM or NiTi is likely to be the cathode. Bimetallic corrosion of CAM SEAs with different types of steel is recommended as future research.

3.3. MACHINABILITY OF CU-AL-MN ALLOYS

3.3.1. Introduction

Machinability of NiTi is known to be more difficult than that of steel. The high hardness and specific heat of NiTi result in excessive tool wear, degraded surface conditions and a very low production rate. As a result, machining NiTi is expensive and time-consuming. In contrast, evidence indicates that CAM SEAs show much better machinability. However, quantitative data on the machineability of CAM SEAs are lacking. No systematic research has been conducted on the machinability of CAM SEAs in comparison to known materials or NiTi SEAs. In this chapter, a quantitative comparison of the machinability of CAM SEA with NiTi SEAs and normal mild steel rebar has been conducted. Specifically, tool wear and dimensions of the finished product are used as measures of machineability.

3.3.2. Materials and methods

3.3.2.a. Materials

Three types of materials were considered for the machinability tests, namely polycrystal CAM SEA, NiTi SEA and AISI 1018 mild steel (MS). The composition and manufacturer of CAM and NiTi

SEAs used in this study are the same as those presented earlier. Since only polycrystal CAM SEA and polycrystal NiTi SEA were involved in this chapter, for brevity, they are hereafter simply referred to as CAM and NiTi, respectively. For all three materials, cylindrical samples with 20 mm diameter and approximately 50 mm length were prepared as shown in Figure 3-29. The Vickers hardness of the NiTi, CAM and MS were measured as 438, 280, 237, respectively. A LECO Model No. LM-100 microindentation hardness tester was used for these measurements.

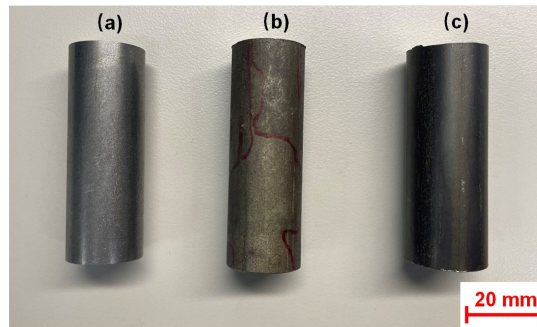


Figure 3-29 Samples used for machinability tests: (a) mild steel, (b) CAM and (c) NiTi.

3.3.2.b. Methods

Turning experiments were conducted to examine the machinability of CAM, NiTi and MS. Figure 3-30 shows the setup used in turning tests. A TRAK 1630SX lathe CNC machine with a three horsepower (2.24 kW) motor and a spindle speed range of 150-2500 rpm was used to run the turning experiments. The KOOL MIST FORMULA #77 mist spray coolant was applied during the machining. A Hertel CCMT32.50.5BH HT115CR uncoated cermet turning insert were employed for all machineability tests. The geometric properties of the inserts are given in Table 3-3.

Figure 3-31 illustrates the machining protocol used in this study. The turning tests were mainly influenced by three key parameters: cutting speed, V_c (m/min), depth of cut, d_c (mm) and chip load, f_z (mm/rev). In this study, the chip load and depth of cut were fixed for all tests. The chip load was 0.1 mm/rev. The depth of cut contained two parts: rough and finish one, as shown in Figure 3-31. The rough depth of cut was 1.016 mm, and the finish depth of cut was 0.508 mm. The same cutting speed, $V_c = 60.96$ m/min was used for CAM and NiTi. For NiTi, three cutting speeds of $V_c = 60.96$ m/min, $V_c = 30.48$ m/min, and $V_c = 10.67$ m/min were investigated. The parameters of the machinability tests are given in Table 3-4.

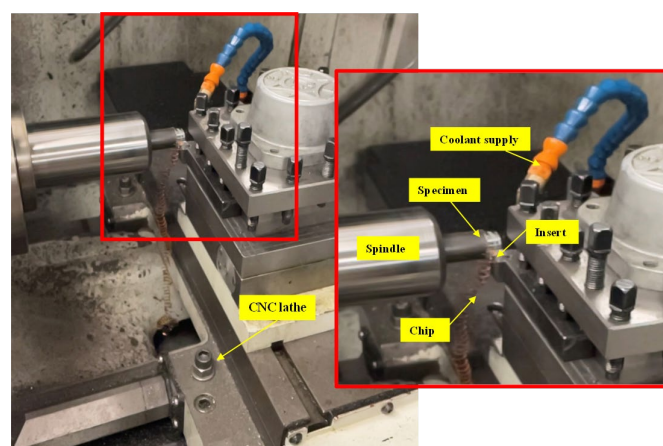


Figure 3-30 Setup for machinability tests.

Table 3-3 Geometric properties of inserts.

Rake	Positive
Rake Angle	5°
Relief Angle	7°
Included Angle	80°
Insert Hand	Neutral
Length	9 mm
Inscribed Circle	9.53 mm
Thickness	3.97 mm
Corner Radius	0.20066 mm
Hole Diameter	4.39 mm

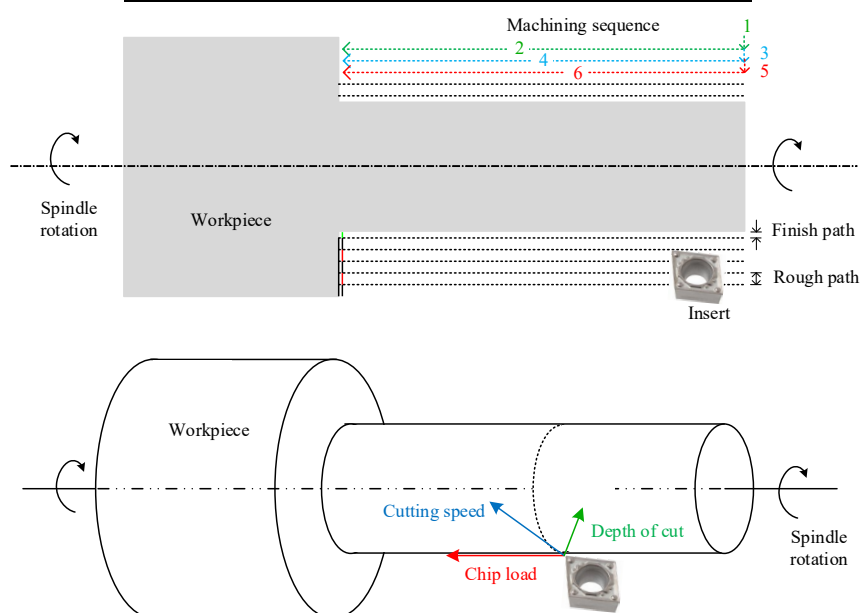


Figure 3-31 Protocol used in machinability tests.

Table 3-4 Parameters of machinability tests.

Material	Workpiece label	Insert label	Note	V_c (m/min)	Rough depth of cut (mm)	Finish depth of cut (mm)	Chip load (mm/rev)
NiTi	NT-1	I-NT-1	Only 1 specimen tested	60.96	1.016	0.508	0.1
	NT-2	I-NT-2	Only 1 specimen tested	30.48	1.016	0.508	0.1
	NT-3	I-NT-3	Only 1 specimen tested	15.24	1.016	0.508	0.1
	NT-4	I-NT-4	Only 1 specimen tested	10.67	1.016	0.508	0.1
CAM	CAM-1 to CAM-30	I-CM-30	30 specimens tested continuously *	60.96	1.016	0.508	0.1

MS	MS-1 to MS-30	I-MS-30	30 specimens tested continuously	60.96	1.016	0.508	0.1
----	---------------	---------	----------------------------------	-------	-------	-------	-----

Note: * The so called ‘continuously’ means that 30 specimens were machined in order, without changing the machining protocol.

The poor machineability of NiTi leads to serious wear of the insert quickly after starting the experiment. Measurable wear (or even fracture, as will be shown below) of the insert formed after only machining one piece of NiTi specimen. Therefore, only one sample was considered for the machinability tests on the NiTi at a given V_c . As shown in Table 3-4, four V_c were selected as the variable of machinability tests on NiTi. For each V_c , a brand-new insert was installed and only one piece of cylindrical sample was machined. At the end of each test, the insert was removed to observe the tip condition under the optical microscope. A HAYEAR 48MP 2K high-definition HDMI digital microscope with a maximum magnification of 150 times was used for this purpose.

As CAM and MS show higher machinability than NiTi, machining a single specimen (as was done for NiTi) was not sufficient to cause visible wear on the insert. As a result, 30 specimens were considered to examine the machinability of CAM and MS. The following procedure was conducted. Before the turning tests, a brand-new insert was installed. Then 30 CAM specimens were machined continuously with the same insert. The so called ‘continuously’ means that 30 specimens were machined in order without changing the machining protocol. After finishing all 30 CAM specimens, the insert was removed and measured under the optical microscope. The test procedure on MS was the same as that on CAM. For 30 CAM and 30 MS specimens after machining, a Mitutoyo IP65 micrometer (with a precision of 0.001 mm) was used to measure the diameter of each machined sample to quantitatively characterize the product quality.

3.3.3. Results for NiTi SEA

3.3.3.a. Chip condition

At high cutting speed ($V_c=60.96$ m/min), sparks are observed, and the chip completely melted due to the high temperature. After cooling down, some very thin purple-blue-colored chips were collected as shown in Figure 3-32(a). At $V_c=30.48$ m/min, some sparks and partial melting of the chips was observed during machining. Blue-yellow-colored chips collected at $V_c=30.48$ m/min are shown in Figure 3-32(b). At $V_c=15.24$ m/min, no sparks were observed but some smoke was seen. A blue colored chip was collected after cooling down as shown in Figure 3-32(c). At $V_c=10.67$ m/min, no sparks or smoke was observed. Long spring-like purple-brown-colored chips were produced as shown in Figure 3-32(d).



(a) $V_c=60.96$ m/min (b) $V_c=30.48$ m/min (c) $V_c=15.24$ m/min (d) $V_c=10.67$

Figure 3-32 Picture of chips obtained from NiTi machineability experiments: (a) $V_c=60.96$ m/min, (b) $V_c=30.48$ m/min, (c) $V_c=15.24$ m/min and (d) $V_c=10.67$ m/min.

3.3.3.b. Insert condition

Figure 3-33 shows the condition of insert I-NT-1 after machining NT-1 at $V_c=60.96$ m/min. It is seen that the insert is heavily damaged during machining the NiTi sample at $V_c=60.96$ m/min. The tip

of the insert broke completely during machining. The fractured part of the tip is over 2 mm on the front side, top side and right side, and is over 9 mm on the left side. Such heavy damage is actually caused by brittle fracture rather than normal wear.

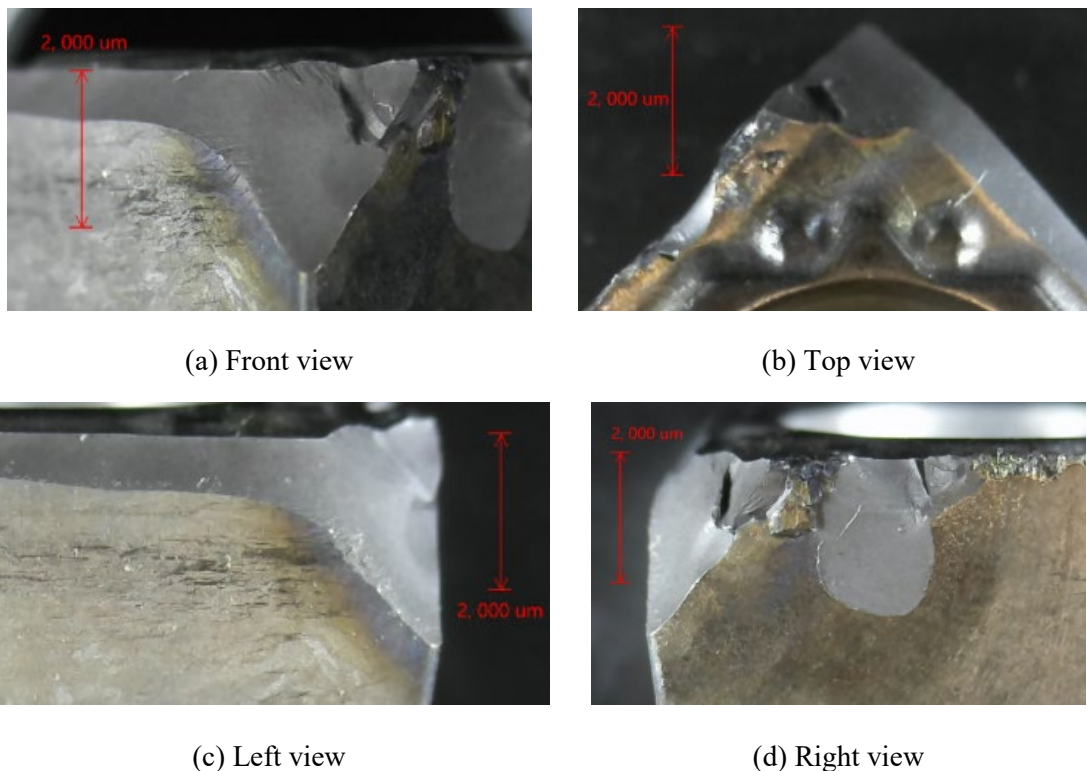


Figure 3-33 Condition of I-NT-1 after machining NT-1 at $V_c=60.96$ m/min, (a) front view, (b) top view, (c) left view and (d) right view.

Compared with Figure 3-33, the fracture of insert tip did not occur for I-NT-2; however, serious wear was observed. The wear on the front, top, left, and right side of the tip was all around 250 μm . Besides, some rough bumps with a size over 100 μm could be observed on the insert tip. The roughness and burrs on the tip of the insert are attributed to the melt during machining. During machining NT-3 at $V_c=15.24$ m/min, a brittle fracture with a size around 500 μm was observed on the tip of the insert. Because of the brittle fracture, no rough bumps caused by melting was observed. For I-NT-4, after machining NT-4 at $V_c=10.67$ m/min, the fracture of the insert tip did not occur and the insert tip was smooth after machining. No rough bumps were observed in comparison with that at $V_c=30.48$ m/min. The wear on the front side was around 200 μm , and the wear on the left and right side was around 400 μm .

As the cutting speed is decreased from $V_c=60.96$ m/min to $V_c=10.67$ m/min, the wear/fracture of the insert has reduced. However, even at the slowest machining condition ($V_c=10.67$ m/min), the wear of the insert tip was over 200 μm after only limited amount of machining of one sample, which indicates the high hardness and difficulty of machining of NiTi. Besides, it is worth noting that under all cutting speeds, the wear on the right side of insert was worse than that on the left side. The reason is that the left side is the movement direction of the insert while the right side is where the produced chips are in contact with. The friction caused by continuous, hard, and high temperature chips results in more significant wear than the contact with the specimen itself.

3.3.4. Results of CAM SEA and mild steel

3.3.4.a. Chip condition

Some very long chips were produced when machining CAM SEAs. The long chips were very strong and even rotated with the workpiece. This is attributed to the strength and superelasticity of CAM SEAs. Another interesting observation is a whistle-like noise produced when machining CAM. Figure 3-34 shows the chips collected from CAM-1, CAM-10, CAM-20 and CAM-30, respectively. It is seen that as the machining went on, the width of chips became thinner, and their spring-like shape disappeared. This may be attributed to the wear on the insert. Besides, all the chips had consistent gold-like color, no blue or purple color that is commonly caused by burning could be observed, which indicates that little to no heat was produced during machining CAM.

Machining mild steel under these conditions was very smooth. Figure 3-35 show the chips collected from MS-1, MS-10, MS-20 and MS-30, respectively. The surface of rotating mild steel peels very fast as it contacts the insert; therefore, the chips produced during machining mild steel were very short (0.5 to 2 mm). Besides, as the machining of mild steel continued, the color of the chips changed from mostly blue to brown-blue. The variation in the chip color is due to the heat accumulation during machining.

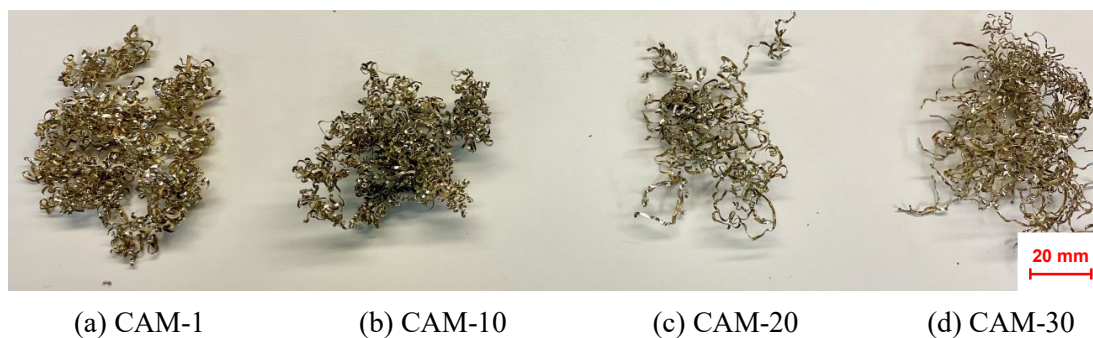


Figure 3-34 Chips produced during machining CAM SEA, (a) CAM-1, (b) CAM-10, (c) CAM-20 and (d) CAM-30.

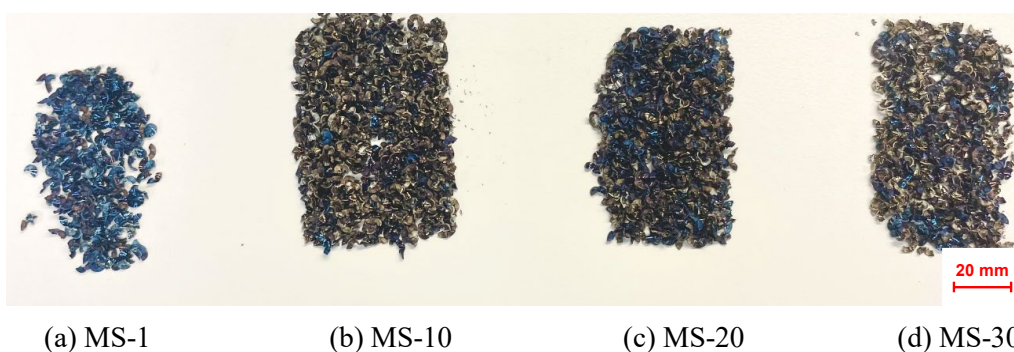


Figure 3-35 Chips produced during machining mild steel, (a) MS-1, (b) MS-10, (d) MS-20, and (d) MS-30.

3.3.4.b. Insert condition

Figure 3-36 shows the condition of I-CM-30 after machining 30 pieces of CAM specimens at $V_c = 60.96$ m/min. Some wear of the insert was observed; however, no fracture of the tip occurred. The wear of the insert was around 200 μ m after machining 30 Cu-Al-Mn specimens at the highest cutting speed considered ($V_c = 60.96$ m/min), which is comparable or even smaller than the wear produced by

machining only one piece of NiTi at the lowest cutting speed considered ($V_c = 10.67$ m/min). Figure 3-37 shows the condition of I-MS-30 after machining MS at $V_c = 60.96$ m/min. The wear of the insert I-MS-30 was around 100 μm , which was approximately one half of the wear for I-CM-30.

It is worth noting that for I-CM-30, the wear on the right side (around 400 μm) was obviously larger than that on the left side (around 200 μm). This phenomenon occurred on I-NT-2 and I-NT-4 but not on I-MS-30. The reason is that as long chips were produced during machining NiTi and CAM, severe wear occurred due to friction. On the other hand, while machining mild steel, the chips peeled very fast and they were very short in length (0.5 to 2 mm); therefore, no wear on the right side of the insert was produced.

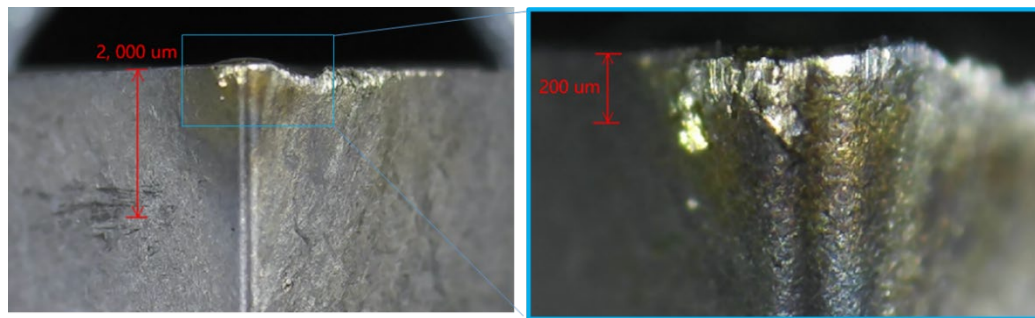


Figure 3-36 Condition of I-CM-30 at $V_c = 60.96$ m/min after machining 30 continuous workpieces.

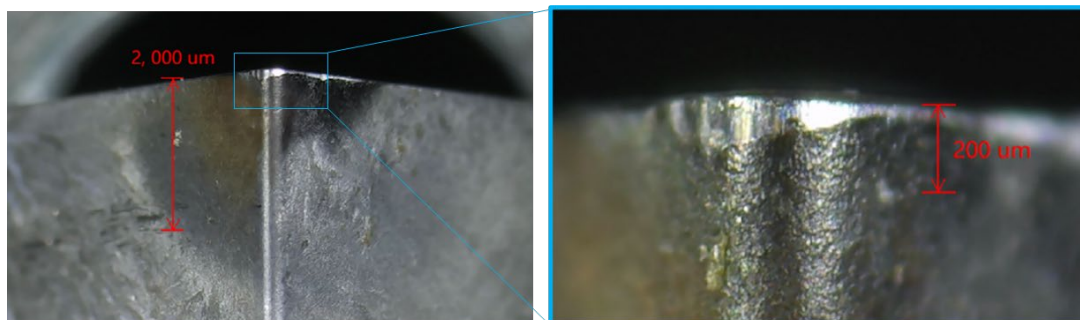


Figure 3-37 Condition of I-MS-30 at $V_c = 60.96$ m/min, after machining 30 continuous workpieces.

3.3.4.c. Visual observation of product surface

For CAM and MS specimens, to the naked eye, there was no visible variation on the product surface. In CAM-18 some very tiny local unsmooth bands (around 2 mm in width) were observed on the surface. Besides, some obvious burrs (less than 1 mm in width) started to occur at the edge, which indicates that the blunting of the insert was taking place. Starting with CAM-27, the burrs at the edge became larger, the width was over 2 mm and the length was over 10 mm.

3.3.4.d. Dimensional variation of end products

It is seen that the surface condition of workpieces after machining does not give sufficient information regarding the wear of the insert or the quality of the end product. Most of the specimens showed similar surface roughness that could not be distinguished by either the naked eye or optical microscope. The change in the diameter was obtained as the difference of the diameter of the measured sample and the diameter of the 1st specimen. A higher the difference in diameter indicates more tool wear, and correspondingly, poorer machinability of the material.

Three positions on the machined workpiece were selected and measured using a micrometer with a precision of 1 μm . The measurement points on the specimen are shown in the inset of Figure 3-38. At

each position (start, middle and end), the largest diameter was obtained by taking multiple measurements around the circumference.

Figure 3-38 shows the difference in diameter of 30 mild steel specimens. It is seen that as the machining progressed, the diameter of mild steel specimens at all three positions increased gradually. Figure 3-39 shows the difference in the diameter of 30 CAM specimens. Despite showing the same increasing trend, compared to mild steel, the difference in diameter of CAM exhibited a larger scatter. It was observed that from CAM-22 to CAM-23, there is a jump in the measurements at all three positions. The pictures of the surface of CAM-22 and CAM-23 are shown in the insets of Figure 3-39. Some rough bands were observed on the surface of CAM No. 23, which is attributed to a breakage or fracture of the insert tip.

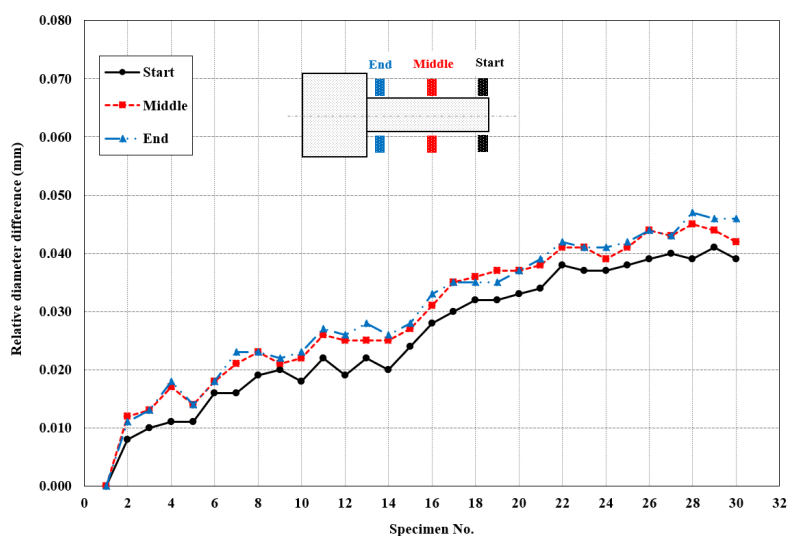


Figure 3-38 Change in diameter of 30 mild steel specimens after machining.

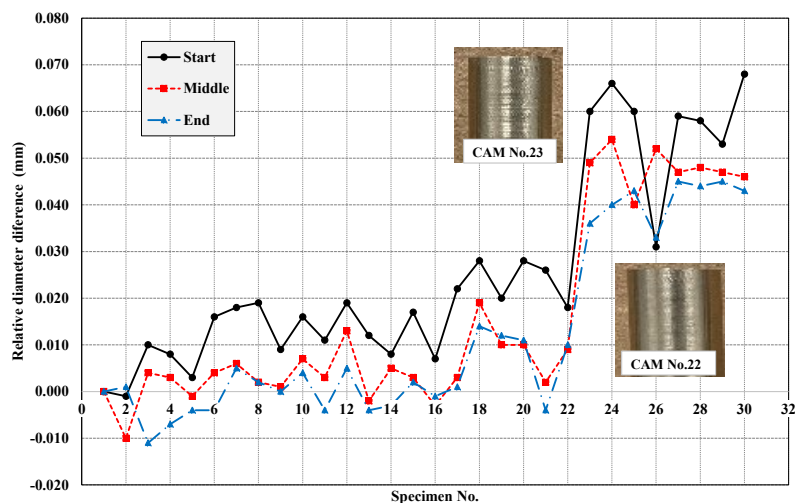


Figure 3-39 Change in diameter of 30 Cu-Al-Mn specimens after machining.

The average value of three diameter measurement positions was calculated for both materials and compared in Figure 3-40. It is seen in Figure 3-40 that after 30 pieces of continuous machining, the diameter increase of Cu-Al-Mn and mild steel was around 0.052 mm and 0.042 mm, respectively. The

machining of Cu-Al-Mn showed a larger scatter in diameter; however, the final increase of diameter was only around 10 μm bigger than that of mild steel.

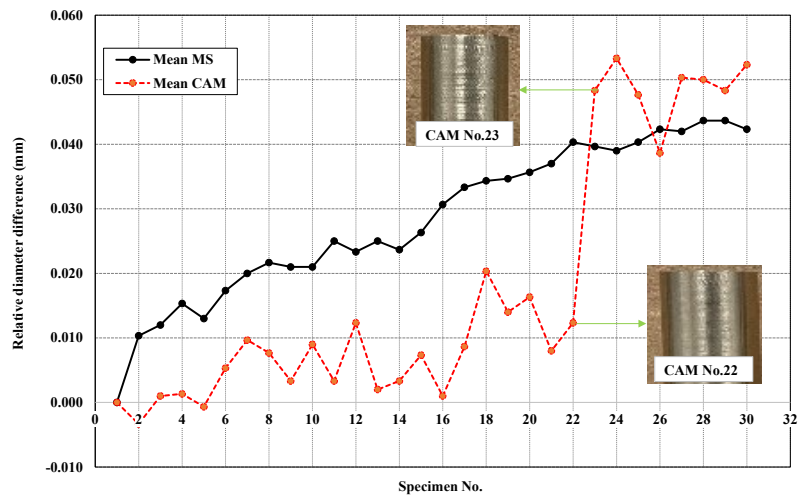


Figure 3-40 Mean value of diameter difference of Cu-Al-Mn and mild steel.

3.3.5. Summary

It has been confirmed in this study that machinability of NiTi SEA using standard machining tools is very difficult and causes extensive wear or breakage of the insert after only limited amount of machining. When machining NiTi at a cutting speed $V_c = 60.96$ m/min, the tip of the insert broke after machining only one specimen. While at this cutting speed, the wear on the insert tip was only around 200 μm after machining 30 specimens of CAM SEA. Machining NiTi at very low cutting speeds may decrease the wear of the insert, but the product quality was still not good. For example, when machining NiTi at a very low cutting speed of $V_c = 10.67$ m/min, some obvious scratches (larger than 4 mm) could be seen on the product surface. No alternative machining tools were attempted in this study to determine if a more appropriate set of tools are available for machining NiTi.

Compared with NiTi, the CAM showed higher machineability and better quality of products when using standard machining tools. The machineability of CAM was found to be comparable to that of conventional mild steel. After machining 30 specimens at a cutting speed of $V_c = 60.96$ m/min, the insert wear for CAM SEA was approximately twice that of mild steel. The friction resulted from the long chip produced during machining CAM doubled the wear on one side of the insert, but this did not affect the surface condition of the end products. All CAM specimens showed a smooth and shiny surface condition after being machined at a cutting speed of $V_c = 60.96$ m/min. The change in the diameter of CAM after machining 30 specimens was only around 10 μm more than that of mild steel.

3.4. COUPLING PERFORMANCE OF CAM ALLOYS

3.4.1. Introduction

In this chapter, the feasibility and performance of large diameter CAM SEA bars coupled with steel rebar are investigated. Two types of most commonly used coupling forms are considered; namely, threaded coupling and headed coupling. The large diameter CAM SEA bars were threaded or headed at the ends and then connected with steel rebar by mechanical coupler composed of a male and a female steel collar. Cyclic and monotonic tensile tests were conducted on the coupled specimens and the critical

mechanical properties were extracted and discussed. No testing of NiTi SEA for coupling performance has been performed in this research as this subject has been studied by others [22–25].

3.4.2. Specimen preparation and test methods

3.4.2.a. Specimen preparation

For headed end specimens, two large diameter single crystal CAM bars are considered: 20 mm and 30 mm, which were, respectively, coupled with 19 mm diameter (U.S. #6) and 32.3 mm diameter (U.S. #10) Grade 60 MS rebar. The composition and manufacturer of CAM SEA bars are the same as those presented earlier. The dimensions of the headed CAM SEA bars are shown in Figure 3-41(a) and (b). Each CAM SEA bar was headed at both ends and then connected to two headed steel rebar, referred to here as the top and bottom steel rebar. The MS rebar was headed at one end (the heading dimension was the same as the headed CAM SEA bar it was coupled with), and the other end was unmodified.

Five headed CAM specimens were prepared in this study, including four 20 mm diameter CAM SEA bars (labeled as HC20-1, HC20-2, HC20-3 and HC20-4) coupled with #6 steel rebar, and one 30 mm diameter CAM SEA bar (labeled as HC30-1) coupled with #10 steel rebar. Besides, since the mechanical properties of SEAs are sensitive to temperature, the superelastic performance of the CAM SEA may deteriorate during the heading process, which involves high temperature. To understand this variation and make a comparison, two threaded CAM SEA bars (labeled as TC20-1 and TC20-2) were also prepared and tested. The threaded CAM SEA bars were machined at room temperature, without experiencing any high temperature. The geometries of the threaded specimens are shown in Figure 3-41(c). The labeling of the headed or threaded specimens is done in three parts where the first part indicates headed coupling (HC) or threaded coupling (TC), the second part indicates the diameter in mm and the third part indicates the number of samples of this type. For example, for ‘HC20-1’, HC indicates the headed coupling, 20 means that it is a 20 mm diameter as received CAM SEA bar, 1 means the first specimen of this type; for ‘TC20-1’, TC indicates the threaded coupling, 20 means that it is made from a 20 mm diameter as received CAM SEA bar, 1 means the first specimen.

Heading of the CAM SEA bars and steel rebar was performed at the Headed Reinforcement Corp. (HRC) in Fountain Valley, California. Some pictures from the heading process are shown in Figure 3-42. The CAM SEA and steel rebar followed the same heading procedure. The as received CAM SEA bars and the steel rebar were heated by a blowtorch and then headed by a mechanical extruder. After that, the headed specimens were naturally cooled in the ambient temperature. A REED R2020 infrared thermometer with temperature range -50 °C to 3992 °C was used to monitor the surface temperature of the headed region of each specimen after removing from the extruder.

The surface temperature variation of CAM SEA specimens after heading with respect to the cooling time was measured. It was seen that after heading, the surface temperature of the headed region of five specimens ranged from 514 °C to 675 °C, the HC30-1 reached 859 °C. All headed specimens cooled down to room temperature in about 30 min.

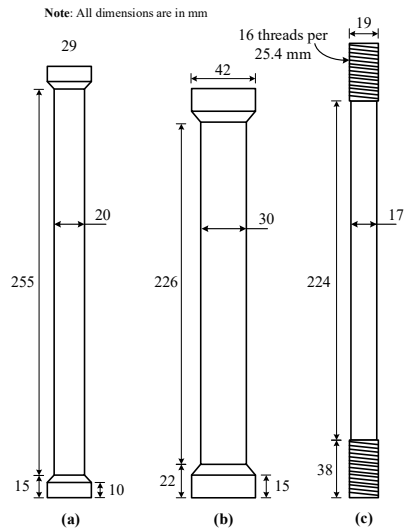


Figure 3-41 Dimensions of headed end CAM SEA bars for coupling tests: (a) 20 mm diameter headed bar, (b) 30 mm diameter headed bar, and (c) 20 mm diameter threaded bar.

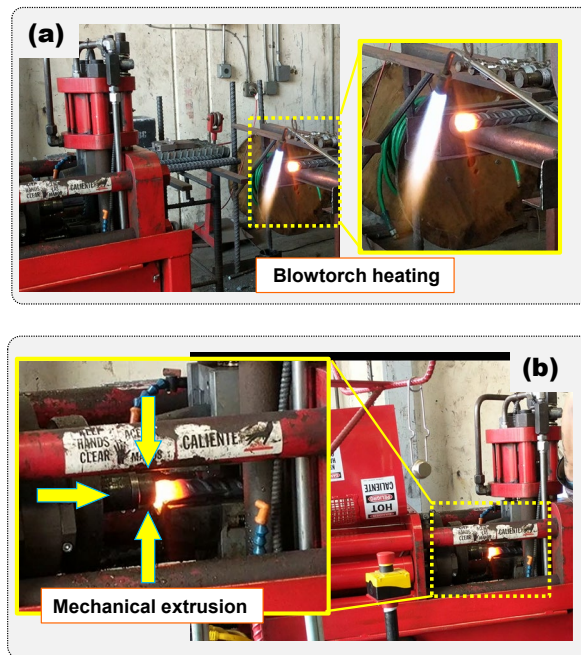


Figure 3-42 Pictures from heading process: (a) heating specimens by blowtorch, (b) heading specimens using a mechanical extruder.

3.4.2.b. Test methods

Three types of mechanical tests were conducted, namely, single coupling tests for threaded CAM SEA bars, single coupling tests for headed CAM SEA bars and double coupling tests for headed CAM SEA bars. The details of the three test methods are described as follows.

The test setup for the single coupling tests on threaded CAM SEA bars is shown in Figure 3-43. Since during each experiment, only one specimen was tested without being connected to other specimens, this test is called single coupling tests for brevity. The MTS loading frame and the 50.8 mm Epsilon extensometer presented earlier were also used for these tests.

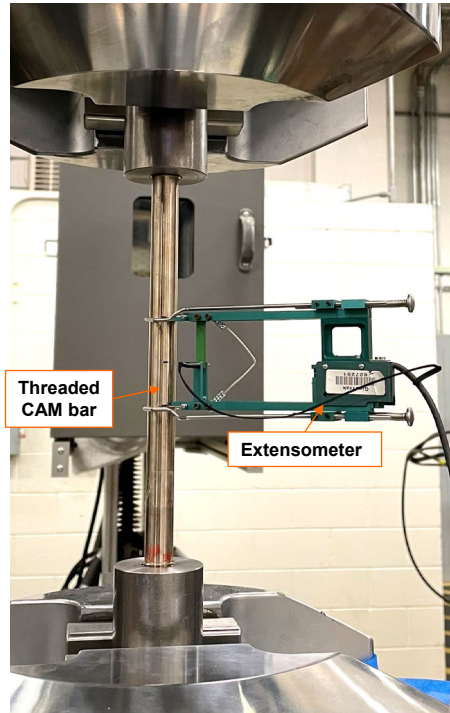


Figure 3-43 Setup for single coupling tests on threaded CAM SEA bar.

The loading protocol used in the single coupling tests on threaded CAM SEA bars is shown in Figure 3-44, which involved increasing tensile strain cycles with 1% increments up to a maximum strain amplitude of 5%. The loading rate was 0.4 mm/sec. This loading protocol is also referred to as training.

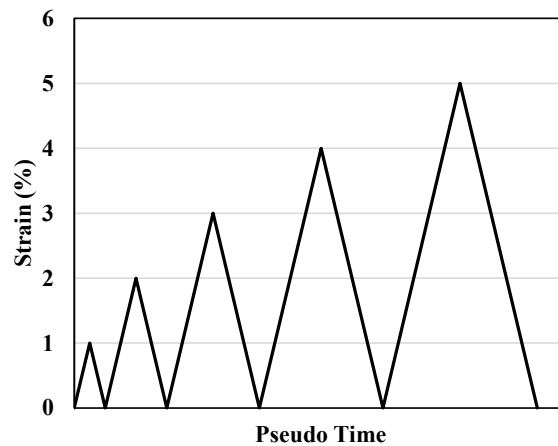


Figure 3-44 Loading protocols used for training CAM SEA bars in coupling tests.

For single coupling tests on headed CAM SEA specimen, the headed CAM SEA bar is coupled with two headed steel rebar at the two ends; however, since only one CAM SEA specimen is involved, it is referred to as a single coupling test. To connect the middle CAM SEA bar with bottom and top steel rebar, a mechanical coupler composed of a male and a female threaded steel collar was used, as shown in Figure 3-45.

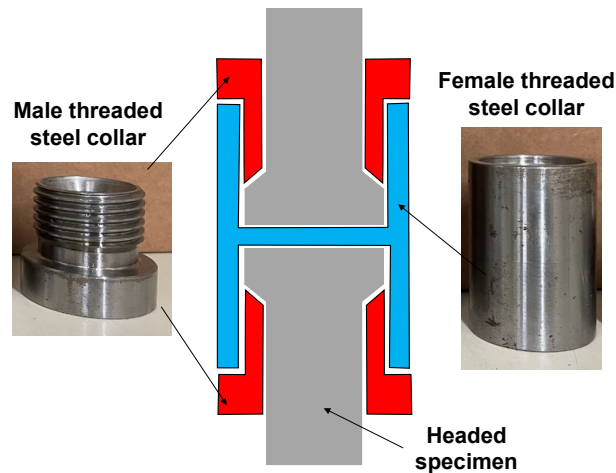


Figure 3-45 Mechanical coupler used to connect headed specimens.

The test setup for single coupling tests on headed CAM SEA bars is shown in Figure 3-46. The loading frame and extensometer were the same as those used in the single coupling tests on threaded CAM SEA bars. An extensometer was used to monitor the strain of the headed CAM SEA bar; while, two strain gauges were applied on the top and bottom steel rebar to ensure they do not yield before the fracture of the middle CAM SEA bar. The reason is that in a real-life application, the CAM SEA bar is coupled with a steel rebar in the plastic hinge region of the column. The deformation should be concentrated on the CAM SEA bar to take full advantage of its superelastic behavior. Strain gages were sourced from Omega Engineering (model number: KFH-6-350-C1-11L3M3R) with a gauge length of $\pm 1\%$ and a resistance of $350\ \Omega$. They were used with the same data acquisition module described earlier.

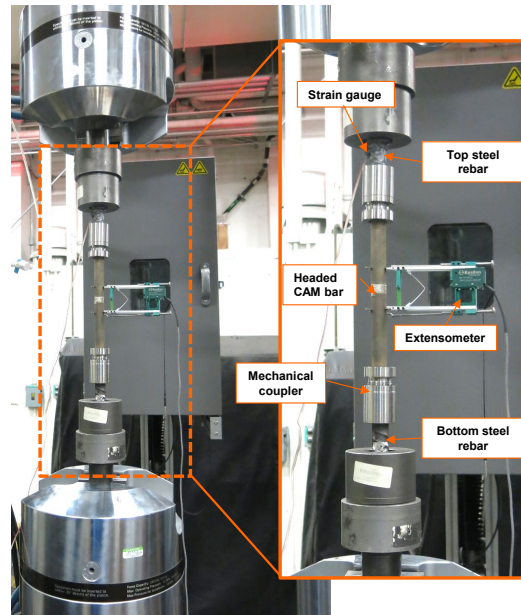


Figure 3-46 Setup for single coupling tests on headed CAM SEA bars.

Two loading protocols were considered in the single coupling tests on headed CAM SEA specimen. One is the training, as shown in Figure 3-44. The other one is the constant tensile strain cycles with an amplitude of 5%, as shown in Figure 3-47. During both loading protocols, the strain gauges on the steel rebar were monitored to ensure the steel rebar did not yield before the CAM SEA bars. In the single coupling tests on the headed CAM SEA specimens, the training protocol was first applied. If the strain gauges reached close to yield strain of the steel rebar, the test was paused, and the CAM SEA bars were

heat treated to reduce the yield strength. The heat treatment temperature was 130°C with a duration of 45 minutes. After the heat treatment, the training was repeated. If the specimens were still intact after the training, the testing was continued with the constant amplitude strain cyclic loading protocol.

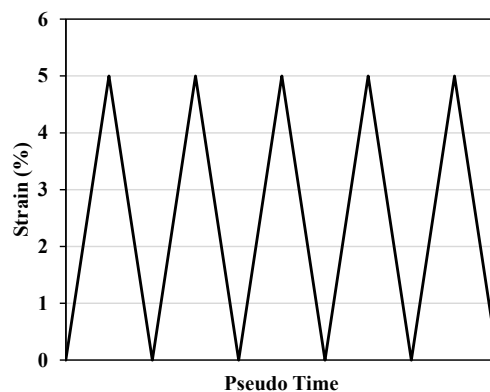


Figure 3-47 Constant amplitude cyclic tensile loading protocol for coupling tests.

For the headed CAM SEA bars that were still intact after the single coupling tests, they were spliced in series with a mechanical coupler and tested under monotonic tensile loading until fracture. Since two CAM specimens were tested in series, this test method is referred to as the double coupling. The test setup for the double coupling tests on headed CAM SEA bars is shown in Figure 3-48. In the double coupling tests, two 50 mm gauge length Epsilon extensometers presented earlier were installed in the middle of the two headed CAM SEA bars. Besides, a CELESCO Model No. CLWG-225-MC4 linear potentiometer with 228.6 mm stroke was installed at the end of the grip fixture, as shown in Figure 3-48.

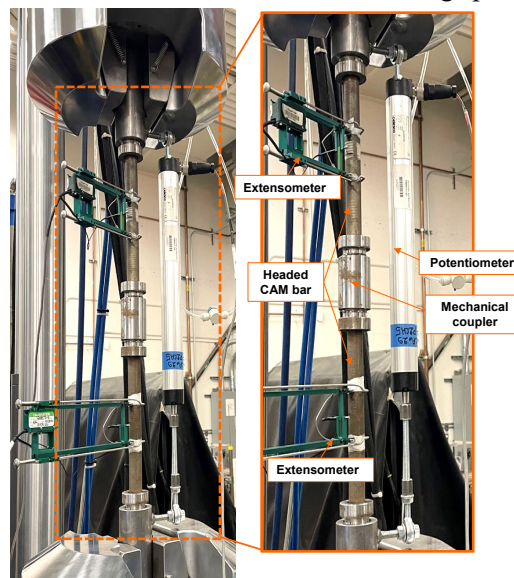


Figure 3-48 Test setup for double coupling tests on headed CAM SEA bars.

3.4.3. Results of threaded CAM SEA specimens

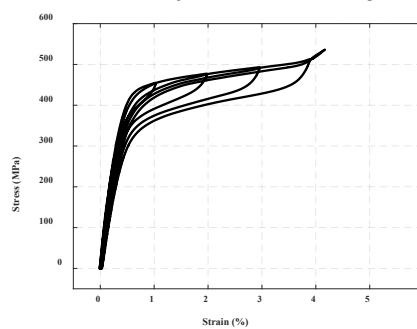
Both specimens showed flag-shaped stress-strain curves as expected. The residual strain of both specimens was less than 0.25%. The σ_{Ms} of TC20-1 and TC20-2 were 336.8 MPa and 311 MPa, respectively. The E_{load} of TC20-1 and TC20-2 were 27.4 GPa and 27.6 GPa, respectively. After yielding, both specimens showed a flat stress-strain plateau, the E_{load2} of TC-1 and TC20-2 were 0.9 GPa and 0.7 GPa, respectively.

3.4.4. Results of headed CAM SEA specimens

3.4.4.a. Single coupling tests

HC20-1

Figure 3-49 shows the first training results of HC20-1. From Figure 3-49, it is seen that the HC20-1 has a higher yield stress and elastic modulus than the threaded CAM SEA bar. The σ_{Ms} of HC20-1 reached 445.7 MPa, which is 40% more than the average of TC20-1 and TC20-2. The E_{load} of HC20-1 reached 98.7 GPa, which is 3.6 times of the average of that of TC20-1 and TC20-2. It should be noted that only for this specimen the test continued after the yielding of the top and bottom steel rebar. The tests on the rest of specimens were all paused, and the CAM SEAs were reheat treated if the steel rebar was close to yielding. Figure 3-49(b) shows the image of HC20-1 after fracture, the specimen failed at the headed region. The fracture strain of HC20-1 was about 4.5%.



(a) CAM SEA bar



(b) Image after fracture

Figure 3-49 Training results of HC20-1: stress strain curves of (a) middle CAM bar, and (b) image of the specimen after fracture.

HC20-2

After heat treatment, the HC20-2 was trained again. The second training results of HC20-2 is shown in Figure 3-50. The HC20-2 fractured during the 5th cycle of the second training. It is seen that after heat treatment, the deformation was concentrated in the CAM SEA bar and the steel rebar did not reach the yield strain when the strain in the CAM SEA bar was over 4%. The E_{load} of HC20-2 decreased from 58.2 GPa to 35.5 GPa, which means that the heat treatment effectively reduced the yield strength of the CAM SEA bar. The fracture strain of HC20-2 was about 4.5%. An image of HC20-2 after fracture is shown in Figure 3-50. The failure also took place in the headed region, the same as HC20-1.

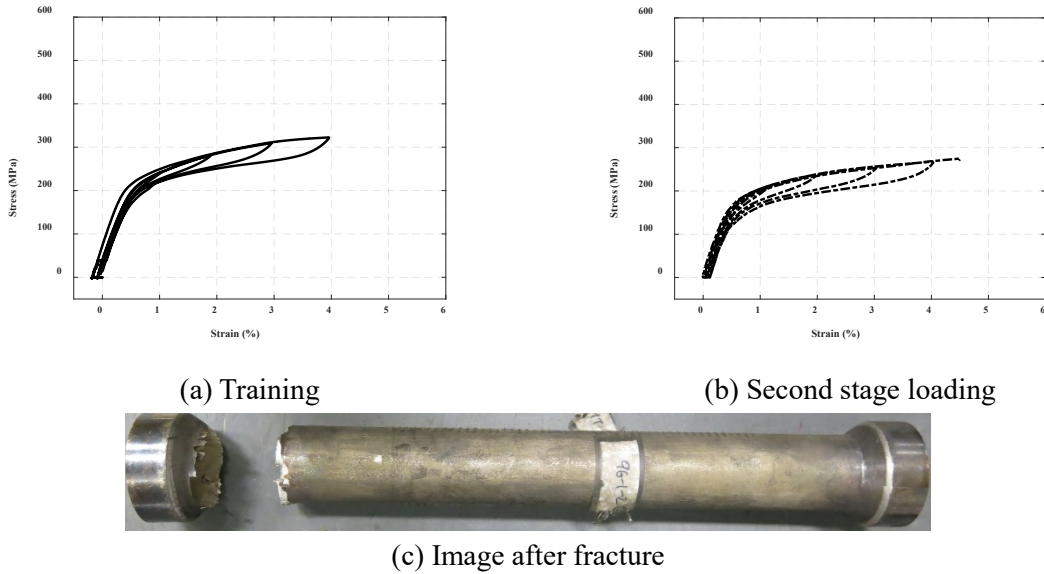


Figure 3-51 Results of HC30-1: (a) first training, (b) second stage loading, and (c) specimen after fracture.

3.4.4.b. Double coupling tests

Since the HC20-3 and HC20-4 were still intact after the training and subsequent loading, double coupling tests were conducted on these two specimens. The double coupling test results are shown in Figure 3-52. The data collected from the two extensometers and one potentiometer is presented. It is seen that the strain measured by two separate extensometers correlates well with the strain measured by the potentiometer, indicating the deformation on the two coupled headed CAM SEA bars as a system is relatively uniform across the length of the specimen. The ultimate stress and strain of the double coupled headed CAM SEA bars was over 450 MPa and 10%, respectively, which are very comparable to Grade 60 steel rebar.

In the double coupling tests, the fracture occurred on HC20-3 and the HC20-4 was still intact after the test as shown in Figure 3-53. It should be noted that the failure was not located in the headed region of HC20-3. Obvious necking was observed in the fracture zone, which is different than the brittle fracture observed in the other specimens, i.e., HC20-1, HC20-2, and HC30-1, which fractured in or very close to the headed zone.

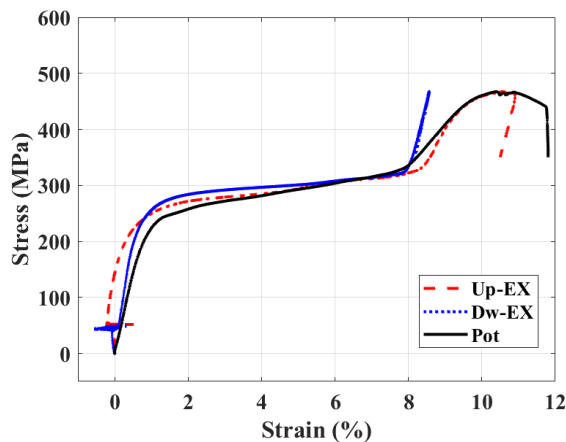


Figure 3-52 Double coupling test results of HC20-3 and HC20-4. Up Ex and Dw Ex denote the results respectively collected from the upper extensometer installed on HC20-3 and lower extensometer installed on HC20-4. Pot denotes the results collected by the linear potentiometer.

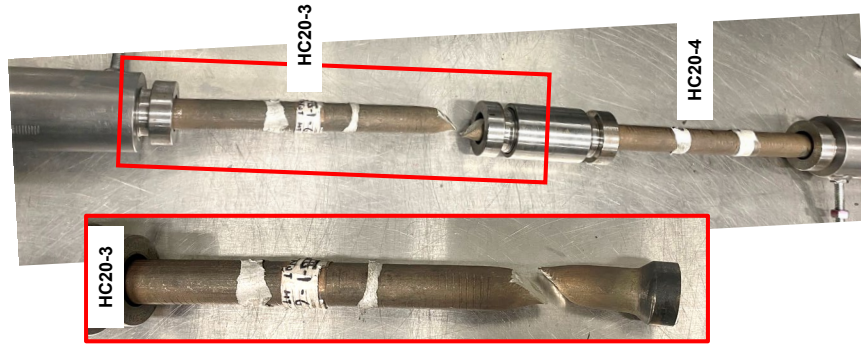


Figure 3-53 After fracture image of double coupling test specimens HC20-3 and HC20-4.

3.4.5. Summary

This study investigated the feasibility of coupling a large diameter CAM SEA bar with steel rebar. It was found that the heading process generally increases the elastic modulus of CAM SEAs, the elastic modulus of one of the specimens was over three times that of before heading. The rest of the four specimens also showed more than 30% increase in the elastic modulus after being headed. The post-heat treatment at 130°C with a duration of 45 min helped reduce the yield strength of the material. With a post-heat treatment, a 40% decrease in the elastic modulus could be achieved.

Additionally, it is concluded that the heading process has almost no influence on the strain recovery of CAM SEAs. The five headed specimens all had the same residual strain less than 0.3% after being loaded to more than 4% strain. However, the fracture strain of CAM SEA decreased after heading. In five large diameter headed CAM SEA specimens, three were fractured during the first training or during the second training after heat treatment. The fracture strain of these three specimens were around 4.5%. Brittle failure of all three specimens occurred in the headed end region. A perfect alignment of the axis of the specimens with the axis of the heading could not be achieved for some specimens. This may have caused additional stresses around the headed region due to bending in addition to the stresses due to tension.

Out of the five CAM SEA specimens, two 20 mm diameter headed specimens showed relatively ductile behavior under both cyclic and monotonic loading. The ultimate stress and strain of two headed CAM SEA specimens reached 450 MPa and 10%, respectively. Nevertheless, to further understand the heading effect on the superelasticity of CAM SEAs and ensure the reliability of the headed coupling method on large diameter CAM SEAs with steel rebar, more research is required. Heat treatment optimization is necessary to find out the conditions needed to avoid brittle fracture in large diameter bars. The success in coupling CAM SEAs together or with steel using headed couplers promises that this approach could lead the path for the implementation of CAM SEAs in real bridges and buildings.

3.5. COST ESTIMATION OF CAM SEAS IN TYPICAL BRIDGE COLUMNS

3.5.1. Introduction

This chapter investigates the cost of applying CAM SEA and NiTi SEA in typical bridge columns. The cost of producing, processing, and coupling, SEAs were considered. Three typical bridge columns were designed; namely, a conventional steel RC, the CAM SEA RC, and the NiTi SEA RC. The three typical bridge columns satisfy the same external load. The cost of CAM SEA RC column, NiTi SEA RC column, and steel RC column is discussed in detail.

3.5.2. Design of bridge columns

3.5.2.a. Material properties and geometric properties

The loads, geometry and material properties of the typical bridge column were selected based on the NCHRP Research Report 864 [26]. The factored loads applied on the column are 2577 kN-m bending moment and 5542 kN axial load. The column diameter is $D=1219$ mm; the column height is $L=5791$ mm and the concrete cover is $c=51$ mm. The diameter of transverse reinforcement is $d_w=22.2$ mm (U.S. #7). Regarding the material properties, the compressive strength of concrete is $f_{cc}=27.6$ MPa, and the yield strength of longitudinal and transverse reinforcement is $f_{yl}=f_{yt}=414$ MPa. The yield strengths of CAM SEA and NiTi SEA are $f_{yCAM}=280$ MPa and $f_{yNiTi}=380$ MPa, respectively. The elastic moduli of CAM SEA and NiTi SEA are $E_{CAM}=51.2$ GPa and $E_{NiTi}=37.9$ GPa, respectively. Because the yield strength of steel rebar is higher than those of CAM SEA and NiTi SEA, columns reinforced with SEAs have a lower lateral strength than those reinforced with steel. Therefore, to make a fair comparison of bridge columns with different reinforcements, all columns were designed for the same bending moment. This has resulted in steel RC, NiTi SEA RC and CAM SEA RC columns to have, respectively, 12, 33 and 42 longitudinal bars and 1.04%, 1.49% and 1.90% longitudinal reinforcement ratio, as shown in Figure 3-54. The clear distance between the longitudinal bars for steel RC, CAM SEA RC and NiTi SEA RC is 280.1 mm, 83.0 mm, and 59.1 mm, respectively.

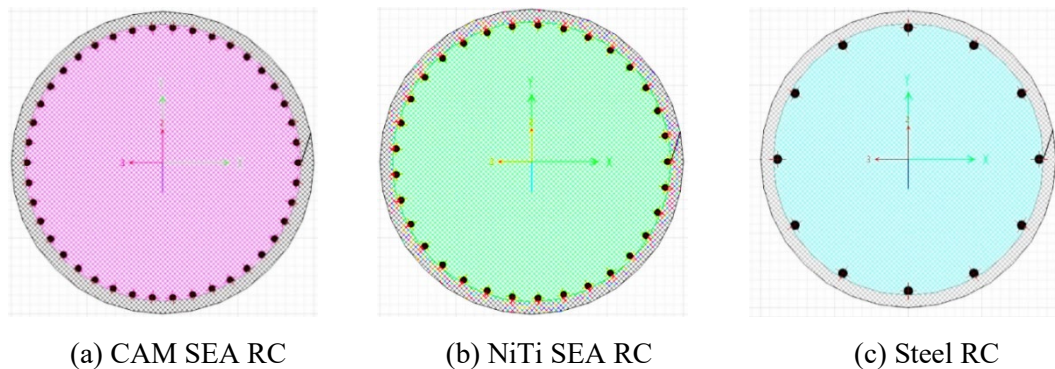


Figure 3-54 Sectional configuration of designed columns: (a) CAM SEA RC, (b) NiTi SEA RC, and (c) steel RC.

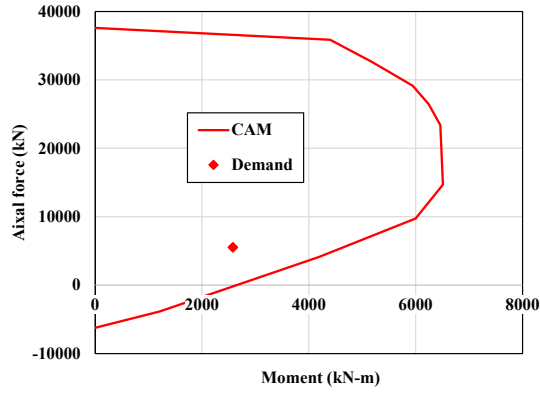
3.5.2.b. Capacity check

According to the NCHRP Research Report 864 [26], the axial capacity of the columns is calculated according to

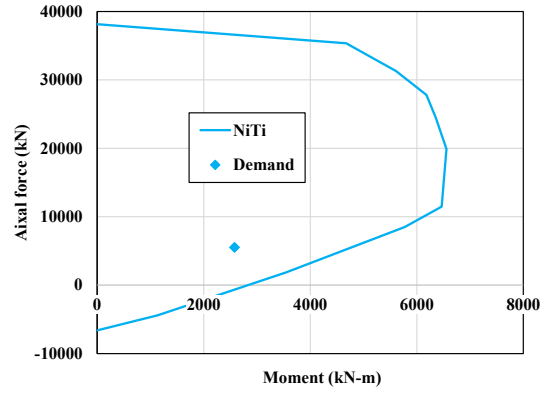
$$\phi P_{on} = 0.75(z_1 f_{cc}(A_g - A_l) + A_l f_{yl}) \quad \text{Eq. 7-1}$$

where f_{cc} is the nominal compressive strength of concrete, z_1 is the upper limit strength modifier, A_g is the gross area of the cross-section, A_l is the area of the longitudinal reinforcement, and f_{yl} is the nominal austenitic yield strength of SEA bars.

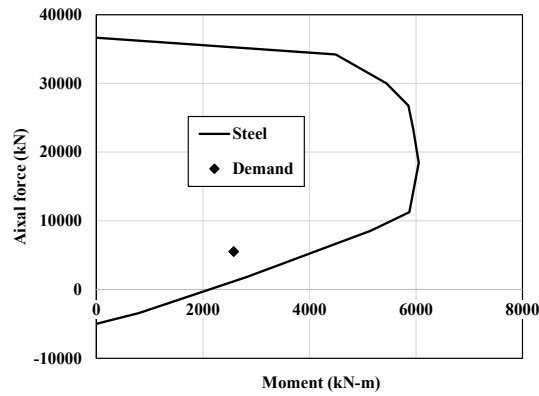
The axial demand to axial capacity ratio, D/R , for the three columns are, respectively, $D/R_{CAM}=0.196$, $D/R_{NiTi}=0.188$, and $D/R_{Steel}=0.204$. Figure 3-55 shows the axial force-bending moment interaction curves of the three designed columns, which were generated using a sectional analysis program. The constitutive model for different materials is the same as those used in the moment-curvature analysis, which will be presented in the following section. As seen from the interaction diagrams, all three designed columns satisfy the requirements.



(a) CAM RC



(b) NiTi RC



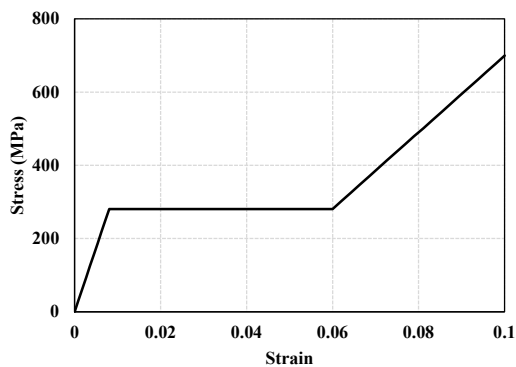
(c) Steel RC

Figure 3-55 Axial force-bending moment interaction diagram of designed columns: (a) CAM SEA RC, (b) NiTi SEA RC, and (c) steel RC.

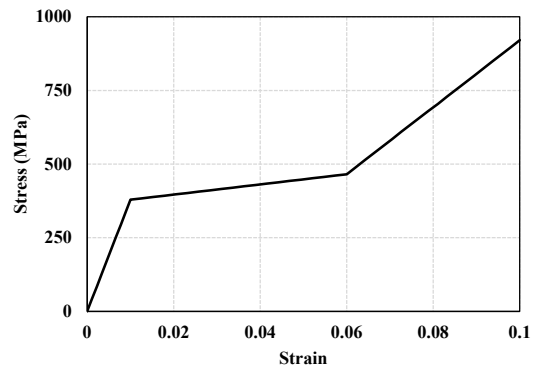
3.5.3. Analysis of bridge columns

3.5.3.a. Moment-curvature analysis

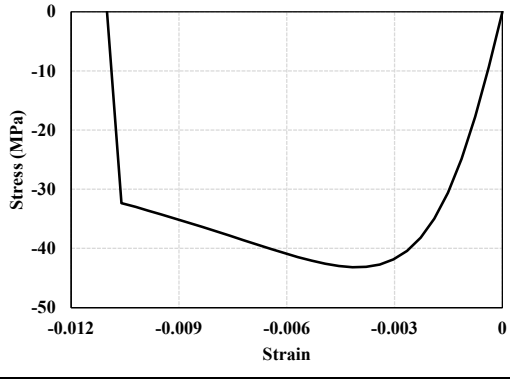
A sectional analysis was conducted to obtain the moment-curvature response of the designed columns. Constitutive models were adopted for different material following the NCHRP Research Report 864 [26]. In total, three different materials were considered; namely, unconfined concrete cover, confined concrete core, and the longitudinal reinforcement (including CAM SEA and NiTi SEA bars and steel rebar). The stress-strain curves of different materials for sectional analysis are shown in Figure 3-56.



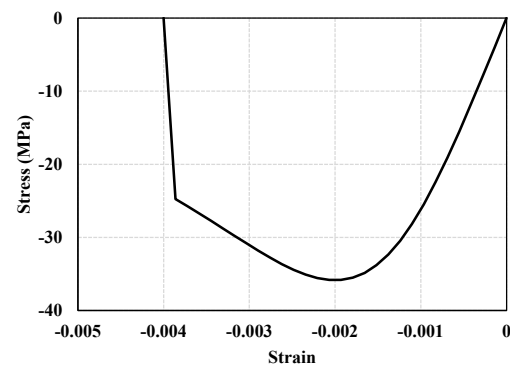
(a) CAM SEA



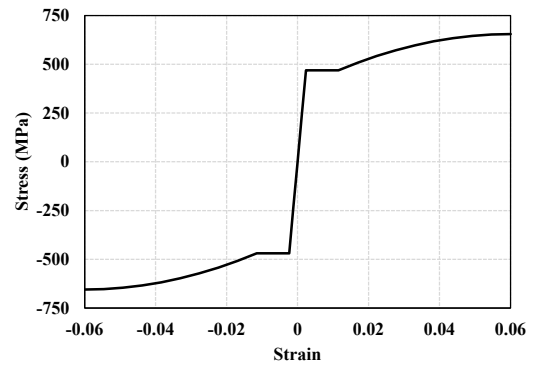
(b) NiTi SEA



(c) Confined concrete



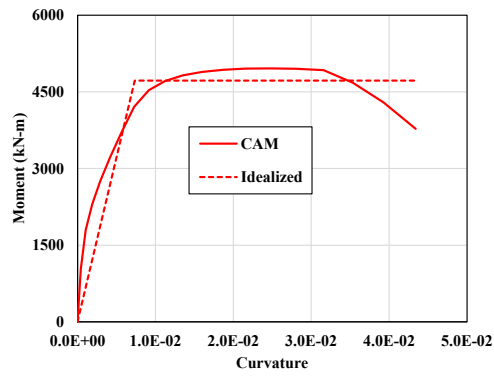
(d) Unconfined concrete



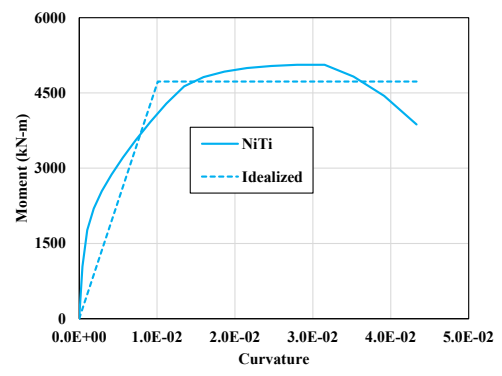
(e) Steel rebar

Figure 3-56 Constitutive models used in sectional analysis: (a) CAM SEA, (b) NiTi SEA, (c) confined concrete, (d) unconfined concrete, and (e) steel rebar.

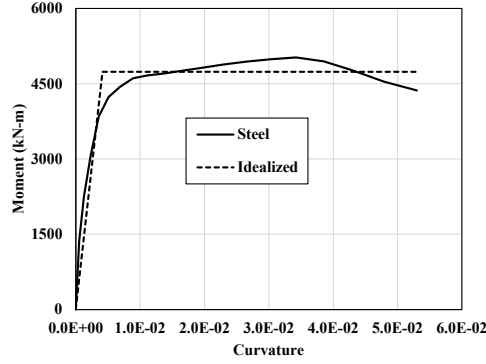
Using the above material properties and the applied axial load, the moment-curvature diagrams of three columns were obtained as shown in Figure 3-57. The idealized bilinear curves are also shown. From the idealized bilinear moment-curvature diagrams, it is seen that with the selected cross-sectional configurations, the three types of columns have almost identical plastic moment capacity.



(a) CAM SEA RC



(b) NiTi SEA RC



(c) Steel RC

Figure 3-57 Moment-curvature diagrams of three types of columns: (a) CAM SEA RC, (b) NiTi SEA RC, and (c) steel RC.

3.5.3.b. Drift capacity

Available formulations were used to roughly estimate the drift ratio of the columns based on the idealized bilinear moment-curvature diagrams. For the conventional RC column, the deformation was assumed to be localized in the plastic zone, also referred to as the plastic hinge. This simplification works well for conventional RC columns for two reasons. First, the deformed steel rebar shows strain compatibility with the concrete. Second, the localized deformation assumption well approximates the actual deformation along the length of the column. On the other hand, SEA bars have a smooth surface, and they are usually intentionally deboned from the concrete to further localize cracks [1]. The development of more accurate formulations to predict the SEA reinforced column response is outside the scope of this study. Further, the objective here is to perform a cost comparison of the three types of RC columns; therefore, only a rough estimation of the column deformations is required.

According to NCHRP Research Report 864 [26], the plastic hinge length L_p of steel RC column is obtained as

$$L_p = \max\{ 0.3f_{yl}d_{yl}, 0.08L + 0.15f_{yl}d_{yl} \} \quad \text{Eq. 7-2}$$

where f_{yl} and d_{yl} are, respectively, the yield strength and the diameter of the steel rebar; and L is the column height. Similarly, the displacement, Δ , at the top of the column is obtained as

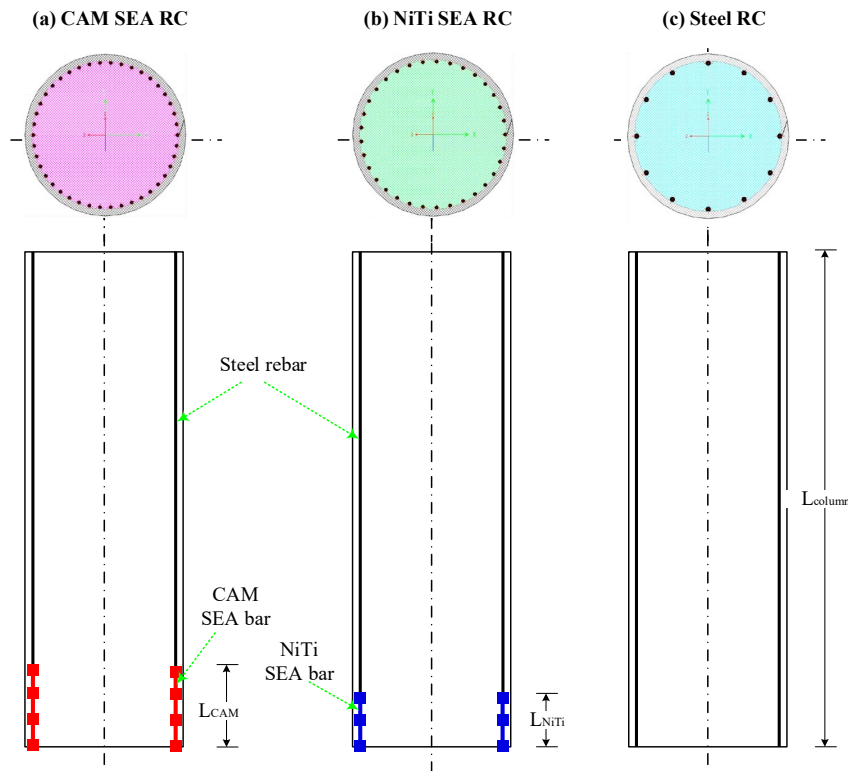
$$\Delta = \frac{\varphi_y L^2}{3} + (\varphi_u - \varphi_y)L_p(L - \frac{L_p}{2}) \quad \text{Eq. 7-3}$$

where φ_y is the idealized yield curvature and φ_u is the idealized ultimate curvature when concrete reaches the ultimate strain 0.01.

For the steel RC column, the plastic hinge length, $L_{p, steel}$, the displacement at the top end of the column, Δ_{steel} , and the drift ratio, δ_{steel} , were, respectively, obtained as 786 mm, 166 mm and 2.863%. For the SEA RC column, targeting the same displacement at the top end of the column as in the steel RC column, the length of the CAM SEA and NiTi SEA bars were obtained as 674 mm and 514 mm, respectively.

Figure 3-58 shows the arrangement of longitudinal reinforcement for the three types of bridge columns. For SEA reinforced columns, the CAM SEA and NiTi SEA were only applied in the plastic hinge region while the remaining length was steel rebar. Because the most commonly available CAM SEA and NiTi SEA are 30 cm long, the CAM SEA and NiTi SEA have to be spliced to reach the desired length. Hypothetically, mechanical couplers were used to splice the CAM SEA and NiTi SEA, as shown

in Figure 3-58. For CAM SEA RC, three pieces of SEA bars and four mechanical couplers were needed. For NiTi RC, two pieces of SEA bars and three mechanical couplers were needed.



Note: This figure is not drawn to scale

Figure 3-58 Arrangement of longitudinal reinforcement for three types of columns, (a) CAM SEA RC, (b) NiTi SEA RC, and (c) steel RC.

After obtaining the length of the SEA bars, the price of each column could be evaluated based on how much materials and machining are used.

3.5.4. Cost estimation of typical columns

It was assumed here that the difference in the cost of the three columns is only due to the longitudinal reinforcement. This assumption is approximate because the use of SEA reinforcement may alter other aspects of construction. The cost of SEA reinforcement includes: SEA bars, machining or heading, and mechanical couplers. In the following sections, the cost of three types of reinforcement was estimated.

The cost of steel RC columns was obtained as follows. Price of each steel reinforcement E_{steel} is computed by

$$E_{steel} = W_{steel} \times P_{steel} \quad \text{Eq. 7-4}$$

$$= L \times \pi \times \left(\frac{d_{steel}}{2}\right)^2 \times \frac{1}{1000} \times \rho_{steel} \times \frac{1}{1000} \times P_{steel} \quad \text{Eq. 7-5}$$

where W_{steel} is the weight of each steel reinforcement, N_{steel} is the number of steel rebar (i.e., 12), d_{steel} is the diameter of steel rebar (i.e., 36 mm), ρ_{steel} is the density of steel rebar (i.e., 7.8 g/cm³), and P_{steel} is the price of steel rebar \$2.2 /kg. The total cost for all steel rebar T_{steel} is computed by

$$T_{steel} = E_{steel} \times N_{steel} \quad \text{Eq. 7-6}$$

For CAM SEA and NiTi SEA reinforced columns, two types of coupling methods were considered; namely, headed end coupling (referred to as heading method hereafter) and dog-bone machined coupling (referred to machining method hereafter). The heading method involves firstly heading the two ends of SEA bars and steel rebar, then using mechanical couplers to connect them. The machining method involves firstly machining the SEA bars into dog-bone shape, then threading the two ends, and finally using mechanical couplers to connect SEA bars together and SEA bars and steel rebar. The difference of these two methods is the effective cross-sectional area of the SEA bars and the type of couplers and labor involved in the coupling. Because the machining method results in a smaller cross-sectional area, the cost on SEA material and coupling are different.

When using machining, the 30 mm diameter as received CAM SEA bars were reduced to an effective diameter of 26 mm. The steel in the remaining length was U.S. #9 rebar with a diameter of 28.7 mm. The cost of CAM SEA RC columns was calculated as shown below. When using machining, the cost of each reinforcement bar $E_{CAM-machine}$ constitutes four parts: the cost of CAM SEA material $E_{material}$, the cost of machining $E_{machining}$, the cost of mechanical coupler $E_{coupler}$, and the cost of the remaining steel rebar $E_{remainsteel}$. The cost of CAM SEA material $E_{material}$ is obtained as

$$E_{material} = L_{CAM} \times \pi \times \left(\frac{d_{CAM-machine}}{2}\right)^2 \times \frac{1}{1000} \times \rho_{CAM} \times \frac{1}{1000} \times P_{CAM} \quad \text{Eq. 7-7}$$

where N_{CAM} is the number of CAM SEA bars (i.e., 42), L_{CAM} is the length of CAM SEA in the plastic hinge region (i.e., 674 mm), n_{CAM} is the number of CAM SEA bars in each longitudinal rebar (i.e., 3), d_{steel} is the diameter of steel rebar (i.e., 28.7 mm (U.S. #9)), ρ_{CAM} is the density of CAM SEA (i.e., 7.1 g/cm³), and P_{CAM} is the price of CAM SEA (i.e., \$66.14 /kg). Note that the diameter of CAM SEA before machining is 30 mm, after machining it is 26 mm.

The cost of machining CAM SEA $E_{machining}$ is obtained as

$$E_{machining} = P_{machine-CAM} \times n_{CAM} \quad \text{Eq. 7-8}$$

where $P_{machine-CAM}$ denotes the price of machining each piece of CAM SEA. The cost of machining usually includes four parts; namely, cost of setup, C_{setup} , cost of machining, $C_{turning}$ (turning is considered in this study), cost of inserts, C_{insert} , and cost of cutting the machined specimens into designed length, $C_{cutting}$.

When machining CAM SEA, the four parts of machining cost were respectively taken as C_{setup} =\$120 /h, $C_{turning}$ =\$120 /h, C_{insert} =\$10 /each, $C_{cutting}$ =\$0 (cutting CAM SEA is as easy as cutting steel, therefore, no extra cost was added). For each piece of CAM SEA machining, only one setup work and one piece of insert is needed. The time required for each piece of CAM SEA machining was taken as 0.25 h. 100 specimens were considered to compute the average price of machining CAM SEA. Therefore, the price of machining each piece of CAM SEA is obtained as

$$P_{machine-CAM} = \frac{C_{setup}+C_{turning}+C_{insert}+C_{cutting}}{100} \quad \text{Eq. 7-9}$$

The cost of machining CAM SEA $E_{machining}$ is obtained as

$$E_{machining} = 46 \times n_{CAM} \quad \text{Eq. 7-10}$$

The cost of mechanical coupler $E_{coupler}$ is obtained as

$$E_{coupler} = P_{coupler} \times (n_{CAM} + 1) \quad \text{Eq. 7-11}$$

where $P_{coupler}$ is the cost of the couplers (both for machining and heading) was estimated as \$10/bar which includes two couplers per bar, one for each end.

The cost of remaining steel rebar $E_{remainsteel}$ is obtained as

$$E_{remainsteel} = (L - L_{CAM}) \times \pi \times \left(\frac{d_{steel}}{2}\right)^2 \times \frac{1}{1000} \times \rho_{steel} \times \frac{1}{1000} \times P_{steel} \quad \text{Eq. 7-12}$$

Therefore, the cost of each CAM reinforcement $E_{CAM-machine}$ is obtained as

$$E_{CAM-machine} = E_{material} + E_{machining} + E_{coupler} + E_{remainsteel} \quad \text{Eq. 7-13}$$

Total cost of all reinforcement when using machining $T_{CAM-machine}$ is computed by

$$T_{CAM-machine} = E_{CAM-machine} \times N_{CAM} \quad \text{Eq. 7-14}$$

When using heading, a smaller number of SEA bars is required, because the heading method does not reduce the effective cross-sectional area. The number of CAM SEA bars N_{CAM} is 32. The diameter of CAM SEA before and after heading is all 30 mm. The diameter of remaining steel rebar d_{steel} is 32.3 mm (U.S. #10). All the other variables were the same as those above for the machining method. The cost of heading each bar, $P_{heading-CAM}$ and $P_{heading-NiTi}$ was estimated as \$10/bar, which included both ends of the bar.

Using the same approach, the cost of NiTi RC columns was obtained for machining and heading methods. For machining, the number of NiTi SEA bars N_{NiTi} is 33 while that for heading is 25. The length of NiTi SEA in plastic region L_{NiTi} is 514 mm, which requires $n_{NiTi} = 2$ as received NiTi SEA bars (each as received NiTi SEA bar is 300 mm in length). The diameter of NiTi SEA before machining is 30 mm, after machining it is 26 mm. The diameter of remaining steel rebar d_{steel} is 28.7 mm (U.S. #9) for machining and it is 32.3 mm (U.S. #10) for heading. The density of NiTi SEA ρ_{NiTi} is 6.5 g/cm³. The price of NiTi SEA P_{NiTi} is \$154.3 /kg. When machining NiTi SEA, the four parts of machining cost were respectively taken as $C_{setup} = \$120$ /h, $C_{turning} = \$120$ /h, $C_{insert} = \$100$ /each, $C_{cutting} = \$300$. For each piece of NiTi SEA machining, one setup work and two pieces of inserts are needed. The time required for each piece of NiTi SEA machining was taken as 3.25 h. 100 specimens were considered to compute the average price of machining NiTi SEA. The number of NiTi SEA bars N_{NiTi} is 25.

The results of this cost estimation is provided in Table 3-5.

Table 3-5 Results of cost estimation.

Conventional RC		CAM with Machining		CAM with Heading		NiTi with Machining		NiTi with Heading	
N_{steel}	12	N_{CAM}	42	N_{CAM}	32	N_{NiTi}	33	N_{NiTi}	25
d_{steel} (mm)	36	L_{CAM} (mm)	674	L_{CAM} (mm)	674	L_{NiTi} (mm)	514	L_{NiTi} (mm)	514
$r_{hosteel}$ (g/cm ³)	7.8	n_{CAM}	3	n_{CAM}	3	n_{NiTi}	2	n_{NiTi}	2
P_{steel} (\$/kg)	2.2	d_{steel} (mm)	28.7	d_{steel} (mm)	32.3	d_{steel} (mm)	28.7	d_{steel} (mm)	32.3
E_{steel} (\$)	101	ρ_{CAM} (g/cm ³)	7.1	ρ_{CAM} (g/cm ³)	7.1	ρ_{NiTi} (g/cm ³)	6.5	ρ_{NiTi} (g/cm ³)	6.5
T_{steel} (\$)	1212	P_{CAM} (\$/kg)	66.14	P_{CAM} (\$/kg)	66.14	P_{NiTi} (\$/kg)	154.3	P_{NiTi} (\$/kg)	154.3
		$E_{material}$ (\$)	224	$E_{material}$ (\$)	224	$E_{material}$ (\$)	364	$E_{material}$ (\$)	364
		$P_{machine-CAM}$ (\$/each)	46	$P_{heading-CAM}$ (\$/each)	10	$P_{machine-NiTi}$ (\$/each)	46	$P_{heading-NiTi}$ (\$/each)	10
		$E_{machining}$ (\$)	138	$E_{heading}$ (\$)	30	$E_{machining}$ (\$)	896	$E_{heading}$ (\$)	20
		$P_{coupler}$ (\$/each)	10	$P_{coupler}$ (\$/each)	10	$P_{coupler}$ (\$/each)	10	$P_{coupler}$ (\$/each)	10
		$E_{coupler}$ (\$)	40	$E_{coupler}$ (\$)	40	$E_{coupler}$ (\$)	30	$E_{coupler}$ (\$)	30
		$E_{remainsteel}$ (\$)	57	$E_{remainsteel}$ (\$)	72	$E_{remainsteel}$ (\$)	59	$E_{remainsteel}$ (\$)	74
		$E_{CAM-machine}$ (\$)	459	$E_{CAM-heading}$ (\$)	336	$E_{NiTi-machine}$ (\$)	2245	$E_{NiTi-heading}$ (\$)	493
		$T_{CAM-machine}$ (\$)	19278	$T_{CAM-heading}$ (\$)	11712	$T_{NiTi-machine}$ (\$)	74085	$T_{NiTi-heading}$ (\$)	12325

3.5.5. Discussion

Based on the above calculations, the cost comparison of steel RC, CAM SEA RC, and NiTi SEA RC is shown in Figure 3-59. The total cost of longitudinal reinforcement of a steel RC is \$1212. While for CAM SEA RC, the total cost is \$19,278 when using machining and \$11,712 when using heading. The cost increased by \$18,066 (when using machining) and \$10,500 (when using heading) in comparison with the conventional steel RC column. For each NiTi RC column, the total cost is \$74,085

when using machining and \$12,325 when using heading. The cost increased by \$72,873 (when using machining) and \$11,113 (when using heading) in comparison with conventional steel RC column.

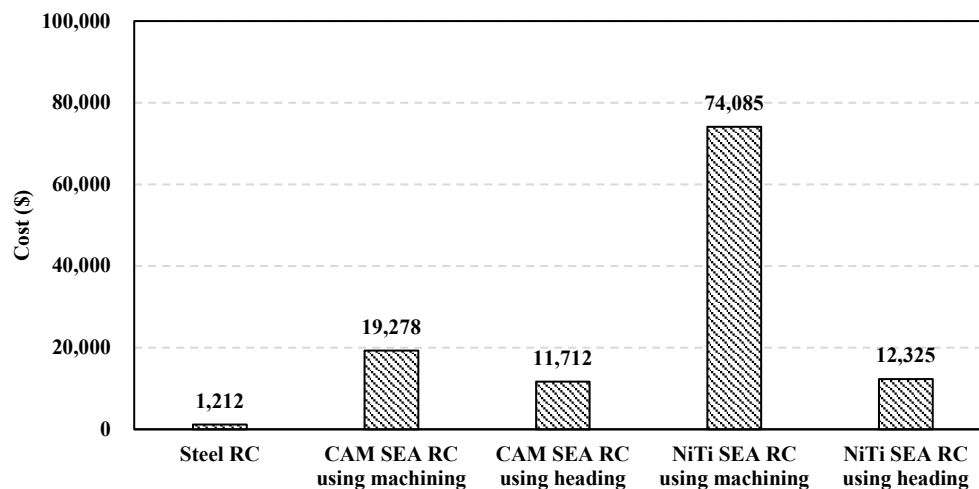


Figure 3-59 Cost comparison of steel RC, CAM SEA RC, and NiTi SEA RC.

It should be noted that, in this study, it is assumed that the difference in the cost of the three columns is only due to the longitudinal reinforcement. This assumption is approximate because the use of SEA reinforcement may alter other aspects of construction. The added cost to the total cost of the column with CAM SEA heading is \$11,712, which is expected to be a trivial increase in the overall cost of the column. The reason is that for conventional RC column, its permanent deformation after earthquake is still a problem. The cost used to repair or rehabilitate the column after an earthquake should also be considered. The excellent strain recovery and energy dissipation capacity of SEA bars are shown to reduce the permanent deformation of SEA reinforced columns up to 91% compared with the conventional RC column after being subjected to a peak drift of 7%, as reported by Hosseini et al. [1]. Therefore, in comparison with conventional steel RC, columns reinforced with SEA are expected to decrease the total cost in the long term.

To estimate the economic impact of using SEA on the overall cost of a bridge, the study by Saiidi et al. [26] provides useful information. A typical 5-span, box girder bridge rigidly supported on four, two-column bents was studied. A conventional RC bridge formed the benchmark. The columns of the bridge were redesigned assuming NiTi combined with engineered cementitious composites (ECC) in the top and bottom of plastic hinges using the method presented in [26]. The initial and repair cost of the two versions of the bridge were estimated for the design level earthquake scenario. The overall cost difference was 7.4% when NiTi/ECC is used. Under strong earthquakes, the damage in the conventional bridge would be more severe thus increasing the repair cost. In that case, the overall difference in the initial plus repair cost was estimated at 3.3%. This assumes that the conventional bridge would be repairable. Should the conventional bridge be deemed unsafe and replaced due to severe damage, the use of NiTi/ECC would substantially reduce the overall cost. Adding the user and traffic control cost of typically prolonged repair/construction of conventional bridges, would make the use of SEA even more economically attractive especially when CAM SEA are used. The use of SEA in bridges in earthquake prone areas results in long-term reduction of the cost of bridges.

3.5.6. Summary

The CAM SEA reinforced column shows economic advantage over the NiTi reinforced column particularly if the machining method is used to connect SEA bars with the steel rebar. The additional cost of CAM SEA reinforced column is only about 1/4 of the cost on NiTi SEA reinforced column, indicating the cost effectiveness of CAM SEA resulting from its excellent machinability. Even though the costs of CAM SEA reinforced column and NiTi SEA reinforced columns are very close when using heading, it should be noted that the reliable coupling between large diameter SEA bars with steel rebar to resist seismic loading is still a problem. The feasibility and performance of heading large diameter SEA bars still require further research. Therefore, considering the most commonly used coupling method at present, i.e., threaded coupling by machining, it can be said that using CAM SEA in bridges reduces the cost up to 75% compared to NiTi SEA.

With respect to the overall cost impact of using SEA, past research has shown that the overall initial plus repair cost increases by a negligible amount under the design level earthquakes. However, under strong earthquakes causing severe damage to conventional bridges, SEA would keep the bridge operational requiring minor repairs, whereas a conventional bridge would either be decommissioned for a long period to be repaired with substantial cost, or totally replaced if deemed unsafe. Either way, the SEA alternative would result in major saving. For future research, a reliability-based life-cycle cost estimation approach is recommended to better understand the impact of using SEAs as plastic hinge reinforcement by incorporating the costs of repair, and downtime in a probabilistic framework.

4. PLANS FOR IMPLEMENTATION

There is a need for further research to understand and develop a reliable coupler that is also cost effective for CAM SEAs. The influence of the heat treatment from the heading method should be studied under controlled conditions to understand the source of brittle failures observed in the headed coupling tests. The potential of using heat treatment following the heading should be investigated for different heat treatment conditions. The influence of the heading process and the post heat treatment on the grain size, distribution and orientation of the CAM SEAs would be helpful in understanding the failures and developing effective coupling methods. Based on the findings of this research, implementation of CAM SEAs in real bridges is feasible using the machined coupling method as it has been shown to work in laboratory studies [1,7,27,28].

5. CONCLUSIONS

This research has shown that CAM SEAs are a strong and viable alternative to NiTi SEAs to be used as a plastic hinge reinforcement. CAM SEAs exhibited higher fatigue lives than NiTi SEAs exceeding 50,000 cycles. The corrosion resistance of CAM SEAs was found to be significantly higher than mild steel and similar to or even better than high-chromium steel under long-term testing. Machineability of CAM SEAs was better than NiTi SEAs and similar to that of mild steel. These are the main advantages of CAM SEAs over NiTi SEAs in addition to temperature and strain rate independency of the properties that have been demonstrated in previous research. Additionally, if machining is used (rather than headed coupling) it was found that the added cost of CAM SEAs is approximately 1/4 of that if NiTi SEAs are used. However, CAM SEAs still do have some shortcomings. Particularly, there is currently a limitation on the maximum diameter and length of CAM SEAs that can be produced as a single crystal material. This limitation, when combined with the lower yield strength of CAM SEAs may result in a very large number of bars in a column when higher flexural resistance is required. Additionally, since the mechanical properties of SEAs are dependent on the temperature and

temperature history, simple splicing methods that are cost effective for mild steel and has been shown to work for NiTi such as headed couplers seem to be unreliable due to heat induced embrittlement. It is noted here that only the tensile behavior of CAM and NiTi SEAs is investigated here. When implemented in columns, these materials are subjected to cyclic tension-compression stresses under load reversals. Previous laboratory tests on columns with CAM or NiTi SEAs have shown that this load reversal does not pose a disadvantage or alter the column behavior [1,7]. The main conclusion of this research project is that CAM SEAs show excellent properties comparable to or superior than existing alternatives. The only major impediment for real life implementation of this SEA composition is the mechanical splicing, which is recommended for future research.

6. INVESTIGATOR'S PROFILE

Dr. Bora Gencturk is an Associate Professor and the Director of Structures and Materials Research Laboratory (SMRL) in the Sonny Astani Civil and Environmental Engineering Department at the University of Southern California (USC). He obtained his Ph.D. and M.S. degrees from the University of Illinois at Urbana-Champaign and his B.S. degree from Bogazici University (Istanbul, Turkey). Dr. Gencturk's research focuses on the durability and extreme event resilience of reinforced concrete structures with emphasis on application of high-performance materials. He specifically studies the degradation of cementitious materials due to environmental aging (e.g., alkali-silica reactivity and corrosion of reinforcing steel) and investigates the application of higher performance materials (e.g., engineered cementitious composites, and high- and ultra-high-performance concretes) to mitigate these issues. He combines his cementitious material degradation studies with structural-scale tests to investigate the impacts of (both traditional and advanced) material performance on the response of structures under extreme events (e.g., earthquakes and impact). To date, Dr. Gencturk has been awarded \$13M total in research funding as a PI or Co-PI (\$5.3M as his individual share). He has received both young investigator awards given by the U.S. National Science Foundation (NSF): Faculty Early Career Development (CAREER) and Broadening Participation Research Initiation Grant in Engineering (BRIGE). Dr. Gencturk has authored or co-authored 64 refereed journal papers, three book chapters, six research reports, and 49 conference papers. He has graduated seven Ph.D. and five M.S. students (with theses). He is currently advising one post-doc and two Ph.D. students. Dr. Gencturk teaches courses on mechanical behavior of materials, structural dynamics and earthquake engineering, reinforced concrete design and behavior, probabilistic methods and structural reliability. He served as the Co-Guest Editor of two special issues, one in American Society of Civil Engineers (ASCE) Journal of Structural Engineering, and the other one in Journal of Earthquake Engineering. He reviewed proposals for NSF, the United States Department of Energy (DOE), the Natural Sciences and Engineering Research Council (NSERC) of Canada, the Chilean National Science and Technology Commission (CONICYT), and the Czech Science Foundation (GACR). He is a member of ASCE, the American Concrete Institute, and the Earthquake Engineering Research Institute. Dr. Gencturk is also a registered Professional Civil Engineer in California.

Dr. Saiidi is senior principal at Infrastructure Innovation, LLC, a Distinguished Researcher at the University of California, Los Angeles, and a Professor Emeritus and Director of Center for Advanced Technology in Bridges and Infrastructure at the University of Nevada, Reno. He has published over 550 papers/reports and given over 450 presentations, many as a keynote speaker. Dr. Saiidi research has been funded by many national and state agencies focusing on experimental and analytical studies of seismic response of reinforced concrete structures, seismic retrofit, resiliency with novel materials, and

seismic response and design of precast bridges. He has served as a technical expert on several bridge and building related disputes. Dr. Saiidi has received many awards for his research and publications.

7. REFERENCES

- [1] F. Hosseini, B. Gencturk, S. Lahpour, D.I. Gil, An experimental investigation of innovative bridge columns with engineered cementitious composites and Cu-Al-Mn super-elastic alloys, *Smart Mater. Struct.* (2015). <https://doi.org/10.1088/0964-1726/24/8/085029>.
- [2] B. Gencturk, Y. Araki, T. Kusama, T. Omori, R. Kainuma, F. Medina, Loading rate and temperature dependency of superelastic Cu-Al-Mn alloys, *Constr. Build. Mater.* (2014). <https://doi.org/10.1016/j.conbuildmat.2013.12.002>.
- [3] K.C. Shrestha, Y. Araki, T. Kusama, T. Omori, R. Kainuma, Functional Fatigue of Polycrystalline Cu-Al-Mn Superelastic Alloy Bars under Cyclic Tension, *J. Mater. Civ. Eng.* 28 (2016). [https://doi.org/10.1061/\(asce\)mt.1943-5533.0001417](https://doi.org/10.1061/(asce)mt.1943-5533.0001417).
- [4] Y. Araki, T. Endo, T. Omori, Y. Sutou, Y. Koetaka, R. Kainuma, K. Ishida, Potential of superelastic Cu-Al-Mn alloy bars for seismic applications, *Earthq. Eng. Struct. Dyn.* (2011). <https://doi.org/10.1002/eqe.1029>.
- [5] S. Kise, Y. Araki, T. Omori, R. Kainuma, Orientation Dependence of Plasticity and Fracture in Single-Crystal Superelastic Cu-Al-Mn SMA Bars, *J. Mater. Civ. Eng.* 33 (2021). [https://doi.org/10.1061/\(asce\)mt.1943-5533.0003568](https://doi.org/10.1061/(asce)mt.1943-5533.0003568).
- [6] S. Kise, A. Mohebbi, M.S. Saiidi, T. Omori, R. Kainuma, K.C. Shrestha, Y. Araki, Mechanical splicing of superelastic Cu-Al-Mn alloy bars with headed ends, *Smart Mater. Struct.* 27 (2018). <https://doi.org/10.1088/1361-665X/aabf0d>.
- [7] S. Varela, M. Saiidi, Resilient deconstructible columns for accelerated bridge construction in seismically active areas, *J. Intell. Mater. Syst. Struct.* 28 (2017). <https://doi.org/10.1177/1045389X16679285>.
- [8] T.O. Standards, Standard Practice for Verification and Classification of Extensometer System, *Annu. B. ASTM Stand.* (2016).
- [9] Y. Araki, K. Kimura, T. Asai, T. Masui, T. Omori, R. Kainuma, Integrated mechanical and material design of quasi-zero-stiffness vibration isolator with superelastic Cu-Al-Mn shape memory alloy bars, *J. Sound Vib.* (2015). <https://doi.org/10.1016/j.jsv.2015.08.018>.
- [10] Y. Araki, K.C. Shrestha, N. Maekawa, Y. Koetaka, T. Omori, R. Kainuma, Shaking table tests of steel frame with superelastic Cu-Al-Mn SMA tension braces, *Earthq. Eng. Struct. Dyn.* (2016). <https://doi.org/10.1002/eqe.2659>.
- [11] C. Maletta, E. Sgambitterra, F. Furgiuele, R. Casati, A. Tuissi, Fatigue properties of a pseudoelastic NiTi alloy: Strain ratcheting and hysteresis under cyclic tensile loading, *Int. J. Fatigue.* 66 (2014). <https://doi.org/10.1016/j.ijfatigue.2014.03.011>.
- [12] V. Iasnii, P. Yasniy, D. Baran, A. Rudawska, The effect of temperature on low-cycle fatigue of shape memory alloy, *Frat. Ed Integrita Strutt.* 13 (2019). <https://doi.org/10.3221/IGF-ESIS.50.26>.
- [13] M.J. Mahtabi, N. Shamsaei, M.R. Mitchell, Fatigue of Nitinol: The state-of-the-art and ongoing challenges, *J. Mech. Behav. Biomed. Mater.* 50 (2015). <https://doi.org/10.1016/j.jmbbm.2015.06.010>.
- [14] ASTM, A516/A516M Standard Specification for Pressure Vessel Plates, Carbon Steel, for Moderate- and Lower-Temperature Service, *Annu. B. ASTM Stand.* 10 (2011).
- [15] ASTM, A615/A615M: Standard Specification for Deformed and Plain Carbon-Steel Bars for

- Concrete Reinforcement, Astm. (2020).
- [16] ASTM, A955/A955M Standard Specification for Deformed and Plain Stainless Steel Bars for Concrete Reinforcement, (2020).
- [17] ASTM, A1035/A1035M Standard Specification for Deformed and Plain , Low-carbon , Chromium , Steel Bars for Concrete Reinforcement, Astm. (2015). <https://doi.org/10.1520/A1035>.
- [18] ASTM, ASTM G85-11: Standard Practice for Modified Salt Spray (Fog) Testing, ASTM Stand. i (2011).
- [19] ASTM A370-19, Standard Test Methods and Definitions for Mechanical Testing of Steel Products, ASTM Int. West Conshohocken, PA, USA. (2019).
- [20] V. Nachiappan, E.H. Cho, Corrosion of High Chromium and Conventional Steels Embedded in Concrete, *J. Perform. Constr. Facil.* 19 (2005). [https://doi.org/10.1061/\(asce\)0887-3828\(2005\)19:1\(56\)](https://doi.org/10.1061/(asce)0887-3828(2005)19:1(56)).
- [21] S. Pareek, S. Kise, F. Yamashita, B. Gencturk, F. Hosseini, S. Alexis Brown, Y. Araki, Chemical Resistance of Cu-Al-Mn Superelastic Alloy Bars in Acidic and Alkaline Environments, *J. Mater. Civ. Eng.* 33 (2021). [https://doi.org/10.1061/\(asce\)mt.1943-5533.0003478](https://doi.org/10.1061/(asce)mt.1943-5533.0003478).
- [22] K. Weinert, V. Petzoldt, Machining of NiTi based shape memory alloys, *Mater. Sci. Eng. A.* 378 (2004). <https://doi.org/10.1016/j.msea.2003.10.344>.
- [23] H.C. Lin, K.M. Lin, Y.C. Chen, Study on the machining characteristics of TiNi shape memory alloys, *J. Mater. Process. Technol.* 105 (2000). [https://doi.org/10.1016/S0924-0136\(00\)00656-7](https://doi.org/10.1016/S0924-0136(00)00656-7).
- [24] K.E. Kirmacioglu, Y. Kaynak, O. Benafan, Machinability of Ni-rich NiTiHf high temperature shape memory alloy, *Smart Mater. Struct.* (2019). <https://doi.org/10.1088/1361-665X/ab02a2>.
- [25] Y. Guo, A. Klink, C. Fu, J. Snyder, Machinability and surface integrity of Nitinol shape memory alloy, *CIRP Ann. - Manuf. Technol.* 62 (2013). <https://doi.org/10.1016/j.cirp.2013.03.004>.
- [26] M.S. Saiidi, M. Tazarv, S. Varela, S. Bennion, M.L. Marsh, I. Ghorbani, T.P. Murphy, Seismic Evaluation of Bridge Columns with Energy Dissipating Mechanisms, Volume 1: Research Overview and Volume 2: Guidelines . National Cooperative Highway Research Program (NCHRP) Research Report 864., (2018).
- [27] K.C. Shrestha, Y. Araki, T. Nagae, Y. Koetaka, Y. Suzuki, T. Omori, Y. Sutou, R. Kainuma, K. Ishida, Feasibility of Cu-Al-Mn superelastic alloy bars as reinforcement elements in concrete beams, *Smart Mater. Struct.* 22 (2013). <https://doi.org/10.1088/0964-1726/22/2/025025>.
- [28] S. Pareek, Y. Suzuki, Y. Araki, M.A. Youssef, M. Meshaly, Plastic hinge relocation in reinforced concrete beams using Cu-Al-Mn SMA bars, *Eng. Struct.* (2018). <https://doi.org/10.1016/j.engstruct.2018.08.072>.

8. APPENDIX RESEARCH RESULTS

8.1. WHAT WAS THE NEED?

Prior research indicates drastic improvements to a column's seismic performance when the plastic hinge reinforcement is replaced with superelastic alloys (SEAs), which is a type of shape memory alloy (SMA) that exhibits reversible yielding and energy dissipation with little to no damage accumulation. The improvement is specifically in terms of repair needed after an earthquake in the bridge columns. No damage implies no or little permanent deformations after an earthquake. This allows for continued use of bridges with or little repair after an earthquake, reducing downtime, cost and facilitating post-earthquake recovery efforts. Previously, NiTi SEAs, a different alloy composition, have been successfully tested and used for the first time in the SR99 Alaskan Viaduct Bridge in Seattle, which was completed in 2017. However, certain properties of NiTi SEAs make it still a worthwhile effort to investigate other SEA compositions. Specifically, it is known that NiTi SEAs have a lower operating temperature range, more dependency on strain rate, low machineability, lower structural fatigue life, and a high price tag.

8.2. WHAT WAS OUR GOAL?

Our goal in this research was to determine if Cu-Al-Mn (CAM) SEAs, a different alloy composition, is a viable alternative for application as plastic hinge reinforcement in bridge columns.

8.3. WHAT DID WE DO?

To achieve the above stated goal, experimental characterization of CAM SEAs has been performed to determine the following characteristics: low-cycle high-strain fatigue lives, corrosion resistance, machineability, and mechanical splicing performance. Additionally, an analysis was performed to compare the cost of a conventional column with that using NiTi SEA or CAM SEAs.

8.4. WHAT WAS THE OUTCOME?

This research has shown that CAM SEAs are a strong and viable alternative to NiTi SEAs to be used as a plastic hinge reinforcement. CAM SEAs exhibited higher fatigue lives than NiTi SEAs exceeding 50,000 cycles. The corrosion resistance of CAM SEAs was found to be significantly higher than mild steel and similar to or even better than high-chromium steel under long-term testing. Machineability of CAM SEAs was better than NiTi SEAs and similar to that of mild steel. The added cost of CAM SEAs to the cost of a bridge column if machining is used was found to be approximately 1/4 of that of NiTi SEAs. These are the main advantages of CAM SEAs over NiTi SEAs in addition to temperature and strain rate independency of the properties that has been demonstrated in previous research. The research has shown that it is still required to develop a reliable coupling method for CAM SEAs as the currently available methods have shown either premature failures or were not efficient in terms of the material usage and cost. CAM SEAs currently have a limitation on the length of the bar that can be produced, therefore, coupling is essential to achieve longer plastic hinge reinforcement and also to connect to steel rebar.

8.5. WHAT IS THE BENEFIT?

CAM SEAs have been shown to be a viable alternative to NiTi SEAs to drastically improve bridge seismic performance. A widespread implementation of SEAs as plastic hinge reinforcement of bridge

columns is going to improve the resiliency of our communities. Having an alternate material with similar or better properties at a lower cost is a direct benefit.